

UNCLASSIFIED

AD NUMBER

ADB011771

LIMITATION CHANGES

TO:

Approved for public release; distribution is unlimited.

FROM:

Distribution authorized to U.S. Gov't. agencies only; Test and Evaluation; MAY 1976. Other requests shall be referred to Air Force Weapons Lab., Kirtland AFB, NM.

AUTHORITY

AFWL ltr 29 Apr 1985

THIS PAGE IS UNCLASSIFIED

AD

B011771

AUTHORITY:

AFWL 17, 29 APR 85



2

ADBO11771

THE MECHANICS OF CENTRAL PEAK FORMATION IN SHOCK WAVE CRATERING EVENTS

May 1976

Final Report

Distribution limited to US Government agencies only because of ~~operational testing of equipment/systems~~ (May 1976). Other requests for this document must be referred to AFWL (DEV), Kirtland AFB, NM 87117. *T&E*

This research was sponsored by the Defense Nuclear Agency under Subtask SB144, Work Unit 11, Determination of the Properties of Earth Media and Their Influence on Ground Motions.

Prepared for
Director
DEFENSE NUCLEAR AGENCY
Washington, DC 20305

AIR FORCE WEAPONS LABORATORY
Air Force Systems Command
Kirtland Air Force Base, NM 87117

DDC
REGISTERED
JUN 23 1976
C



AD No. _____
DDC FILE COPY

This final report was prepared by the Air Force Weapons Laboratory, Kirtland Air Force Base, New Mexico, under Job Order WDNS3309. Captain Gilbert W. Ullrich (DEV) was the Laboratory Project Officer-in-Charge.

When US Government drawings, specifications, or other data are used for any purpose other than a definitely related Government procurement operation, the Government thereby incurs no responsibility nor any obligation whatsoever, and the fact that the Government may have formulated, furnished, or in any way supplied the said drawings, specifications, or other data, is not to be regarded by implication or otherwise, as in any manner licensing the holder or any other person or corporation, or conveying any rights or permission to manufacture, use, or sell any patented invention that may in any way be related thereto.

This technical report has been reviewed and is approved for publication.

Gilbert W. Ullrich

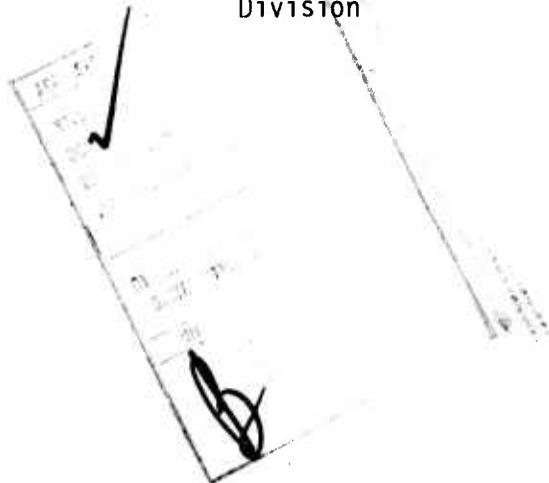
GILBERT W. ULLRICH
Captain, USAF
Project Officer

James M. Warren

JAMES M. WARREN
Lt Colonel, USAF
Chief, Facility Survivability Branch

Frank J. Leech

FRANK J. LEECH
Lt Colonel, USAF
Chief, Civil Engineering Research
Division



UNCLASSIFIED

SECURITY CLASSIFICATION OF THIS PAGE (When Date Entered)

REPORT DOCUMENTATION PAGE		READ INSTRUCTIONS BEFORE COMPLETING FORM
1. REPORT NUMBER 14 AFWL-TR-75-88	2. GOVT ACCESSION NO.	3. RECIPIENT'S CATALOG NUMBER 9
4. TITLE (and Subtitle) 6 THE MECHANICS OF CENTRAL PEAK FORMATION IN SHOCK WAVE CRATERING EVENTS.		4. TYPE OF REPORT & PERIOD COVERED Final Report
7. AUTHOR(s) 10 Gilbert W. Ullrich, Capt, USAF		5. PERFORMING ORG. REPORT NUMBER
9. PERFORMING ORGANIZATION NAME AND ADDRESS Air Force Weapons Laboratory (DEV) Kirtland Air Force Base, NM 87117		6. CONTRACT OR GRANT NUMBER(s)
11. CONTROLLING OFFICE NAME AND ADDRESS Director Defense Nuclear Agency Washington, D.C. 20305		10. PROGRAM ELEMENT, PROJECT, TASK AREA & WORK UNIT NUMBERS 62704H WDNS3309
14. MONITORING AGENCY NAME & ADDRESS (if different from Controlling Office)		11. REPORT DATE 11 May 1976
Air Force Weapons Laboratory (DEV) Kirtland Air Force Base, NM 87117		12. NUMBER OF PAGES 140
16. DISTRIBUTION STATEMENT (of this Report) Distribution limited to US Government agencies only because of operational testing of equipment/systems (May 1976). Other requests for this document must be referred to AFWL (DEV), Kirtland AFB, NM 87117.		13. SECURITY CLASS. (of this report) UNCLASSIFIED
17. DISTRIBUTION STATEMENT (of the abstract entered in Block 20, if different from Report) 16 DNA-NWER-SB-144		14. DECLASSIFICATION/DOWNGRADING SCHEDULE
18. SUPPLEMENTARY NOTES		
19. KEY WORDS (Continue on reverse side if necessary and identify by block number) High-explosive tests Boundary conditions MIXED COMPANY Test Series Numerical techniques Ground motion tests Cratering tests		
20. ABSTRACT (Continue on reverse side if necessary and identify by block number) A series of numerical simulations of ground response to a high-explosive detonation was used to examine the influence of material models on calculated central-peak formation in shock-produced craters. One simulation of the 20-ton high-explosive detonation Mixed Company II showed that computed motions at 16.4 msec, when ballistically extrapolated, were consistent with the observed crater and formation of a central mound. Compaction, layering, and material yield models were varied in additional simulations. →(over)		

DD FORM 1473 EDITION OF 1 NOV 65 IS OBSOLETE

UNCLASSIFIED

SECURITY CLASSIFICATION OF THIS PAGE (When Date Entered)

013 150 ✓

mt

UNCLASSIFIED

SECURITY CLASSIFICATION OF THIS PAGE(When Data Entered)

ABSTRACT (cont'd) for P1473A)

→ The results indicated the occurrence of a central mound is primarily dependent on material properties of the medium.

4

UNCLASSIFIED

SECURITY CLASSIFICATION OF THIS PAGE(When Data Entered)

SUMMARY

Central peaks are common features observed in craters on the earth, the moon, Mars, and Mercury. Since these peaks do not occur in all craters, they should be useful in providing strong constraints on both planetary evolution and numerical cratering simulations. Unfortunately, because the mechanics of central peak formation has been poorly understood, little use of those constraints has yet been made.

Therefore, a program of numerical simulations of the ground response to a high-explosive detonation was accomplished to examine the influence of model conditions on calculated central peak formation. During this program, data from a numerical simulation of a high-explosive detonation were used as a surface-boundary condition, and the ground response was simulated by a computer code that modeled two-dimensional, axisymmetric problems of continuum-mechanics with elastic-plastic material models. First, a calculation that modeled the 20-ton high-explosive detonation designated MIXED COMPANY II showed that, when ballistically extrapolated, the computed motions at a simulated time of 16.4 msec were consistent with the observed crater and formation of a central mound. The results of a series of calculations in which compaction, layering, and material-yield models were varied indicated (1) the calculated upward motions below the crater were eliminated by increased material compactibility, (2) the model of test-site layering in the MIXED COMPANY II numerical simulation only slightly influenced the upward velocities below the crater, (3) plastic volumetric increases of material during Mohr-Coulomb yield contributed significantly to the calculation of upward motions, (4) upward velocities for points on the axis of symmetry were first calculated where strength effects were important, and (5) the inclusion of a lower, "fluid" layer modified the calculated response in an overlying, solid layer in a manner that may have eventually resulted in upward motions.

A mechanical model of central mound formation was developed with the results of the numerical calculations as a guide. Material rebound in the region where strength effects are important was emphasized in the model. Central mounds would be inhibited by material compaction unless a lower layer responded as a fluid. The mechanical model includes enhancement of the central mound primarily

by material bulking but also by reflections of stress waves and the effect of the main shear wave. Gravitational adjustments that contribute to inward displacements are considered possible. This model is found to be consistent with both the observed occurrence and structural relations of central peaks at sites of nuclear and high-explosive detonations and hypervelocity impact events. The conclusions are that the mechanical model is generally applicable to central peak formation, the occurrence of a central peak in a crater is primarily dependent on material properties of the medium, and the calculational code used for the numerical simulations can serve as a tool to investigate those material properties.

PREFACE

This document was originally a doctoral thesis submitted to the Massachusetts Institute of Technology. M. G. Simmons of MIT provided much time and encouragement, and his suggestions were extremely valuable. R. J. Port of the Air Force Weapons Laboratory first suggested the MIXED COMPANY II numerical simulation, then he provided valuable physical insight that led to the successful model. The guidance and support of D. R. Roddy, J. R. McGetchin, C. Goetze, and J. B. Southard was appreciated, and their time and ideas were especially important.

Permission to use the AFTON-2A code was graciously granted by J. G. Trulio, and R. Waters of the Defense Nuclear Agency and B. L. Carnes of the US Army Waterways Experiment Station provided the MIXED COMPANY II crater profiles.

Significant support from the Air Force Weapons Laboratory Civil Engineering Branch and the Air Force Cambridge Research Laboratory Computation Support Division included providing the computer codes and training in their use, and aid in the solution of the many programming problems encountered.

CONTENTS

<u>Section</u>		<u>Page</u>
I	INTRODUCTION	11
II	PREVIOUS WORK OF OTHERS	15
	Occurrence and Structure of Central Peaks	15
	Previous Computational Programs	23
	Postulated Mechanisms	27
III	NUMERICAL SIMULATION OF SHOCK WAVE CRATERING	33
	MIXED COMPANY II Experiment	33
	Computational Model of MIXED COMPANY II	36
	MIXED COMPANY II Numerical Simulation (MC 2.12)	46
	Numerical Parametric Study	63
IV	DISCUSSION AND CONCLUSION	90
	Discussion	90
	Conclusions	95
	Future Work	96
	APPENDIX A COMPUTATION PARAMETERS	99
	APPENDIX B THE AFTON-2A CODE	103
	APPENDIX C AUXILIARY COMPUTATION ROUTINES	124
	BIBLIOGRAPHY	129

ILLUSTRATIONS

<u>Figure</u>		<u>Page</u>
1	Generalized Stratigraphic Sections from the Western Side of the Flynn Creek Structure	16
2	The Size Distribution of Craters with Central Peaks on the Earth, Mars, and the Moon	19
3	Cross Section of the Crater Produced by the 500-ton TNT Event SNOWBALL	21
4	Velocity Vectors at a Simulated Time of 220 msec for the DISTANT PLAIN 6 Calculation	24
5	Vertical Velocity Comparison between MIDDLE GUST III Experimental Measurement and Three Material Models	28
6	Composite Crater Profile Constructed from the Detonation of Two 40-Grain Dynamite Charges with the Shot Point at the Base of the Black Layer	29
7	Theoretical Lines of Slip under a Valley with Sides Dipping at 30° to the Horizontal	31
8	Apparent and True Crater Profiles of the 20-Ton TNT Event MIXED COMPANY II	35
9	The Model Pressure--Specific Volume Relation in the Low-Pressure Regime for Layer 2	40
10	The Model Pressure--Specific Volume Relation in the High-Pressure Regime for Layer 2	43
11	Schematic Yield Surface for Materials	44
12	Velocity Vector Plot for MC 2.12 at 8.4 msec after Detonation	47
13	Principal Stress Axes Plot for MC 2.12 at 8.4 msec after Detonation	48
14	Calculation Grid Plot for MC 2.12 at 616.4 msec after Detonation Compared to Observed Apparent and True Crater Profiles along the Southern Radial of the MIXED COMPANY II Crater	49
15	Velocity Vector Plot for MC 2.12 at 3.0 msec after Detonation	52
16	Acceleration Vector Plot for MC 2.12 at 3.0 msec after Detonation	53
17	Motion Time History for the Target Point Originally Located on the Vertical Axis at 10 Ft Depth in the MC 2.12 Calculation	54

ILLUSTRATIONS (Continued)

<u>Figure</u>	<u>Page</u>
18 Stress Time History for the Target Point of Figure 17 with Compressive Stresses Positive	55
19 Motion Time History of the Target Point Originally Located at 4 Ft Range and 8 Ft Depth in the MC 2.12 Calculation	57
20 Stress Time History for the Target Point of Figure 19 with Compressive Stresses Positive	58
21 Motion Time History of the Target Point Originally Located at 18 Feet Range and 4 Ft Depth in the MC 2.12 Calculation	59
22 Stress Time History for the Target Point of Figure 21 with Compressive Stresses Positive	60
23 Maximum Pressure Contours as a Function of Original Position for the MC 2.12 Calculation	61
24 Motion Time History of the Target Point Originally Located at 6 Feet Range and 1 Foot Depth in the MC 2.12 Calculation	62
25 Velocity Vector Plot for MC 2.13 at 9.5 msec after Detonation	64
26 Velocity Vector Plot for MCP-03 at 8.2 msec after Detonation	66
27 Velocity Vector Plot for MCP-09 at 9.5 msec after Detonation	67
28 Velocity Vector Plot for MCP-09 at 2.8 msec after Detonation	69
29 Velocity Vector Plot for MCP-01 at 8.4 msec after Detonation	70
30 Velocity Vector Plot for MCP-02 at 9.5 msec after Detonation	71
31 Velocity Vector Plot for MC 2.15 at 8.4 msec after Detonation	74
32 Velocity Vector Plot for MCP-06 at 3.2 msec after Detonation	75
33 Velocity Vector Plot for MCP-02 at 3.2 msec after Detonation	76
34 Velocity Vector Plot for MCP-05 at 19.9 msec after Detonation	78
35 Velocity Vector Plot for MCP-21 at 5.6 msec after Detonation	80
36 Velocity Vector Plot for MCP-21 at 6.9 msec after Detonation	81
37 Velocity Vector Plot for MCP-21 at 10.5 msec after Detonation	82

ILLUSTRATIONS (Continued)

<u>Figure</u>	<u>Page</u>
38 Motion Time History for the Target Point Originally Located on the Vertical Axis at 12 Feet Depth in the MCP-21 Calculation	83
39 Stress Time History for the Target Point of Figure 38 with Compressive Stresses Positive	84
40 Stress Time History for the Target Point Originally Located on the Vertical Axis at 20 Feet Depth in the MCP-21 Calculation	86
41 Velocity Vector Plot for MCP-12 at 6.6 msec after Detonation	89
B-1 Quadrilateral Wedge	104
B-2 Projection of the Cross Section of a Quadrilateral Zone in the x-y Plane	107
B-3 Quadrilateral Wedge and its Projections into the x-y, y-z, and x-z Planes	112
B-4 Interior Areas of a Quadrilateral Wedge	114
B-5 Momentum Zone Centered at Point 1 Projected Into the x-y Plane; Point 1 is the Vertex Common to the Four Thermodynamic Zones Labeled a, b, c, d	115
B-6 Illustration of the Sense of the Forces F_{1a} , F_{2a} , F_{3a} , and F_{4a}	117
B-7 Schematic of an Unstrained and Strained Triangular Zone	119

TABLES

<u>Table</u>		<u>Page</u>
1	Structures with Shatter Cones in Central Uplift	18
2	Defense Nuclear Agency High Explosive Experiments	21
3	MIXED COMPANY II Site Model	34
4	Summary of Numerical Simulation Results	92

SECTION I

INTRODUCTION

Central peaks, or mounds, are a common feature of craters. Such peaks have been observed in craters measured in feet (Roddy, 1968; 1973) and in craters measured in tens of miles (Baldwin, 1963). They occur in craters produced by chemical explosives (Roddy, 1973) and in ancient impact structures on the earth (Howard et al., 1972; Roddy, 1968; Dence, 1968; Beals, 1965). They have been seen in craters on the Moon (Baldwin, 1963), on Mars (Hartmann, 1973), and on Mercury (Murray et al., 1974). However, while several authors have advanced hypotheses as to the cause of central peaks (Baldwin, 1963; Short, 1965; Dence, 1968; Milton and Roddy, 1972), a satisfactory explanation of the mechanics of central mound formation has not been demonstrated.

Central mounds serve as a very useful constraint on cratering calculations because they are directly observable. The Defense Nuclear Agency (a branch of the U.S. Department of Defense) has sponsored many attempts to simulate numerically the cratering and ground-shock effects of experiments where high-explosive charges were detonated at the surface of the earth (Christensen, 1969; Maxwell and Moises, 1971b; Port and Gajewski, 1973; Wright et al., 1973; Ialongo, 1973). Primary constraints on these calculations have been comparisons with crater radii and depths, and comparisons with ground-motion data obtained from active instrumentation usually emplaced more than one crater radius from ground zero. Although central mounds occurred in many of the craters (Roddy, 1968; 1973), little attention has been given to whether the motions predicted by such calculations are consistent with central peak formation. Christensen (1970) considered such a constraint, and he found the requirements for upward motions below the detonation point to be a very useful guide to the physics required in the calculation because, while all computations predicted a crater, a central mound was predicted only under limited conditions. Therefore, the presence or absence of a central mound in an experimentally produced crater provides an immediate direct test of the adequacy of numerical simulations, and an understanding of the causes of the central mound will be important to the understanding of cratering and ground-shock mechanics.

Also, the central peaks observed in hypervelocity impact craters on planetary surfaces provide information on the conditions of the impact event. The high-velocity impact of a body on a planetary surface is a dynamic test of the two bodies over a very short time period. This information is recorded in the occurrence of a central mound; because, while the size of the crater is primarily controlled by the mass and velocity of the impacting particle (Baldwin, 1963), the formation of a central mound is primarily controlled either by properties of the planet (Baldwin, 1963; Short, 1965; Dence, 1968), by properties of the impacting body (Milton and Roddy, 1972), or by properties of both (Roddy, 1968b). An understanding of the causes of central mound formation may allow us to obtain information concerning the conditions at the time a crater was formed. The evolution of those conditions may then be studied by observations of craters of different ages, and variations of those conditions with location may be tested with central-peak data in different locations.

The central peaks of craters represent important sampling sites for any extraterrestrial landing or remote sensing mission. Roddy (1968) showed that the material in the central mound is the deepest material exposed during the cratering event. A traverse across the mound will sample the deepest stratigraphic section obtainable at the surface of a crater. An understanding of central peak formation will aid the determination of the pre-impact location of the material.

Therefore, a program of numerical simulations was accomplished to examine the causes of central peak formation in shock-wave cratering event. During this program, the models were limited to the simplest possible expressions to demonstrate which factors were most important in the formation of a central mound. These models were an idealization of much more complex material behavior. The AFTON-2A (see appendix B) computer code was used because it was already active in ground-shock calculations (see, for example, Port and Gajewski, 1973) and because no code development was required other than modifications of material behavior models. One model of a high-explosive detonation was used for all of the numerical simulations, and only models of material properties were varied. The results of the calculations were generalized to different types of cratering events by developing a general model for the causes of central mound formation that was compared to reported observations of central mounds.

To clarify this discussion, the terms "shock-wave cratering event" and "central mound" should be defined. A "shock-wave cratering event" is an event

that transfers a large amount of energy to a small volume of a halfspace by sending a shock wave into the halfspace and forms a crater at the surface. This term applies to both a hypervelocity impact and a surface chemical or nuclear explosive detonation. Further, as Shoemaker (1961) suggests, this term is more basic than explosion cratering event because, even if the characteristics of craters are controlled by the expansion of gases near the source of the event (Baldwin, 1963), the passage of the shock wave through the material is the mechanism which establishes the conditions for such expansion. A "central mound" is a local topographical high at the center of a crater that is composed of material that was displaced upward during the cratering event. This term is applicable to a definite structural feature, and is not meant to include the possibility that material ejected from the crater may subsequently fall into the crater and form a hill at the center. Also, in this report, the terms "central peak" and "central mound" will be synonymous.

Three assumptions were basic to the physical models used. First, all calculations were performed assuming axial symmetry, i.e., all properties can be described in terms of the radial and axial position coordinates of a cylindrical coordinate system. Second, all material models were assumed to be isotropic. Finally, no energy transfer by radiation or conduction was considered.

In addition to the basic assumptions, several additional assumptions were involved in this study. Some of these assumptions were inherent in the AFTON-2A code and are described in appendix B. Other assumptions were involved in the description of the numerical experiments accomplished and are described during the presentation of those problems.

The generalization of the results of numerical simulations should be done cautiously because those results strictly apply only to definite models with specific input parameters. The following procedure was used to generalize specific numerical results concerning the mechanics of central peak formation. First, the available information pertinent to central peaks was reviewed to provide the broadest possible base of data. Then, a numerical model of the high-explosive experiment MIXED COMPANY II is described to demonstrate the applicability of the numerical results to that one experiment. The results from additional numerical simulations in which material models were varied are described to determine what properties are important to central peak formation. These properties are included in a general model of central peak mechanics which

was tested by comparisons with the available information described initially.
Through this comparison the relevance of the general model was determined.

SECTION II

PREVIOUS WORK OF OTHERS

Three types of information are available concerning central mounds in shock-produced craters. First, observations, presented by others, of the occurrence of central peaks and of the structure of central uplifts in both ancient impact features on earth and experimental high-explosive detonations provide constraints on any explanation of central peak formation. Second, numerical simulations of shock-wave cratering events provide guides to the physical processes involved in central mound formation. Finally, several others have previously proposed hypotheses concerning the causes of central peak formation. In this section, information of each type is reviewed to provide a basis for later conclusions concerning the mechanics of central mound formation.

1. OCCURRENCE AND STRUCTURE OF CENTRAL PEAKS

Observations of the structure of central uplifts and their occurrence in craters indicate that similar relations apply to both hypervelocity impact events and explosive detonations. The material in the central uplifts of both ancient impact structures on earth and high-explosive craters is displaced upward from its original position (Roddy, 1968). Horizontal displacements of the material that forms central mounds are probably inward in the deeper regions and outward in the shallower regions (Howard, et al., 1972; Milton, et al., 1972). Shatter cones are frequently found in the central uplifts (Dietz, 1968; Roddy, 1973), indicating that maximum stresses were on the order of, but above, the Hugoniot elastic limit of the material. Central mounds do not occur in craters formed in very porous material.

a. Central Peaks in Hypervelocity Impact Structures

Central uplifts have been observed in many structures that have effects which are commonly associated with sites of hypervelocity impact events on earth (Dietz, 1968). Roddy (1968) examined one of those structures (2.3 miles in diameter) at Flynn Creek, Tennessee (figure 1). He found that Stones River and Knox strata occur in the center as folded, faulted, and brecciated material which forms a hill with a top about 370 feet above the original crater floor. This hill had the general structure of a domed megabreccia block with 100 feet of the Knox formation, now exposed as steeply dipping strata, raised 1100 feet

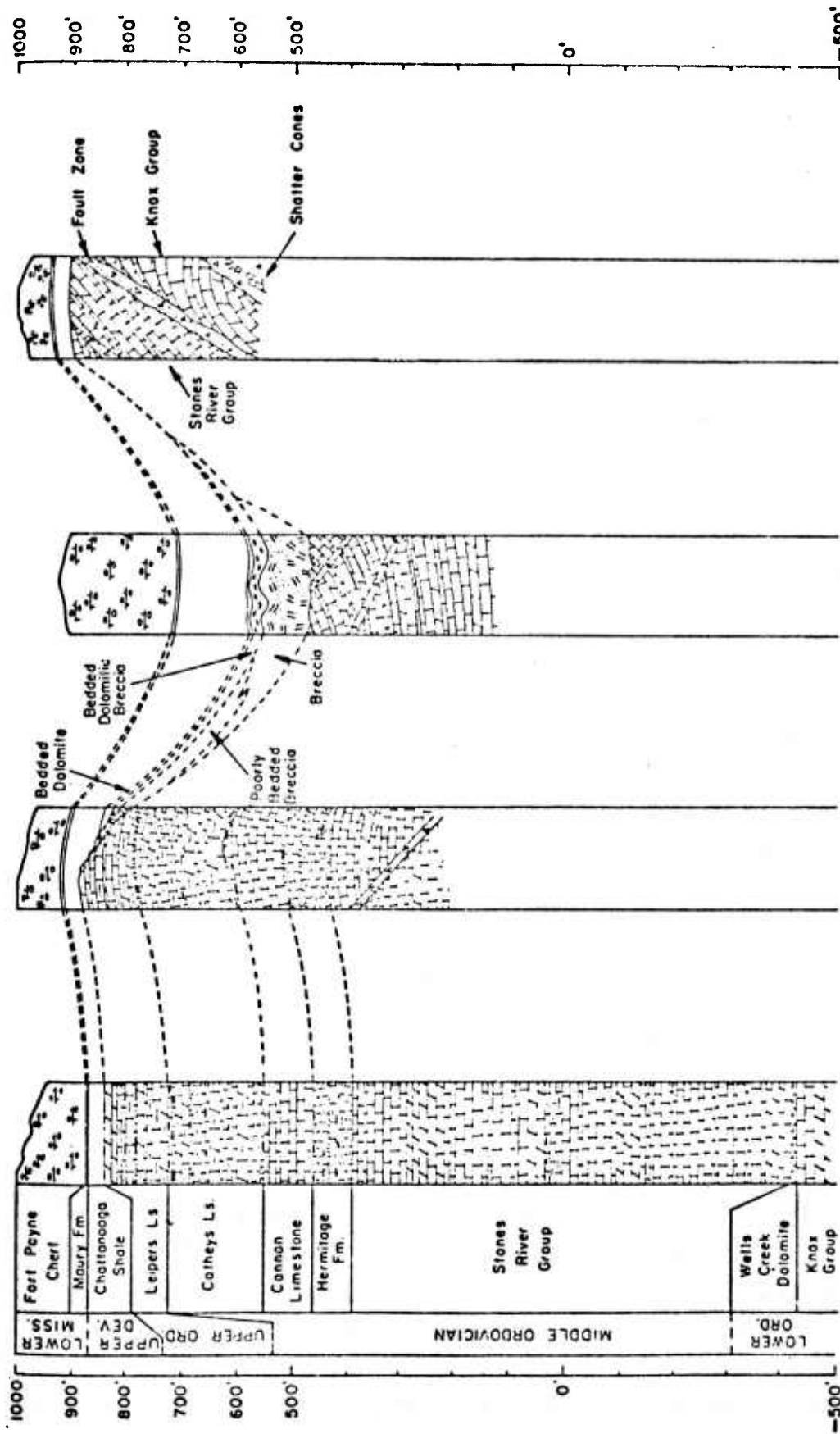


Figure 1. Generalized Stratigraphic Sections from the Western Side of the Flynn Creek Structure (after Roddy, 1968)

above its original position. Where the base of the mound intersected the bedded breccia on the crater floor, the hill was almost 3000 feet in diameter with sides sloping an average of 15°. Similar upward displacements of the material in central mounds were observed at the Wells Creek structure, Tennessee (Stearns, et al., 1968); Sierra Madera, Texas (Howard, et al., 1972); and Gosses Bluff, Australia (Milton, et al., 1972).

Some evidence of inward displacements at depths also existed in many of the structures. Howard, et al., (1972) suggested that individual beds in the Sierra Madera uplift were faulted and folded to an extent that the total strike length of each bed was greater than the perimeter on which it lies. This shortening may have been as great as 25 percent in some stratigraphic sections, although this estimate was based on the possibly invalid (Milton and Roddy, 1972) assumption that the displacement of each segment could be resolved into translation plus rotation about no more than one axis. Also, stratigraphic beds appeared to have been thickened such that near-vertical beds, which were no more than 1200 feet thick, filled a minimum width of 5000 feet.

The orientation of shatter cones (shatter cones will be discussed later) has also been used as a measure of inward displacement (Milton, et al., 1972). Measurements of such orientations at Gosses Bluff indicated that when a common shock focus was assumed inward displacements were from 20 to 52 percent of the original radial distance from the center, with the deeper strata displaced inward more than the shallower strata. However, these estimates could be significantly reduced if the shock was produced by a vertical line source. A complete elimination of inward displacements would require that the line source was 6300 feet long. If the relation that upper beds moved inward relative to lower, as suggested by Howard, et al., (1972) based on fold patterns at Sierra Madera, is also valid at Gosses Bluff, then the assumption of a common source results in an incorrect relation of displacements between strata, and quantitative estimates that are based on that assumption are not valid.

While evidence of inward displacements in the deeper regions is not complete, outward displacements in much shallower regions are observed. For example, at Gosses Bluff the upper ends of layers lie as overturned plates or detached blocks on the truncated edge of stratigraphically higher units (Milton, et al., 1972). In addition, 330 foot long blocks of sandstone lie 1000 feet from their stratigraphic outcrop, indicating an outward ballistic flight.

The peak shock pressures experienced by the material in central mounds can be estimated on the basis of the occurrence of shock effects. One macroscopic shock effect, already mentioned, is the shatter cone. Dietz (1968) describes shatter cones as cup-and-cone structures with striated surfaces that radiate from small half-cones on the face of a master cone. They are most common in carbonate rocks, but are also known in shale, sandstone, quartzite, and other lithologies. They frequently occur in central uplifts, as shown in table 1, indicating that conditions favorable to shatter-cone formation are experienced in that material. A theoretical study of shatter-coning (as reported by Dietz, 1968) shows that shatter cones are shock fractures formed along a travelling boundary between the plastic and elastic response of a material defined by the dynamic elastic limit, with the plastic domain moving relative to an elastic domain. The analysis is consistent with the observations that shatter cones appear to be formed prior to significant material displacement, and high-pressure phases (coesite, stishovite, maskelynite) have not been found associated with shatter cones. Thus, shatter cones, and by association central mounds, appear to be formed in material where the shock pressures were close to, but above, the Hugoniot elastic limit.

Table 1
STRUCTURES WITH SHATTER CONES IN CENTRAL UPLIFT
(Dietz, 1968)

<u>Structure</u>	<u>Location</u>	<u>Rock type of shatter cones</u>
1. Steinheim Basin	Germany	Limestones
2. Wells Creek Basin	Tennessee	Dolomite
3. Crooked Creek	Missouri	Limestone
4. Serpent Mound	Ohio	Limestone
5. Flynn Creek	Tennessee	Limestone
6. Sierra Madera	Texas	Limestone
7. Verdefort Ring	South Africa	Granite
8. Clearwater Lake West	Quebec, Canada	Granitic Gneiss
9. Sudbury	Ontario, Canada	Quartzite, Shale, Granite
10. Manicouagan-Mushalagan	Quebec, Canada	Crystalline Gneisses
11. Gosses Bluff	Australia	Limestone, Sandstone, etc.

An extensive study of circular structures that have effects consistent with hypervelocity impact sites has led Dence, et al., (1968) to conclude that there is a critical crater size required to form central uplifts in granitic gneisses. Information from structural mapping, gravity surveys, and drilling, combined with evidence of previous shock-wave experience in materials, has indicated that there are at least 12 shock-produced craters on the Canadian Shield. The smaller of these craters, with diameters of 2.5 miles or less (Brent, Holleford, New Quebec craters), have a bowl-shaped structure with no central uplift. The craters with diameters greater than 5.5 miles (Deep Bay, Clearwater Lakes, Carswell Lake), however, show a complex structure which includes a central uplift, an annulus of brecciated rock, and a peripheral depression which surrounds the crater.

Observations of the occurrence of central mounds on the Earth, Mars, and the Moon have been interpreted to show that gravity has an influence on the occurrence of central peaks (Hartmann 1972, 1973). Hartmann (1972) suggested that data on the size distribution of craters with central peaks as a function of crater diameter (figure 2) indicated that central peaks tended to

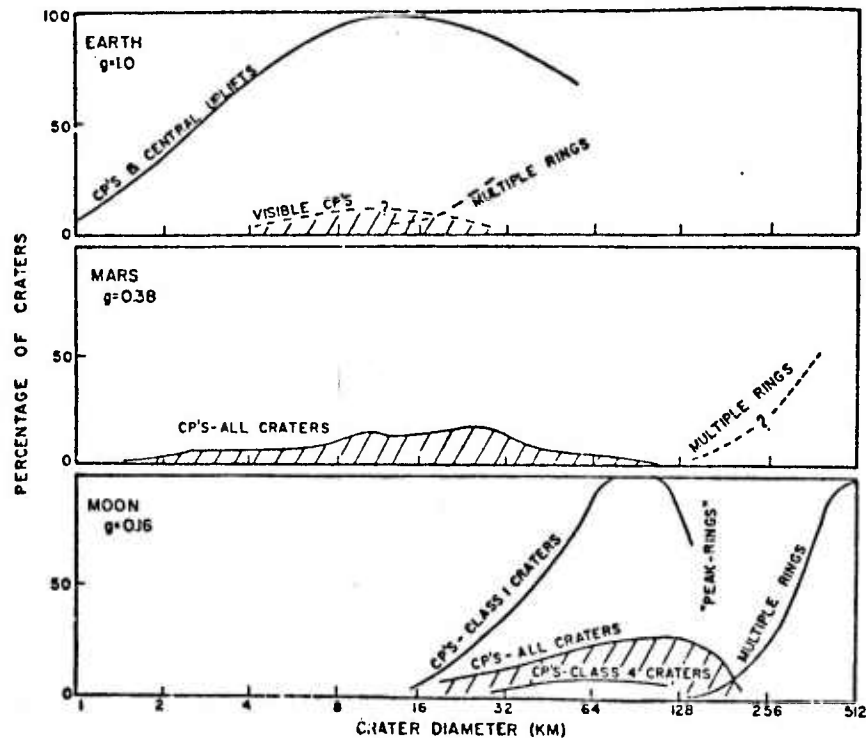


Figure 2. The Size Distribution of Craters with Central Peaks on the Earth, Mars, and the Moon (Solid line on earth data includes structural uplifts in astroblemes and is based on a total of 33 structures (after Hartmann, 1972)

form in craters of smaller diameter as gravity increased; although the statistical base for the Earth data was only 33 cryptovolcanic structures. He suggested the relationship was

$$D_c \propto g^{-1.25 \pm 0.2}$$

where g was the gravitational acceleration and D_c represented either the minimum diameter for craters with central peaks or the diameter of craters with the maximum frequency of central peak occurrence. The data also showed, however, that the inferred minimum diameter of craters with central peaks was significantly different from the diameter at maximum frequency. This difference indicated that gravitational stress, while a contributory factor, was not the only cause of central mound formation.

b. Central Mounds in High Explosive Detonation Experiments

Similar structural relations have been observed at central mounds in craters caused by large chemical-explosive detonations. One series of tests was located at the Watching Hill Test Range near Suffield, Alberta, and was sponsored by the Defense Research Establishment of Canada. Programs during this series included SNOWBALL, DISTANT PLAIN, PRAIRIE FLAT, and DIAL PACK. The geology at the test range was characterized by a ground water table usually near 25 feet depth (Zelasko and Baladi, 1971). The presence and depth of this water table resulted in essentially a two-layer structure. The material above 25 feet depth was a low-density soil that displayed a Mohr-Coulomb yield surface with a slope near 1. The material below 25 feet depth was a denser, saturated soil that, for confining pressures less than 40 bars, had little strength dependence on confining pressure. Also, the Poisson's ratio of the material increased from 0.30 near the surface to 0.47 at 30 feet depth.

Central peaks with characteristics similar to the central uplifts observed in ancient impact structures were formed in many of the craters that resulted from the explosive tests. Roddy (1968) described the crater (figure 3) from the 500-ton TNT event, SNOWBALL, as shallow and flat-floored with a diameter of more than 300 feet and a maximum depth of 22 feet. The central mound, which was nearly 19 feet high, consisted of folded and faulted clay beds in a tightly folded dome. The beds showed plastic thickening and thinning with a stratigraphic horizon lifted nearly 24 feet. During the test series at Suffield,

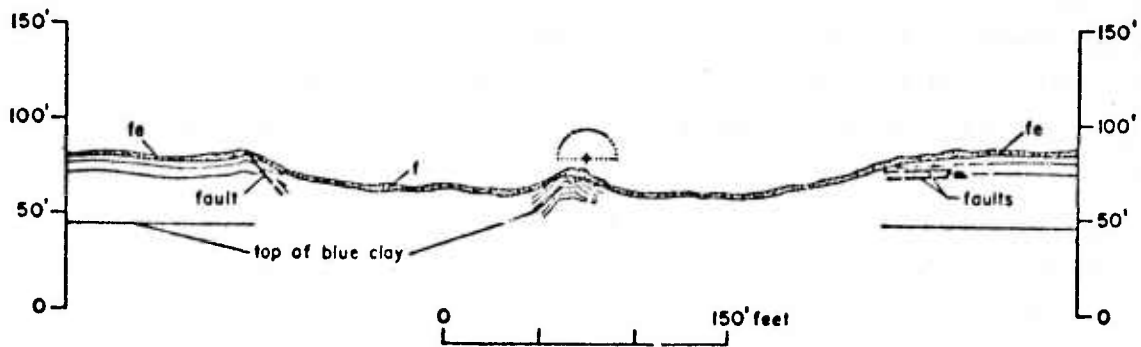


Figure 3. Cross Section of the Crater Produced by the 500-Ton TNT Event SNOWBALL (after Roddy, 1968)

a 20-ton spherical charge and a 100-ton hemispherical charge formed craters with no central peaks, while a 100-ton spherical charge and 500-ton hemispherical and spherical charges formed craters with central mounds (Milton and Roddy, 1972).

A series of high-explosive detonations, named MIDDLE GUST, was performed near Pueblo, Colorado, during 1971 and 1972 (Myers, 1973). This series included a total of five experiments at two sites (see table 2). One site had a 10-foot

Table 2

DEFENSE NUCLEAR AGENCY HIGH EXPLOSIVE EXPERIMENTS

<u>Experiment</u>	<u>Charge (tons TNT)</u>	<u>Charge position</u>	<u>Test side</u>	<u>Central mound</u>
MIDDLE GUST I	20	half-buried	"wet" shale	2 ft
MIDDLE GUST II	100	elevated	"wet" shale	5 ft
MIDDLE GUST III	100	surface tangent	"wet" shale	trough
MIDDLE GUST IV	100	surface tangent	"dry" shale	2 ft
MIDDLE GUST V	20	half-buried	"dry" shale	3 ft
MIXED COMPANY I	20	half-buried	sandstone	3 ft
MIXED COMPANY II	20	surface tangent	sandstone	7 ft
MIXED COMPANY III	500	surface tangent	sandstone	5 ft

overburden of sandy clay over fractured clay shale that interfaced with competent shale 23 feet below the ground surface (Windham, et al., 1973). This site was called the "wet" site because a perched water table on the top of the competent shale extended to about 4 feet below the ground surface. Two sets of nearly vertical joints existed in the competent shale. The sets were nearly perpendicular and had intervals between joints of 6 to 8 feet and 10 to 14 feet. The second or "dry" site was 23 feet of fractured clay shale over a more competent shale with no near-surface water table. Three sets of nearly vertical joints existed in the weathered shale at the second site. The maximum strength of even the competent shale at both sites was less than 100 bars and independent of confining pressure. All the craters extended into the weathered shale, and the MIDDLE GUST III crater reached the competent shale (Myers, 1973). All of the craters except MIDDLE GUST III had interior mounds that were 2 to 5 feet high, although the top of one of the mounds was offset from ground zero. The mounds tended to fracture along old joint directions (Roddy, 1973). The MIDDLE GUST III crater had a 5-foot deep central trough in the competent shale. Roddy (1973) reported shatter cones in the MIDDLE GUST IV and V central mounds.

An additional series of three high explosive detonations, called the MIXED COMPANY series, was performed near Grand Junction, Colorado, during 1972 (Choromokos and Kelso, 1973). The sites for these experiments were surface layers of alluvial sandy soil over sandstone with no significant water content. The alluvial soil layer was 5 feet thick for events I and III and 1.8 feet thick (Day, 1973) for event II. The sandstone was generally weathered to a depth of 12 feet below the surface.

The craters that resulted from these experiments all had central uplifts (Roddy, 1973). The first event produced a crater with an apparent depth of 15 feet and a central peak 3 feet high. The sandstone beds in this uplift were generally intact on the flanks but were brecciated in the core. The second event produced a crater with an apparent depth of 7 feet. A very large central mound covered the crater floor and extended nearly 3 feet above the original ground level. The third event produced a crater with an apparent depth of 18 feet and a poorly formed irregular dome of massive sandstone 5 feet high. The crater floor surrounding the uplift consisted of large slabs of sandstone that sloped upward towards ground zero and exhibited both fracturing and faulting approximately parallel to the local joint pattern. A circular ring

fault formed on the crater floor at the base of the crater walls, locally separating the floor from the walls. Carnes (1973a) reported that permanent displacements in the sandstone beyond the crater walls were primarily upward and outward.

c. Craters Without Central Peaks

Central mounds were not observed in all shock-produced craters. In particular, there was a notable lack of central peaks produced by nuclear detonations at the Nevada Test Site (Roddy, 1968) and at Eniwetok and Bikini Atolls in the Pacific (Circeo and Nordyke, 1964). Such nuclear experiments included detonations with yields from a kiloton to over 10 megatons and deeply buried, near surface, and above surface shotpoint locations. The test sites were dry alluvium at the Nevada Test Site and unconsolidated sands and gravels over coral reefs in the Pacific. The common geologic characteristic of these sites is the porous structure of the cratered materials. The medium beneath the Barringer Crater in Arizona, a meteorite impact crater with no central mound, is porous sandstone (Shoemaker, 1963). Also, craters without central mounds were produced in impact craters formed in dry, non-cohesive quartz sand during laboratory tests (Gault, et al., 1968).

2. PREVIOUS CALCULATIONAL PROGRAMS

Several attempts have been made by others to numerically simulate shock-wave cratering events. These attempts have shown that the ground-motion history during a simulation was sensitive to the amount of material compaction that was modeled for a complete cycle of stress loading and unloading. A second important feature of the simulations was that the motion caused by the simulated shear wave was toward the axis of symmetry.

a. Distant Plain 6 Simulation

The coupled Eulerian-Lagrangian computer code called ELK was used for three attempts to numerically simulate the crater and central mound produced by the 100-ton, surface-tangent high-explosive experiment, Distant Plain 6 (Christensen, et al., 1968; Christensen, 1970). The material models for all three of the calculations were based on reported test-site data; however, only one of the simulations, ELK 31, included a precompaction model beneath, and as a result of, the 100-ton explosive charge. The ELK 31 calculation was continued until a simulated time of 220 msec (figure 4) and showed the development of upward velocities near the axis of symmetry after 160 msec. At 220

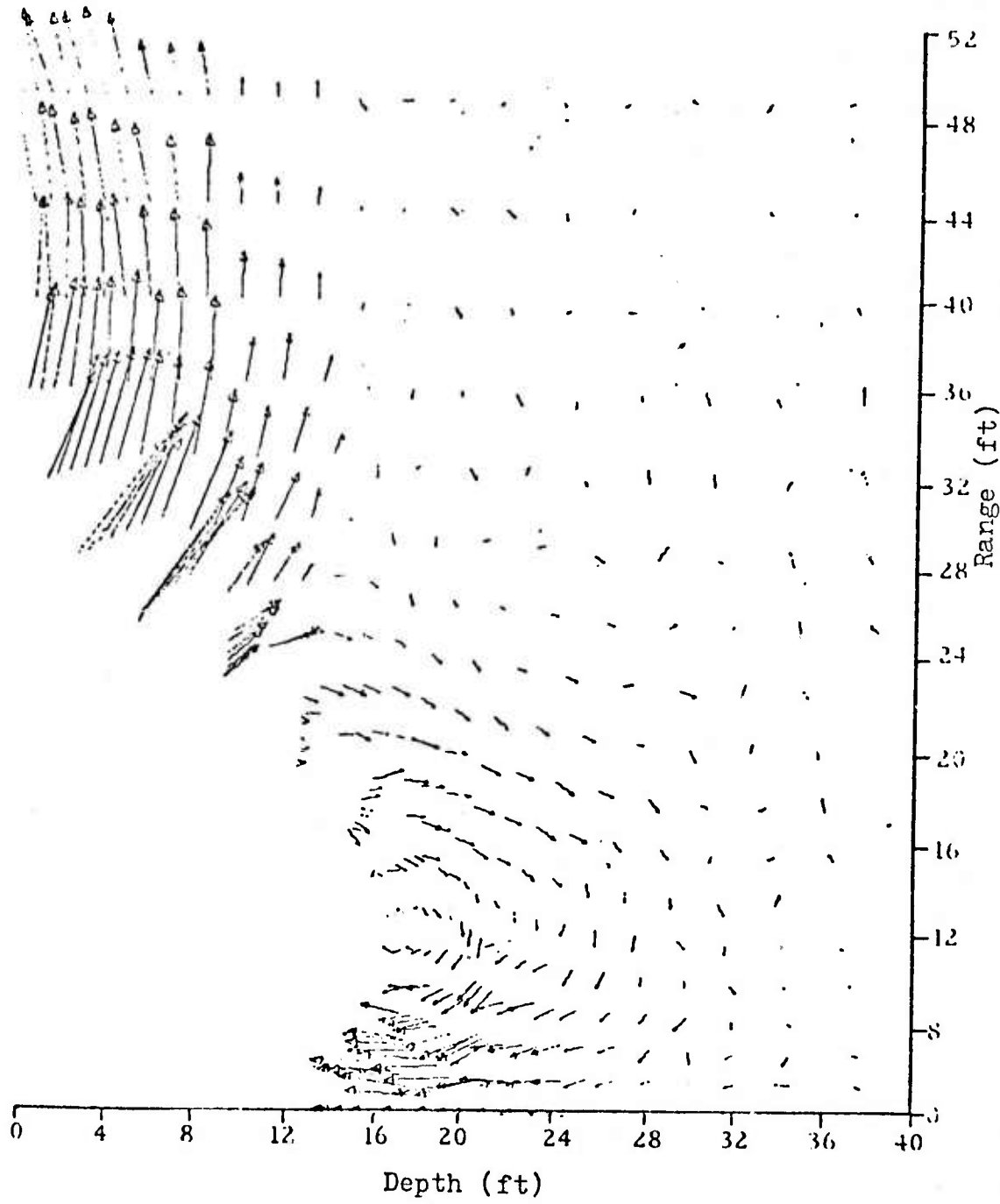


Figure 4. Velocity Vectors at a Simulated Time of 220 msec for the DISTANT PLAIN 6 Calculation (after Christensen, et al., 1968)

msec, the flow pattern showed that material near the crater boundary at the 20-foot range was moving down and toward the vertical axis. This motion resulted in a vortex pattern centered at a range of 12 feet. Extension of this flow pattern, accomplished by extrapolating deceleration, resulted in calculated crater dimensions at a simulated time of 1 second that were consistent with the observed crater. The other two calculations were stopped by a simulated time of 125 msec because the computed depths of the craters were too great. Christensen (1970) concluded that causes for the upthrust included the airblast-induced shear wave interacting at the axis of symmetry, the effect of gravity, and the compaction cone that resulted from quick settlement under the 100-ton explosive load, but he did not determine the contribution of each cause.

b. Mine Under Simulation

A numerical simulation was also accomplished to model the test event MINE UNDER (Maxwell and Moises, 1971a). The event was the detonation of a 100-ton spherical charge of TNT over granite. The charge was centered at a height of 2 charge radii to produce only airblast loading on the ground. The test site was composed of weathered granite with a compressional wave speed of 10,000 ft/sec and a shear wave speed of 6100 ft/sec. Sample porosities varied a factor of 2 from a mean value of 5 percent. This porosity resulted in a residual compression, after a cycle of compressive loading and unloading, of 20 percent of the peak compression for peak pressures below 43 kbar. A complex yield model which included brittle fracture and sliding on cracks was also included in the calculation, with a von Mises limit of 30 kbar reached by a pressure of 24 kbar. The results of this calculation showed that the calculated shear wave, supported by the strong rock model, caused a clockwise rotation in the material flow pattern. However, data from instrumentation in the actual event did not indicate such a substantial shear wave. Maxwell and Moises concluded that the in situ rock strength was much lower than the strength included in the model.

c. Sierra Madera Simulation

A numerical simulation of the event which may have formed the Sierra Madera formation was also accomplished by Maxwell and Moises (1971b). For this simulation a sphere with a radius of 328 feet and a velocity of 19 miles/sec was assumed to impact vertically on a halfspace. Both the sphere and the halfspace were assumed to be composed of the same material, which had an assumed density of 2.7 gm/cc. The parameters of the material equation of state were

based only on Hugoniot data for basalt. The yield model was a 0.2-kbar von Mises limit until a calculational zone experienced zero pressure, after which that zone was assumed to have no shear strength. The calculation resulted in upward velocities below the impact point by a simulated time of 5.5 seconds with a toroidal flow pattern developed by 9.5 seconds that continued until the calculation was terminated at 30 seconds. Maxwell and Moises concluded that the dominant driving force of the central uplift was the release of the overburden by excavation. The entire flow pattern after 5.5 seconds, however, could be explained by the flow of a liquid under the influence of gravity.

d. Nuclear Explosion Simulation

A series of calculations, called REVROC, was completed at the Air Force Weapons Laboratory (AFWL, 1973) to study the effects of layered bedrock on calculated near-surface ground motions caused by a simulated nuclear explosion. A two-dimensional, axisymmetric computer code was used for the simulation. Material models included irreversible compaction after a cycle of loading and unloading. The results showed that, by 0.5 second, the calculated flow field included upward motion near the vertical axis of symmetry. These motions seemed to be caused by the primary shear wave and occurred even in the bottom layer of material. Also, the motions were a function of the amount of irreversible compaction included in the model, with less compaction favoring more upward motion.

e. MIDDLE GUST III Simulation

Port and Gajewski (1973) performed a numerical parametric study to examine the causes of major discrepancies between the ground motions calculated using pretest models of the MIDDLE GUST III event and ground motions measured during the experiment. The main discrepancy was the failure of the numerical calculations to simulate accurately the arrival and magnitude of the large direct-induced ground shock which dominated the experimental motion. Three alternate material models were evaluated in their calculations. The first, or laboratory, model was based on detailed laboratory uniaxial-strain tests on samples of materials obtained from site drill cores. The second, or CIST, model was based on cylindrical in situ test results of the MIDDLE GUST site. The CIST test was used to determine dynamic moduli of in situ materials by measuring the ground motions caused by a cylindrically symmetric shock input (Davis, 1973). The third model was based on seismic velocity data of the site and was referred to as the seismic model. The first two models included

irreversible compaction after a load-unload pressure cycle, while the seismic model was incompactible. The velocities of large-amplitude stress waves implied by the models were lowest for the laboratory model and highest for the seismic model. The same equation of state was used for high pressures in all three models.

The results of the parametric study showed that the laboratory model was inadequate. That model resulted in wave speeds that were one-third to one-fourth of the values required to match the arrival time of strong ground-motion signals. Further, that model failed to produce the magnitude of the peak upward velocities near the surface caused by the direct-induced wave (figure 5). The shock arrival times that were measured above 23 ft depth were most consistent with the CIST model calculation. The data from instruments placed below 23 feet indicated wave speeds greater than even the seismic model. The peak upward velocities near the surface were matched only with the seismic model. The crater profiles predicted for all three models were nearly the same, with a maximum depth below ground zero near 17 feet, while the observed depth was 21 feet.

3. POSTULATED MECHANISMS

Several mechanisms have been proposed to explain the formation of central peaks. These mechanisms may be broadly divided into (1) effects related to stress waves and (2) rapid gravitationally controlled adjustments of the walls of an initial crater. The first of these broad divisions includes rebound, stress wave reflections, shear wave effects, and special boundary conditions caused by the impact of low-density bodies. The second division includes deep gravitational sliding and Rayleigh jet formation.

a. Stress Wave Related Mechanisms

The rebound of material below the crater following the compression by the shock wave was suggested by Boon and Albritton (1938) as the primary mechanism for forming central mounds. This rebound results from the acceleration of material toward the stress wave source as a result of the decreasing stress gradient that extends to the free surface. Baldwin (1963) used a set of two very small-scale explosive experiments to examine this mechanism. In the first, a 40-grain dynamite charge was detonated 1 inch below the surface of a specially built-up volume of soil. A box 3 feet square and 1 foot deep was filled with soil. The bottom 6 inches consisted of ordinary soil. Above

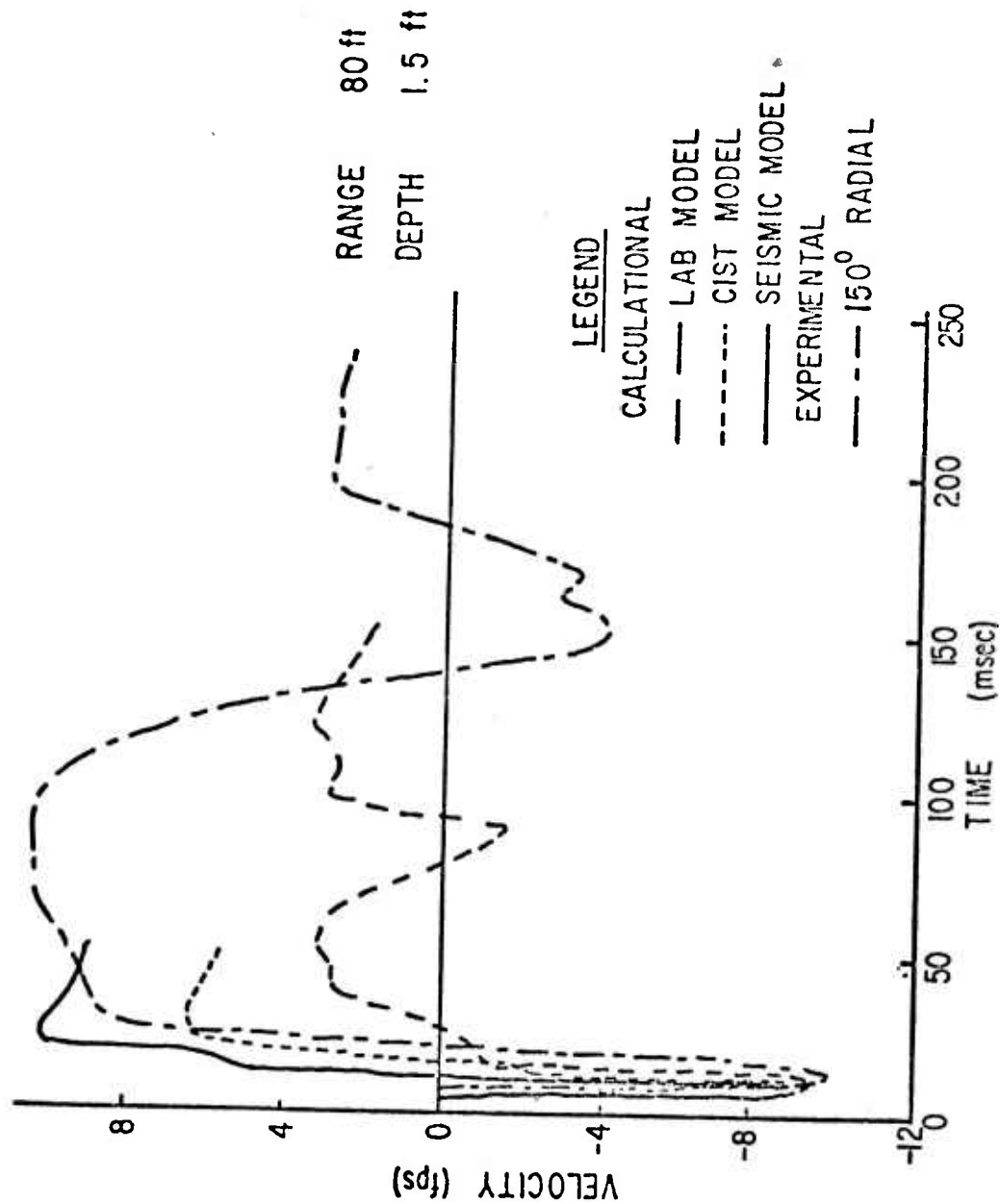


Figure 5. Vertical Velocity Comparison between MIDDLE GUST III Experimental Measurement and Three Material Models (Termination of model lines indicate end of calculations; positive velocities indicate upward motion (after Port and Gajewski, 1973))

this soil were six horizontal layers of colored soil, each 1-inch thick, with each layer lightly tamped into place. The second test was a repeat of the first with the soil colored into vertical layers. From these two tests, a composite crater (figure 6) was determined. Baldwin concluded that a flat area

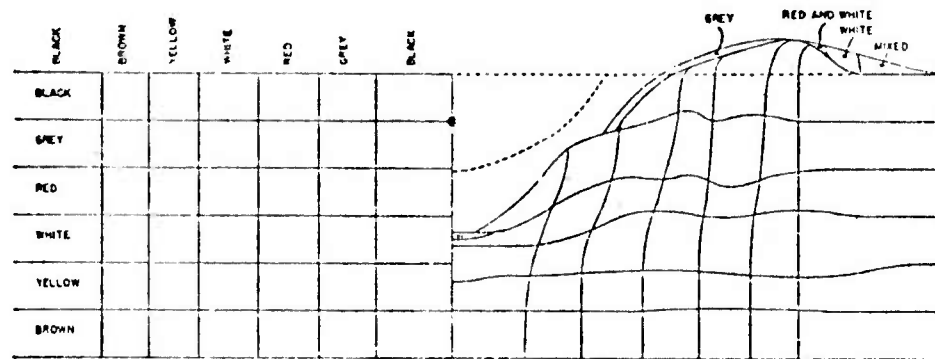


Figure 6. Composite Crater Profile Constructed from the Detonation of Two 40-Grain Dynamite Charges with the Shot Point at the Base of the Black Layer (The curved dotted line gives the limit of the volume from which the soil was actually blasted from the crater; the lens at the bottom of the crater is white material of lower than original density (after Baldwin, 1963, pg. 120)).

in the center of the crater was an incipient central cone formed by rebound. This conclusion was reached because some of the horizontal white layer was found above the red layer and partially under the gray layer. This white material was of lower-than-normal density, while the yellow and white layers below it were denser than normal. Dence (1968) also mentioned that unloading of materials after the shock wave might influence central mound formation, but he did not emphasize this mechanism because of the small increase in specific volumes for materials subjected to shock pressures of less than 100 kbar.

Short (1965) proposed the reflection of stress waves from material discontinuities as an explanation for the occurrence of central peaks. This mechanism was based on the partial reflection of the initial shock wave from surfaces where the acoustic impedance changes discontinuously. These reflected waves, upon returning to the crater, would reflect again from the free surface as tensile waves, producing an upward heave that would be maximum near the center. Short also suggested that if such an effect did result in central

peaks, then the presence of such peaks on the moon implied at least a zone of higher acoustical impedance below the lunar surface.

As an example, Short made a limited calculation of the effect of this mechanism during the impact that formed the East Clearwater Lake crater in Canada. He estimated that the shock pressure from such an event would attenuate to a kilobar at a depth of 19 miles and if totally reflected would still be several hundred bars upon return to the crater base. Beals (1965) discounted this mechanism because much less than total reflection would occur. Beals based his conclusion on the tables of Muskat and Meres (1940), from which he inferred that for an elastic wave reflecting from the crust-mantle discontinuity only about 0.25 percent of the energy would be reflected.

The inward motion of material behind the primary shear wave has also been suggested as a cause of central peaks.* The motion behind that wave would force material into a smaller volume about the vertical axis through the center of the crater, because the shear wave would be symmetric about that axis. This squeezing effect would tend to cause upward velocities in a manner similar to squeezing toothpaste from a tube. This effect was evident in calculations similar to the REVROC study, which showed upward motions began where the calculated shear wave intersected the axis of symmetry. Also, as was noted earlier, Christensen (1970) observed this mechanism in the ELK 31 calculation.

Milton and Roddy (1972) suggested that the occurrence of a central peak in an impact crater may indicate a low-density impacting body such as a comet. They stated that a necessary condition for central peak formation may be the initial deposition of energy near the surface, and not at some depth. This condition may be required because central peak formation depends on a complex interaction of the shock wave with the free surface. If a major portion of the initial energy is deposited too deeply into the target material, the region that would have formed the central peak would become involved in the crater. A central peak would form in a cometary impact crater because the comet, consisting mainly of H₂O and CO₂ ices, would volatilize near the surface upon impact, while a meteorite would penetrate to some depth. They concluded that information on the percentage of impact craters with central peaks may indicate the ratio of large-scale cometary impacts to meteor impacts on the surface of a planet.

*Port, R. J., Air Force Weapons Laboratory, Personal Conference, 1973.

b. Gravitational Mechanisms

Several authors (Shoemaker, 1963; Dence, 1968; Gault, et al., 1968) have suggested that a cause of central peak formation is a deep sliding, or base failure, resulting from the gravitational stresses produced by the difference in height between the rim and the center of a crater. Dence (1968) referred to a solution (figure 7), which showed that under a valley with walls

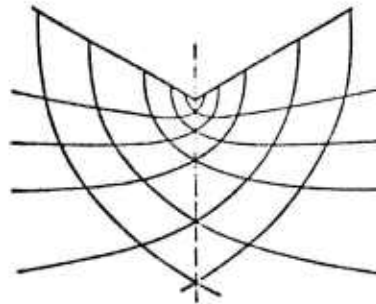


Figure 7. Theoretical Lines of Slip under a Valley with Sides Dipping at 30° to the Horizontal (after Dence, 1968)

sloping at 30° the earth movement would occur along slip lines that form two families of parabolas with the bottom of the valley as the focus and the apices within the moving material. In the cratering case, Dence assumed the slip lines would be replaced by coaxial surfaces that retained the upward turning beneath the center of the crater. Motion along these slip surfaces would be resisted by the shear strength of the medium. There would, therefore, be a minimum crater size for any medium below which no such motion could occur. He described the formation of a crater with a central mound as proceeding from a primary crater by the walls sliding down and in along deep slip surfaces forcing the material under the crater to bulge.

Dent (1974) has also considered the failure mode of the walls of a crater. These modes of failure are "slope failure" (in which the failure surface emerges in the crater wall) and "base failure" (in which the failure surface extends deeply below the bottom of the crater). He accomplished an elastic plane-strain analysis of the stresses caused by the excavation of a semicircular cavity at the surface of a two-dimensional halfspace in a gravitational field. He concluded that with a Mohr-Coulomb failure criterion the slope-failure mode would be preferred for any size of excavation.

Pike(1971) suggested that central peaks may be caused by the centripetal movement of collapsed rim material similar to the Rayleigh jet produced in the transient craters in a liquid medium. Harlow and Shannon (1967) have numerically simulated the splash of liquid drops into deep pools, showing the development of these splash jets in incompressible fluids. Their results showed that the development of the central jet was caused by the gravitational collapse of the sides of the crater into the crater void provided that the scale condition $(gR)^{1/2}/U_0$ was less than 0.4 where g is the gravitational acceleration, R is the radius of the impacting drop, and U_0 is the impact velocity. However, these results were changed significantly when compressibility and shock processes were involved, with the process reverting to the rebound mechanism already described (Amsden, 1966).

Section III

NUMERICAL SIMULATION OF SHOCK WAVE CRATERING

The high-explosive cratering experiments provided excellent opportunities to examine the causes of central mound formation through numerical simulation because (1) the preshot material properties of the medium were extensively tested, (2) the test conditions were known, and (3) the post-event structure of the craters and central mounds were carefully documented to provide strong constraints on the numerical results. The MIXED COMPANY II event served as a particularly useful experiment because of the large size of the central mound compared to the size of the crater. This large size indicated that the central mound processes were particularly effective in this test event and reduced resolution problems associated with numerical calculations. Therefore, a series of numerical experiments was undertaken to simulate the MIXED COMPANY II event and determine the contribution of individual mechanisms to the formation of the central mound. The results showed that the calculation of upward motions below a simulated crater was dependent on the material compaction model in the region where strength effects were significant. The results of one numerical simulation indicated that the presence of a lower "fluid" material may also cause the formation of a central mound.

1. MIXED COMPANY II EXPERIMENT

As previously stated, the MIXED COMPANY II experiment was the detonation of 20 tons of TNT, arranged in a spherical charge of 4 feet radius, placed above, and tangent to the ground surface. The MIXED COMPANY test site consisted of a thin deposit of sandy clayey silt over a 70-foot thick section of Kayenta formation (Ehrgott, 1973). The silt, which was 1.8 feet thick at the MIXED COMPANY II test site (Day, 1973) appeared to become slightly cemented at depth. The Kayenta is a fluvial deposit that consists of lenticular to irregularly bedded layers of fine-to-medium-grained sandstone, siltstone, and conglomerate with occasional layers or lenses of shale. The calculational models of these material were based on properties determined from laboratory and CIST data from the site* and are given in table 3. This information divided the test

*Gajewski, R., Personal letter and data, Air Force Weapons Laboratory/DEV, Kirtland AFB, NM, 1973.

Table 3
MIXED COMPANY II SITE MODEL*

<u>Property</u>	<u>Layer</u>			
Depth to top (ft)	0.0	1.8	11.2**	19.6+
Density (gm/cc)	1.875	2.35	2.47	2.35
Compressional wave speed (ft/sec)	500	8000	9000	8000
Rarefaction velocity (ft/sec)	1500	16000	18000	16000
Volume fraction of air filled voids	0.2366	0.0510	0.0229	0.0510
Poisson's ratio	0.25	0.20	0.25	0.20
Cohesion (bars)	0.7	68	51	68
Angle of internal friction (°)	25	35	37	45
Von Mises limit (kbar)	0.5	7.5	2.1	11.6

*Gajewski R., Personal letter and data, Air Force Weapons Laboratory/DEV, Kirtland AFB, NM, 1973.

**Changed to 11.4 ft in calculations

+Changed to 19.2 ft in calculations

site, to a depth of 60 feet, into a 1.8-foot layer of alluvium over a halfspace that had three layers. The properties indicated that the material below the soil had a much higher maximum yield strength than the shales in the MIDDLE GUST experiments.

Observed crater morphology and structural information provided the primary constraints on the numerical simulation of the MIXED COMPANY II experiment. Detailed profiles (figure 8) of the crater that was formed* showed that the apparent crater extended a maximum of 4 feet below the original ground level at a radius from ground zero of 12 feet. The crater was only approximately symmetric, with radii at the original ground level of 20 feet to the north and 22 feet to the south. The central mound, represented by true crater dimensions, extended a distance of 8 feet from the vertical axis through ground zero and was 7 feet high. The mound was composed of uplifted and brecciated sandstone (Roddy, 1973). A poorly developed overturned flap and thin blanket of ejecta surrounded the crater, and no fused material was found. Deformation in the

* Carnes, B. L., Personal letter and data, Waterways Experiment Station, U S Army Corps of Eng., Vicksburg, MS, 18 October, 1973b.

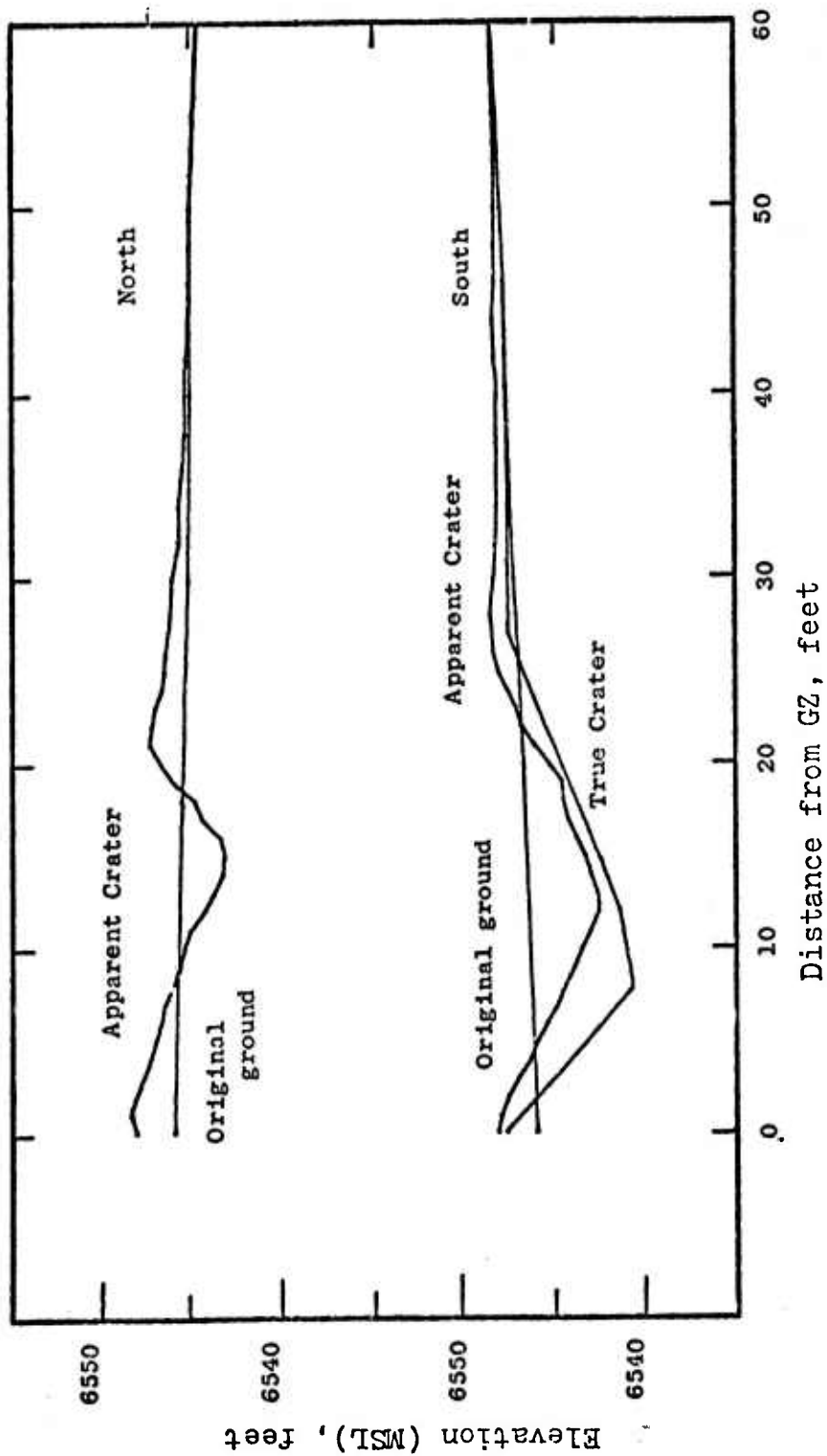


Figure 8. Apparent and True Crater Profiles of the 20-Ton TNT Event, MIXED COMPANY II (Carnes, B. L., Personal letter and data, Waterways Experiment Station, U. S. Army Corps. of Eng. Vicksburg, MS, 18 October, 1973b)

crater wall and rim consisted mainly of shattering and local brecciation. A piece of color-coded grout, originally placed at 10 feet depth, was found 1 foot below the top of the central peak.* Ground shock instrumentation (Day, 1973) included vertical and horizontal acceleration gages at ranges of 54 and 70 feet and depths of 1.5 and 5 feet. Vertical and horizontal velocity gages were located at similar depths and ranges greater than 93 feet. The gage at 70 feet range and 5 feet depth indicated a shock arrival at 10 msec. All the data indicated that a large signal was transmitted in the material below the depth of 1.8 feet.

2. CALCULATIONAL MODEL OF MIXED COMPANY II

The numerical simulation of the MIXED COMPANY II experiment included the use of three mathematical models of the physical processes that were assumed to be important. The first was a model of the surface-pressure boundary condition to simulate the high-explosive detonation. The second was a computer code that modeled the initial response of the ground to the surface boundary condition. This code included approximations to physical relations and the properties of the materials at the test site. The final model was a simplified ballistic extension of the conditions that were calculated using the first two models.

a. Explosive Detonation Model

The explosive detonation was modeled with data from a solution of the airblast pressure as a function of range and time for a 100-ton explosive charge on a rigid halfspace.** This information was applied using a cube-root scaling procedure to provide a surface-pressure boundary condition for a 20-ton, surface-tangent event. The procedure was to scale the ranges and time of the calculation by the ratio $(100/20)^{1/3}$, apply the boundary condition, and then rescale range and time by the inverse ratio.

b. Ground Response Model

The initial response of the ground was modeled with the AFTON-2A computer code (Niles, et al., 1971). This code models two-dimensional, axisymmetric

*Personal conference with Major Lamping of the Air Force Weapons Laboratory in March, 1973.

**Data supplied by the Air Force Weapons Laboratory, see Port and Gajewski, 1973.

continuum mechanics problems using elastic-plastic material models that simplify to hydrodynamic expressions at high internal energies. The theory of this code (see appendix B) is based on a specific method of constructing finite-difference approximations to the laws of continuum mechanics in integral (but not necessarily Lagrangian) form that includes artificial viscosity (von Neumann and Richtmeyer, 1950) to treat strong shock waves. This method uses relations to describe mass conservation, momentum conservation, and the first law of thermodynamics that combine to describe also energy conservation exactly. AFTON-2A is used frequently in ground-shock calculations (see, for example, Port and Gajewski, 1973), and the numerical errors associated with the code have been investigated extensively (Cooper, 1971; Trulio, et al., 1967). All the calculations accomplished during this study used a Lagrangian coordinate system unless specifically stated.

The code provides information in three forms. One form, termed a data edit, is a printed listing of selected parameters at each calculation point. The second form, called a restart dump, is a listing on magnetic tape of all the information necessary to continue the calculation from the time of that dump. While the primary purpose of this form is to provide a restart capability, these dumps also provide the information required to construct displays, termed flow field plots, of the conditions that exist in the calculation space at the simulated time of each dump. The third form is complete time history information of 100 selected "target" points. These "target" points may be considered to be "perfect" instruments which measure the forces and responses of a mass particle without influencing the behavior of that particle. They are points that may be located at any position in the calculational space, not just at calculational meshpoints, and move in a Lagrangian manner.

A description of the calculation grids is required to understand the later ballistic model and information representations. The quantities in this code are computed on two separate, but related, grids. Motion quantities (such as acceleration, velocity, and position) are computed at the designated calculation, or grid, points. Thermodynamic variables (such as stresses, strains, and internal energy) are computed at the interior of the volume defined by the four surrounding grid points. Thermodynamic quantities are, therefore, computed and represented on a thermodynamic mesh. The combination of the two grids divides the volume surrounding the calculation point into four quarter-volumes with

associated quarter masses. These quarter-volumes are also used in a ballistic extension to the code results.

The boundaries of the grid were the surface boundary, the axis of symmetry, and two transmitting boundaries (Niles, et al., 1971). The transmitting boundaries were imposed at 60 feet depth and 551 feet range and had no significant influence on the calculated motions.

One of the basic relations used to describe the material properties is the equation of state, which related pressure, P , to material density, ρ , and specific internal energy. The general equation of state for the material models of the MIXED COMPANY site was

$$P = f(u, u^*) \quad (1)$$

where the excess compression, u , was defined as

$$u = \frac{\rho - \rho_i}{\rho_i} \quad (2)$$

with ρ_i the initial material density and u^* the maximum excess-compression ever calculated at a thermodynamic mesh point. This functional relationship was divided into a low-pressure region, for u less than or equal the volume fraction of air-filled voids, and a high-pressure region. Effects of internal energy on relation (equation 1) were included by adding the term Ae (e is the specific internal energy and A is a constant assumed to be 3×10^{-12} gm/erg) to both u and u^* . For all calculations, the effect on pressure of this addition was small. This equation of state is a generalization of the seismic model (Port and Gajewski, 1973) to allow for a permanent compaction, as in the CIST model.

The low-pressure equation of state was further divided into a loading relation, for u equal u^* , and an unloading relation, for u less than u^* . The loading relation was

$$P = K_L u \quad (3)$$

where

$$K_L = \rho_i c_p^2 \frac{(1+v)}{3(1-v)} \quad (4)$$

defined K_L for each layer from the initial density, the compressional wave speed, c_p , and the Poisson's ratio, v , of the material. The unloading relation allowed for a linearly changing derivative of the equation of state through the relation

$$\frac{dP}{du} = \left[K_u u_x (\beta - 1) + K_u u + K_v (u_x - u) \right] / \beta u_x \quad (5)$$

for $(1 - \beta) u_x \leq u \leq u_x$

where

$$u_x = \min \left\{ \begin{array}{l} u^* \\ u_3 \end{array} \right\} ; \quad \beta = \frac{2K_L}{K_u + K_v}$$

and u_3 represented the volume fraction of air-filled voids. The parameter K_u was defined by the relation (equation 4) where c_p was replaced by the sonic velocity at the initial release of pressure, c_u ; and K_v was defined by the same relation with the sonic velocity as the pressure approaches zero, c_v . The unloading hydrostat was then

$$P = \frac{K_u \left[(\beta - 1) u_x + u \right]^2 - K_v (u_x - u)^2 + K_v (\beta u_x)^2}{2\beta u_x} \quad (6)$$

after integration of equation 5. For u less than $(1 - \beta)u_x$, the pressure-density relation was assumed to be

$$P = -K_v \left[(1 - \beta) u_x - u \right] \quad (7)$$

with the material in tension.

The low-pressure region allowed for a reduction in the specific volume of the materials after a complete cycle of loading and unloading (figure 9). The amount of this reduction was defined by the ratio β and the maximum

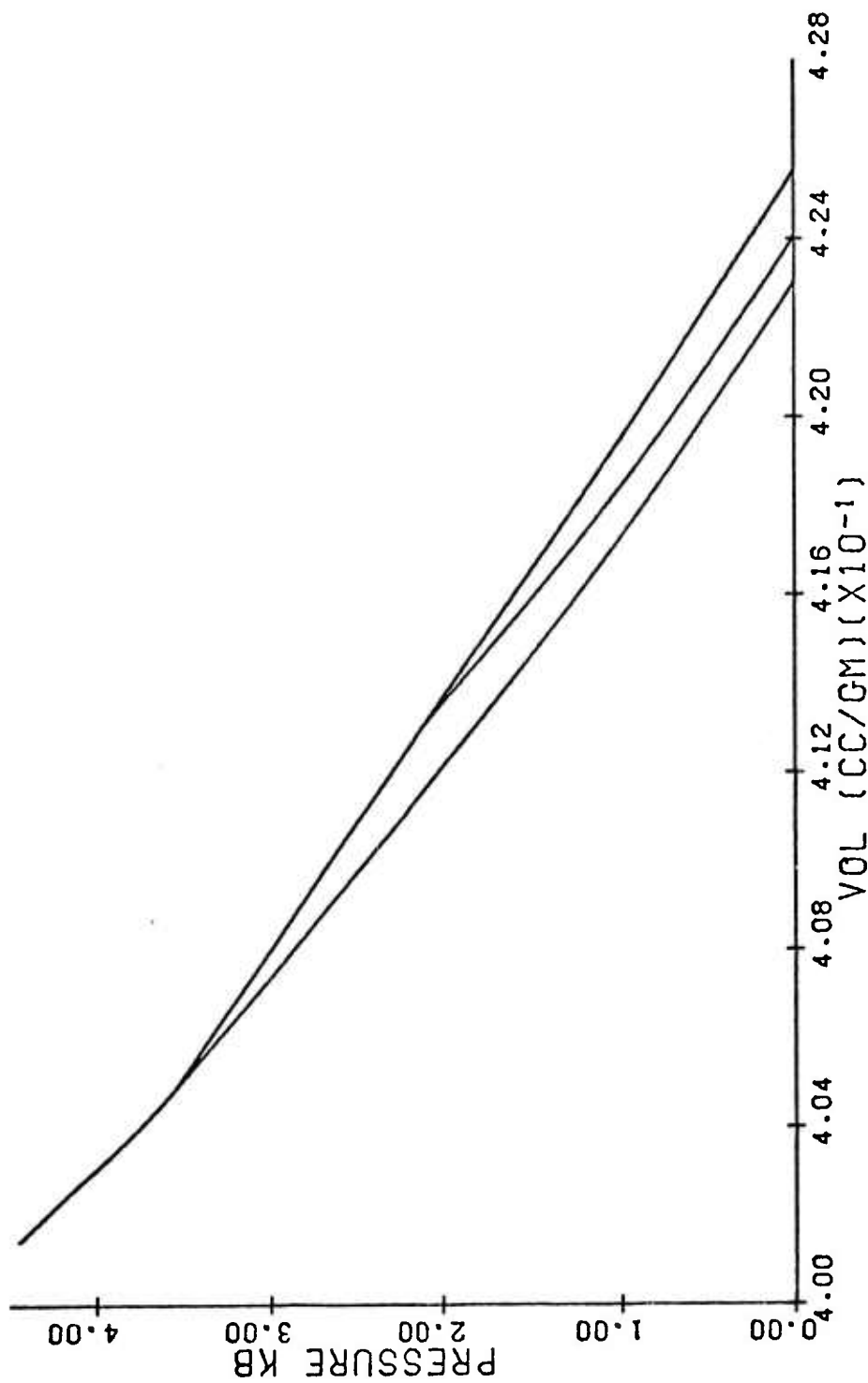


Figure 9. The Model Pressure--Specific Volume Relation in the Low-Pressure Regime for Layer 2 (Shown are the loading relation and unloading relations for u^* less than u_3 and u^* equal to or greater than u_3)

compression experienced within the low-pressure region. The parameter defined as

$$C = (1 - \beta) \quad (8)$$

was the compactibility of a material. By transformations to specific volumes, the relation

$$\frac{v_i - v_0}{v_i - v_x} = \frac{v_0}{v_x} C \approx C \quad (9)$$

where v represents specific volume and v_0 is the zero-pressure specific volume after a load-unload cycle, allows the compactibility of a material model to be estimated from graphs of pressure vs. specific volume. Initial calculations, which used the rarefaction velocity from the site data for c_u and c_v , failed to produce motions consistent with central mound formation. In the MIXED COMPANY II numerical simulation these values for the three deepest layers were reduced to

$$\begin{aligned} c_v &= c_L \\ c_u &= c_L + 1000 \end{aligned}$$

which implied a compactibility of approximately 10 percent in those layers. The results of subsequent parametric calculations showed the effects of variations in these two parameters.

The high-pressure equation of state was assumed to be independent of u^* , which resulted in one relation describing both loading and unloading. The derivative of the equation of state in this region was expressed by

$$\frac{dp}{du} = K_m - (K_m - K_u) \exp\left(\frac{u_3 - u}{u_s}\right) \quad (10)$$

where K_m and u_s were parameters determined from appropriate high-pressure data. Relation 10 implied that

$$P = K_L u_3 + K_m(u - u_3) - (K_m - K_u)u_s \left[1 - \exp\left(\frac{u_3 - u}{u_s}\right) \right] \quad (11)$$

was the pressure density relationship for this region. The values for K_m and u_s were determined from Hugoniot data on Coconino sandstone at pressures above that required to close the air voids (figure 10). The values of $K_m = 680$ kbar and $u_s = 0.3$ provided the comparison shown in figure 10 for layer 2, with the less porous material having lower specific volumes for pressures below 150 kbar, consistent with internal energy relations. Although the model did not compare adequately with the data above 150 kbar, no pressure above 40 kbar ever occurred in the material during all calculations. The same value of K_m and $u_s = u_3 + 0.25$ were found suitable for all four layers.

The shear modulus, G , was also calculated in the equation of state model. In the low-pressure region the shear modulus was determined from

$$G = \frac{dp}{du} \left[\frac{3(1 - 2\nu)}{2(1 + \nu)} \right] \quad (12)$$

which allowed the Poisson's ratio to remain constant. In the high-pressure region, the shear modulus was a constant defined by

$$G = K_u \left[\frac{3(1 - 2\nu_L)}{2(1 + \nu_L)} \right] \quad (13)$$

where ν_L was the constant Poisson's ratio of the low-pressure region. This model is referred to as the hybrid ν - G model (Zelasko and Baladi, 1971; Bratton, 1973).

The second basic relation used to describe the materials is the material yield surface. A simple Mohr-Coulomb and von Mises yield surface (figure 11) that was independent of the third invariant of the deviator stresses was assumed for all materials. The yield surface, Y , was described by the relation

$$Y = \begin{cases} t_0 + P \tan \phi & P < P_{YLD} \\ Y_{MAX} & P \geq P_{YLD} \end{cases} \quad (14)$$

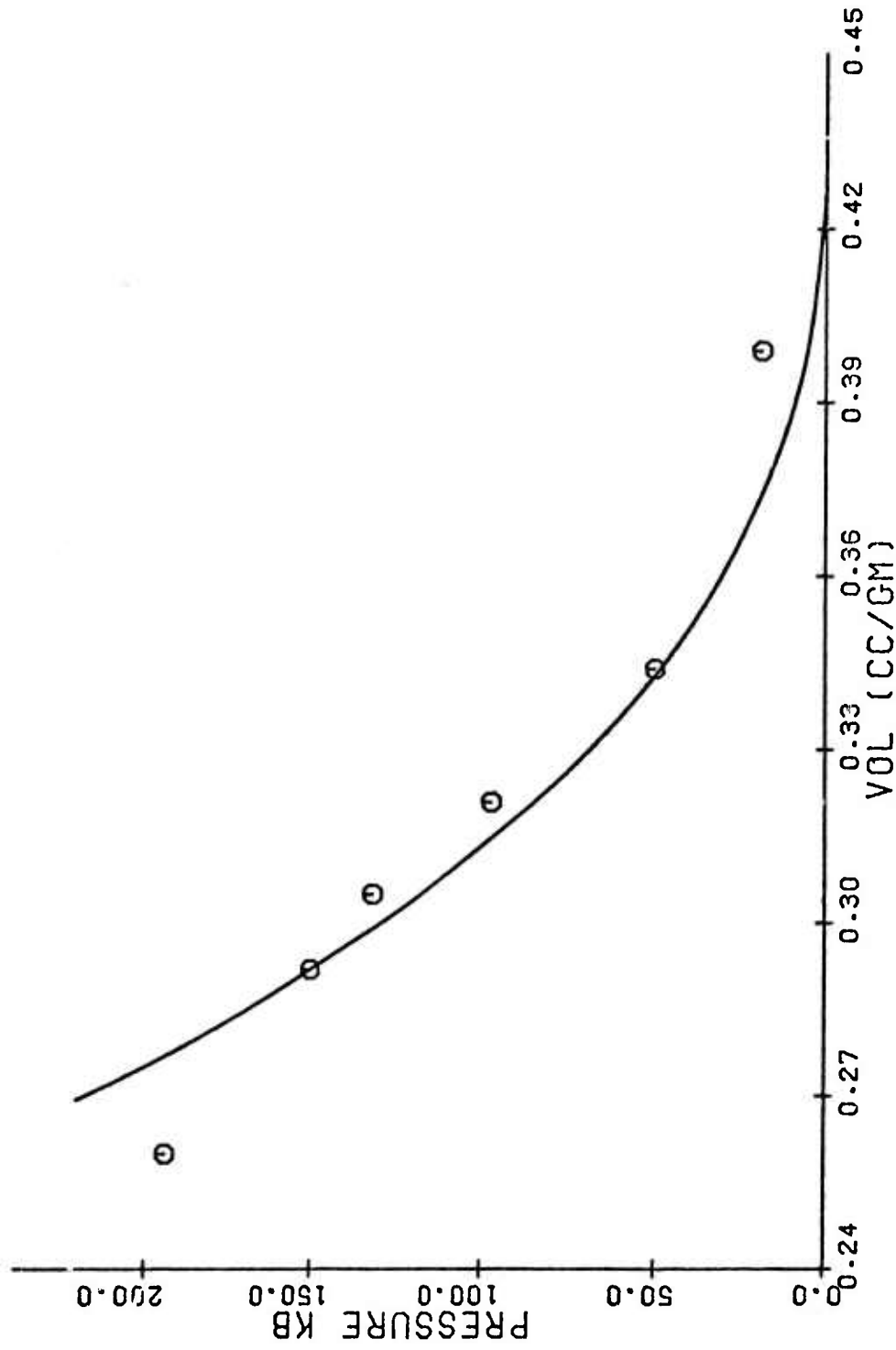


Figure 10. The Model Pressure--Specific Volume Relation in the High-Pressure Regime for Layer 2 (Data points are Hugoniot information for Coconino sandstone as presented by Jones, et al., 1968)

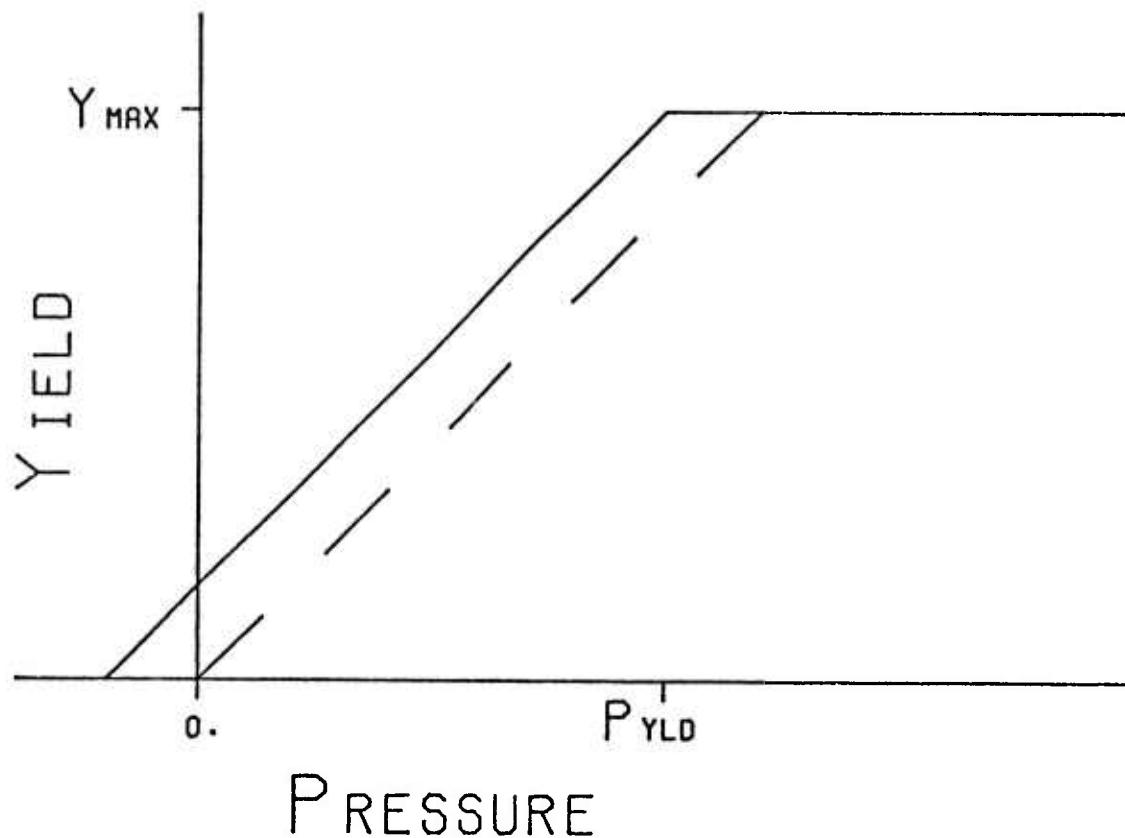


Figure 11. Schematic Yield Surface for Materials (Solid line indicates original yield condition as a function of pressure; dashed line indicates the shifted yield condition; no quantitative relation is expressed)

with t_0 the cohesion, ϕ the angle of internal friction Y_{MAX} the von Mises yield strength, and P_{YLD} defined by

$$t_0 + P_{YLD} \tan \phi = Y_{MAX}$$

Material separation was assumed to occur when the value of the yield surface for a calculation zone reached zero. At the locations of material separation, all forces except artificial viscosity terms and gravity were assumed to be removed. The results of initial simulation attempts indicated that, to achieve motions consistent with the formation of the observed crater, the yield description should be shifted to remove the cohesive strength of the material when

the yield condition was first reached in each thermodynamic zone.* This shift was accomplished by the use of a parameter, S , evaluated for each zone, which modified the expressions containing t_0 to

$$t_0(1 - S) \quad (15)$$

with S initially zero. The value of S was incremented by 0.04 when the yield condition was reached and during the subsequent twenty-four calculational cycles. The shift was accomplished in increments to avoid a drastic change in the yield surface description during one calculational cycle, which might result in calculational instability, and was always completed in less than 0.8 msec of simulated time.

Finally, a relation, called a flow rule, is required to describe the inelastic strain that occurs during flow with stress conditions limited by the yield surface. The associated flow rule (Niles, et al., 1971) was used in the calculations except as will be noted. This flow rule was derived with the Method of Plastic Potential (Trulio, et al., 1969) and results in a plastic volumetric increase, called "bulking," when the yield surface is a function of pressure. When the yield surface is independent of pressure, this flow rule reduces to the Prandtl-Reuss flow rule. Also, the Prandtl-Reuss flow rule was used if (1) the material was in tension, (2) the plastic volumetric strain had reached 0.1, or (3) the value of the yield surface was less than $0.5 t_0$. The first of the conditions was caused by uncertainties in the description of soil response to tension; the second condition limited the amount of bulking; and the third condition was caused by a singularity in the expression for the flow rule when the third invariant of the deviator stresses is ignored and the value of the yield surface is near zero.

The calculational grid spacing (appendix A) was selected based on the decision that this study was primarily interested in conditions in and below the crater region. Therefore, the calculation grid and target points were concentrated in that region. Outside that region the grid spacing was increased geometrically to minimize the calculation time. This decision resulted in only limited comparisons between calculation and experiment instrumentation data.

*As suggested by R. Port, Air Force Weapons Laboratory, personal communication, 1974.

c. Ballistic Extension Model

At the simulated time of 16.4 msec in the MIXED COMPANY II calculation, the material in and below the crater region was calculated to be separated and moving ballistically (as will be demonstrated). Because of this complete separation, the AFTON calculation was stopped at 16.4 msec and a simplified ballistic analysis was accomplished to estimate the final crater shape. This analysis was accomplished for the region within 35 feet range and a depth of 20 feet with the velocity conditions at 16.4 msec as initial conditions. Each grid point was allowed to move ballistically (appendix C) until the following three conditions were met:

- (1) The grid point either immediately below or radially away was not moving
- (2) The vertical velocity was negative
- (3) The density of the material in the bottom, outward quarter-volume of the zone was at least 1.5 gm/cc

The motion of a grid point was stopped after all these conditions, referred to as the stopping criteria, were once met.

3. MIXED COMPANY II NUMERICAL SIMULATION (MC 2.12)

The numerical simulation of the MIXED COMPANY II experiment, designated MC 2.12, resulted in calculated flow-field conditions at a simulated time of 8.4 msec (figures 12 and 13), which were consistent with the formation of a central mound. The material within a range of 12 feet and a depth of 20 feet had achieved upward velocities with the maximum vertical velocities near the vertical axis. Also, all the material within that region had separated and was in ballistic motion. A second velocity zone, centered near 18 feet range and 4 feet depth, was moving horizontally outward and again was completely separated. Only a flap of material in the top layer and beyond a range of 18 feet had significant velocities and had not separated. By 16.4 msec even this flap was completely separated, with little velocity change from the conditions that existed at 8.4 msec.

The model crater (figure 14) was formed by 16.4 msec and a fallback phase of the problem was beginning. The radius and slope of the model true crater wall, defined by the motionless material without extreme shear deformation, was consistent with the true crater profile. An extreme shear zone, with horizontal grid lines extending into an overturned flap, was calculated near the

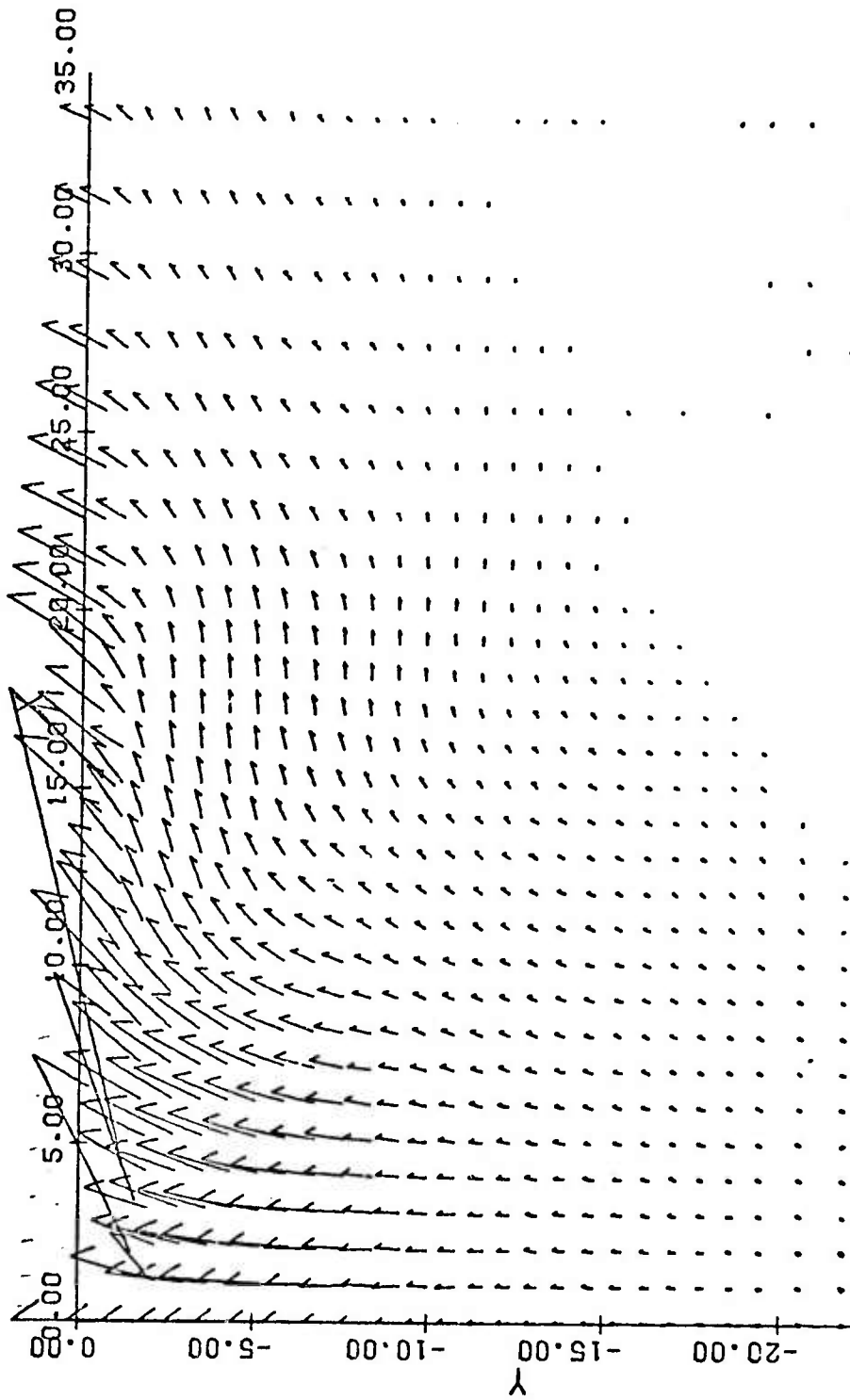


Figure 12. Velocity Vector Plot for MC 2.12 at 8.4 msec after Detonation (Velocity is proportional to the length of the vector with the distance between axis marks equal 100 ft/sec; axes are in feet)

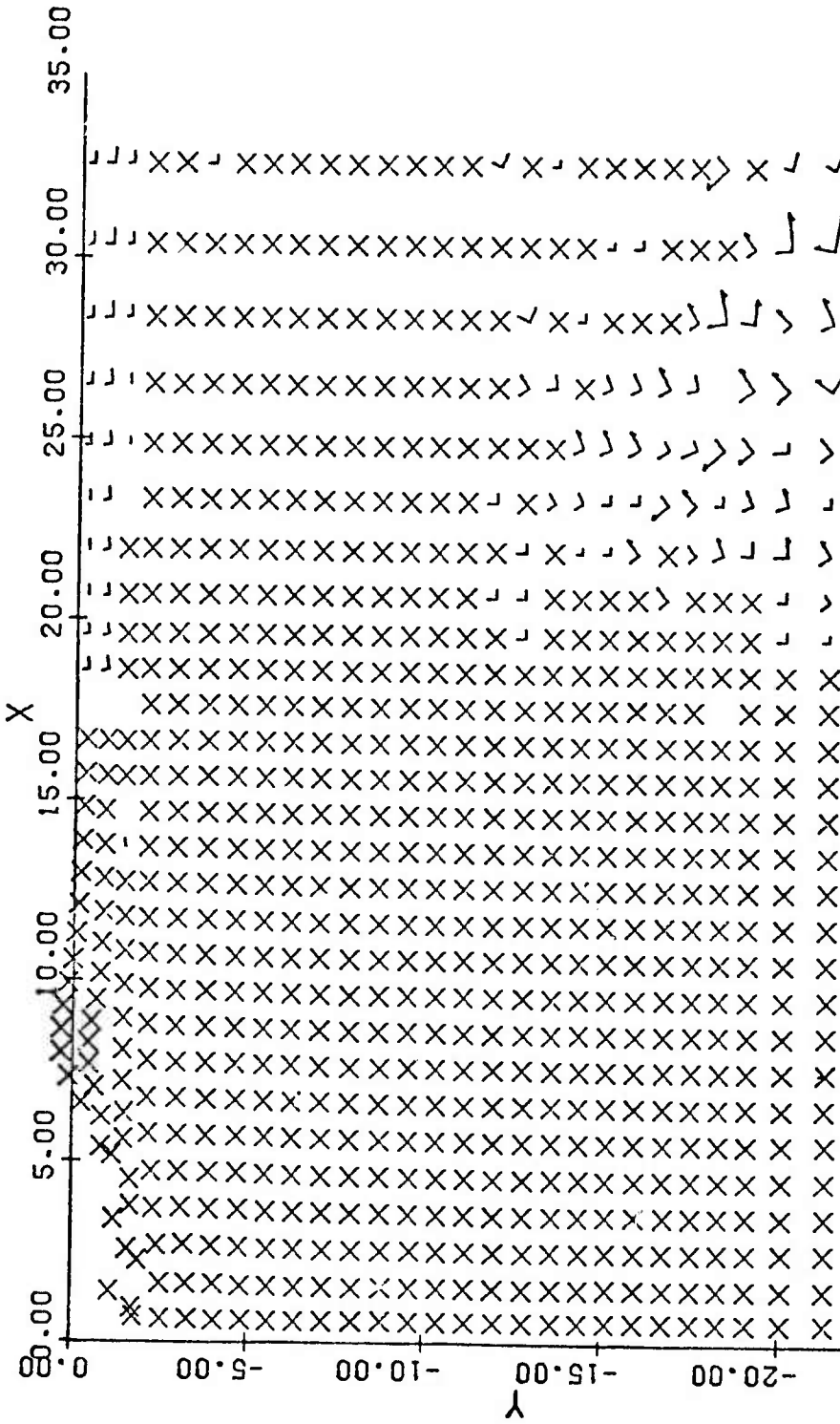


Figure 13. Principal Stress Axes Plot for MC 2.12 at 8.4 msec after Detonation (The marks, X, indicate material separation; stresses are proportional to the square of the vector length with the distance between axis marks equal 1 kbar; all stresses are compressive; figure axes are in feet)

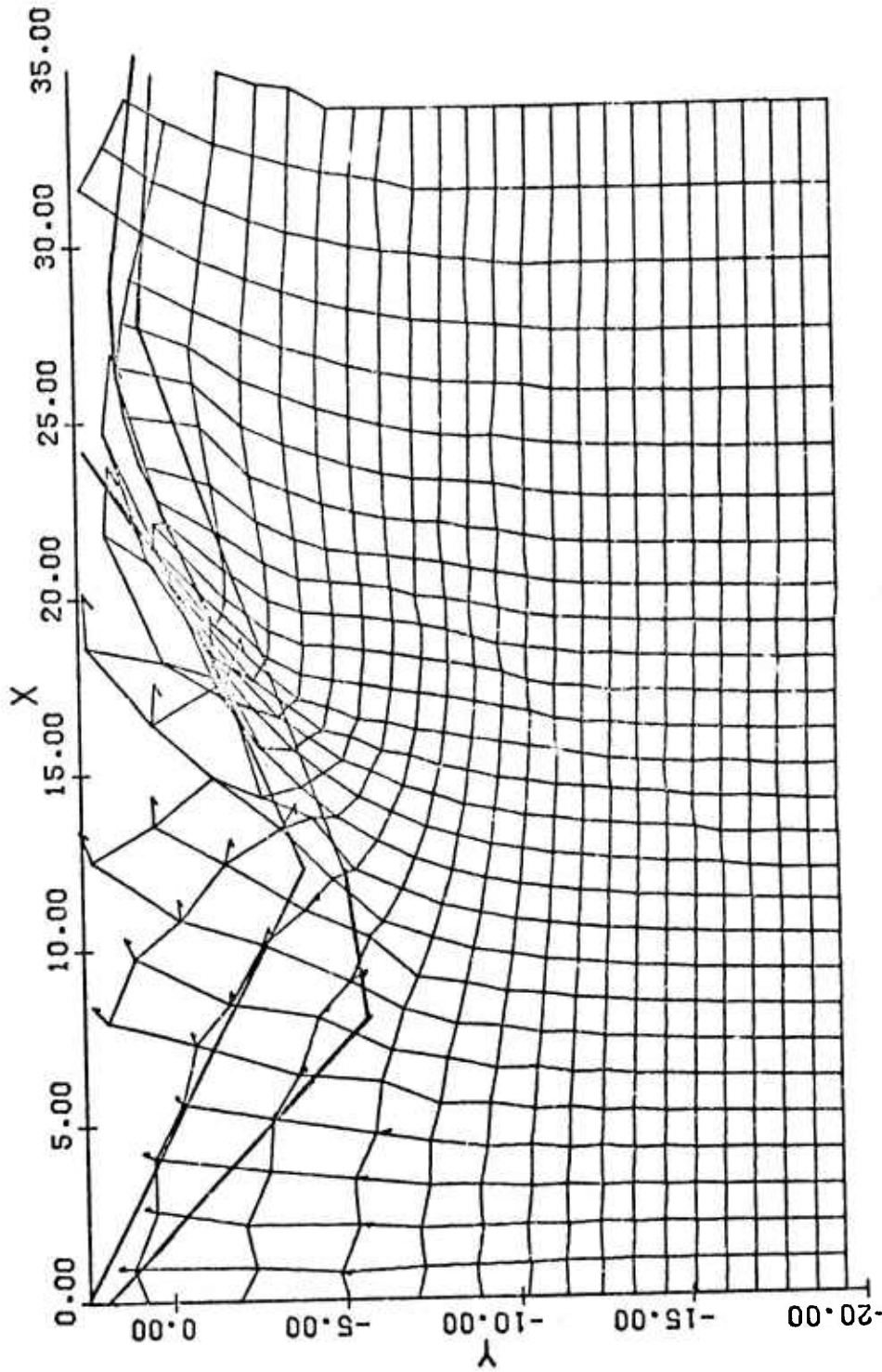


Figure 14. Calculation Grid Plot for MC 2.12 at 616.4 msec after Detonation Compared to Observed Apparent and True Crater Profiles along the Southern Radial of the MIXED COMPANY II Crater* (Velocity of a grid point is proportional to the length of the vector with the distance between axis marks equal 50 ft/sec; axes are in feet.)

*Carnes, B. L., Personal letter and data, Waterways Experiment Station, U.S. Army Corps. of Eng., Vicksburg, MS, 18 October 1973b.

range of the observed southern crater wall and within the asymmetry of the apparent crater. The material below the original surface and between the uplift region and the apparent crater wall was continuing to move ballistically toward the crater wall. Also, the bottom radius of the central uplift was comparable to the deepest point of the true crater, located at a range of 8 feet.

Several deficiencies of the calculational results were also apparent. First, the top calculational line shown in figure 14 at less than 30 feet range represented the interface that was initially at 1.8 feet depth, while the soil layer, even at 30 feet range, was above the 2.5 feet elevation allowed in the figure. However, the measurements of the near-surface motions in both MIDDLE GUST and MIXED COMPANY tests also showed initial upward spall velocities near the surface of at least 10 ft/sec caused by the direct-induced wave (Bratton, 1973; Port and Gajewski, 1973). These velocities were stopped by a second positive phase of air overpressure (Port and Gajewski, 1973) that would occur after the AFTON calculation was stopped and was ignored in the ballistic extension. The interaction of explosion products, aerodynamic forces, and particle-particle interactions rendered a ballistic treatment of ejecta distribution irrelevant. Also, the stopping of some grid points, such as the one located near the 18 foot range and the 0.0-foot depth, and the continued motion of other grid points through the crater wall showed that the stopping criteria were inadequate for model ejecta.

Another discrepancy, and of most concern to a discussion of central peaks, was that insufficient upward motions appeared to have been calculated to produce the height of the observed central mound. A continuation of the ballistic calculation resulted in the highest grid point on the symmetry axis in the figure eventually settling back to 2 feet below the original surface. As the next higher grid point was computed to eventually reach a height of 10 feet, the grid point in the figure probably represented the top of the calculated central mound for this model. An additional indication of the insufficient upward motion was the small upward displacement of the material at the 10-foot depth when compared to the 11 foot upward displacement of the colored grout that was placed at that depth. Possible causes for this discrepancy will be discussed after the results of parametric numerical experiments are described.

Even considering the displacement discrepancy, the results were in sufficient agreement with observations of the experimental event to warrant a

description of the conditions that produced the velocity field calculated at 8.4 msec. These conditions were shown by calculation-space plots (figures 15 and 16) at a time of 3.0 msec. The velocity-vector plot showed that a strong clockwise-rotational velocity wave had reached a depth of 14 feet near the vertical axis. Along the vertical axis, the motion changed from downward to upward at 12.6 feet depth, or immediately behind the intersection of the rotational motion with the vertical axis. Motion behind the wave was upward, with inward and outward oscillations occurring closer to the origin. The acceleration-vector plot showed clearly the wave structure in the flow field. The accelerations beyond a radius of 24 feet were directed radially outward, except in the near-surface airblast region, and indicated the location of the compressional wave. The acceleration reversal, at a radius of 24 feet from the origin, indicated the location of maximum compression. All material within that radius was recovering from maximum compressions and was, thus, described by the unloading models. The wave that produced the decrease in accelerations at the 20-foot radius was caused by a second increase in the overpressure model. The front of the rotational velocity wave at 16 feet radius was associated with accelerations which were parallel to the wave, indicating the wave was the principal shear wave. The velocity reversal on the vertical axis was, therefore, associated with the location of the principal shear wave. A series of calculated shear waves, produced by the "reflection" of the primary shear wave at the vertical axis, extended toward ground zero and controlled the sense of the horizontal velocities.

These wave relationships were also seen in the time histories (figures 17 and 18) of the target point located on the vertical axis, where the geometric relations result in the simplest analysis of vertical motions. For the target point on the vertical axis and at an initial depth of 10 feet, the maximum stress occurred at 1.4 msec. The compressive wave was then followed by a pressure decrease that was interrupted at 1.75 msec by a combination of the second compressive wave and the reflection of the first wave from the material interface at 11.4 feet depth. The principal shear wave arrived at 2.3 msec, producing (1) a change in the maximum stress direction from vertical to horizontal, (2) a momentary period of a completely elastic stress state, and (3) a reversal of velocity from downward to upward. Behind the principal shear wave, the vertical stress was small while horizontal stresses were more gradually reduced until the material separated at 5.5 msec. At the time of separation, the

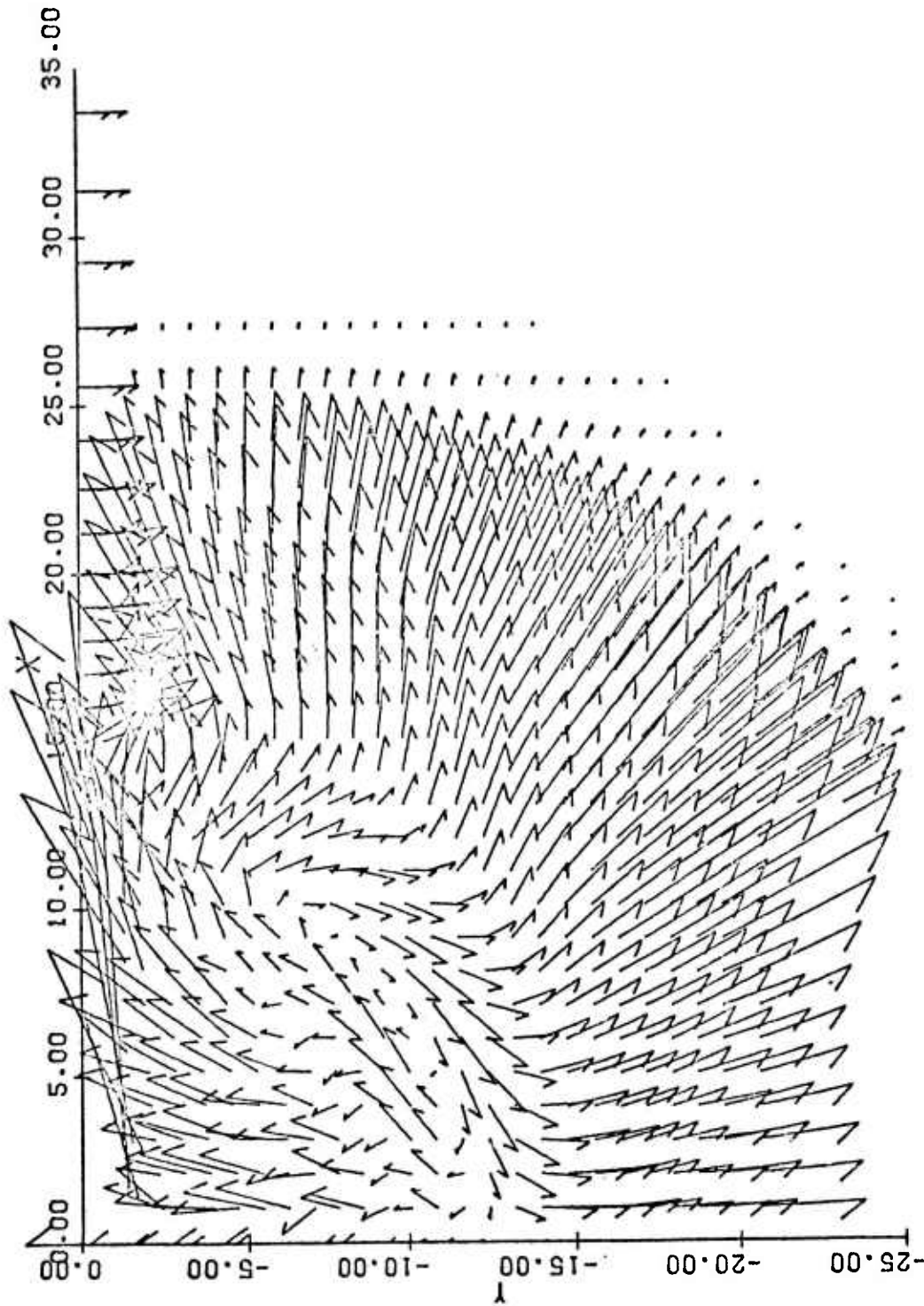


Figure 15. Velocity Vector Plot for MC 2.12 at 3.0 msec after Detonation (Velocity is proportional to the vector length with the distance between axis marks equal 100 ft/sec; axes are in feet)

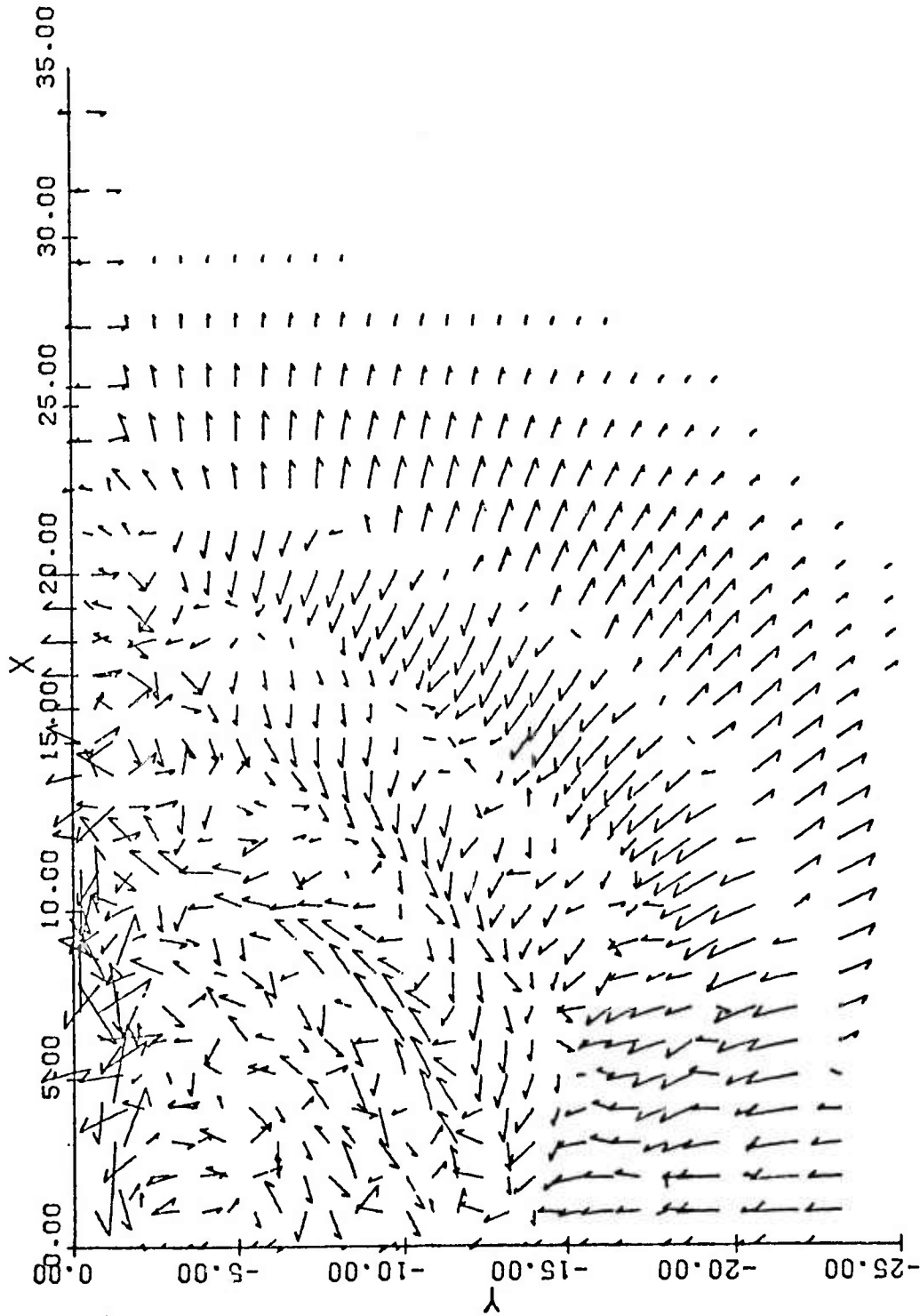


Figure 16. Acceleration Vector Plot for MC 2.12 at 3.0 msec after Detonation
(Acceleration is proportional to the square of the vector length
with the distance between axis marks equal 100 kg; axes are in feet)

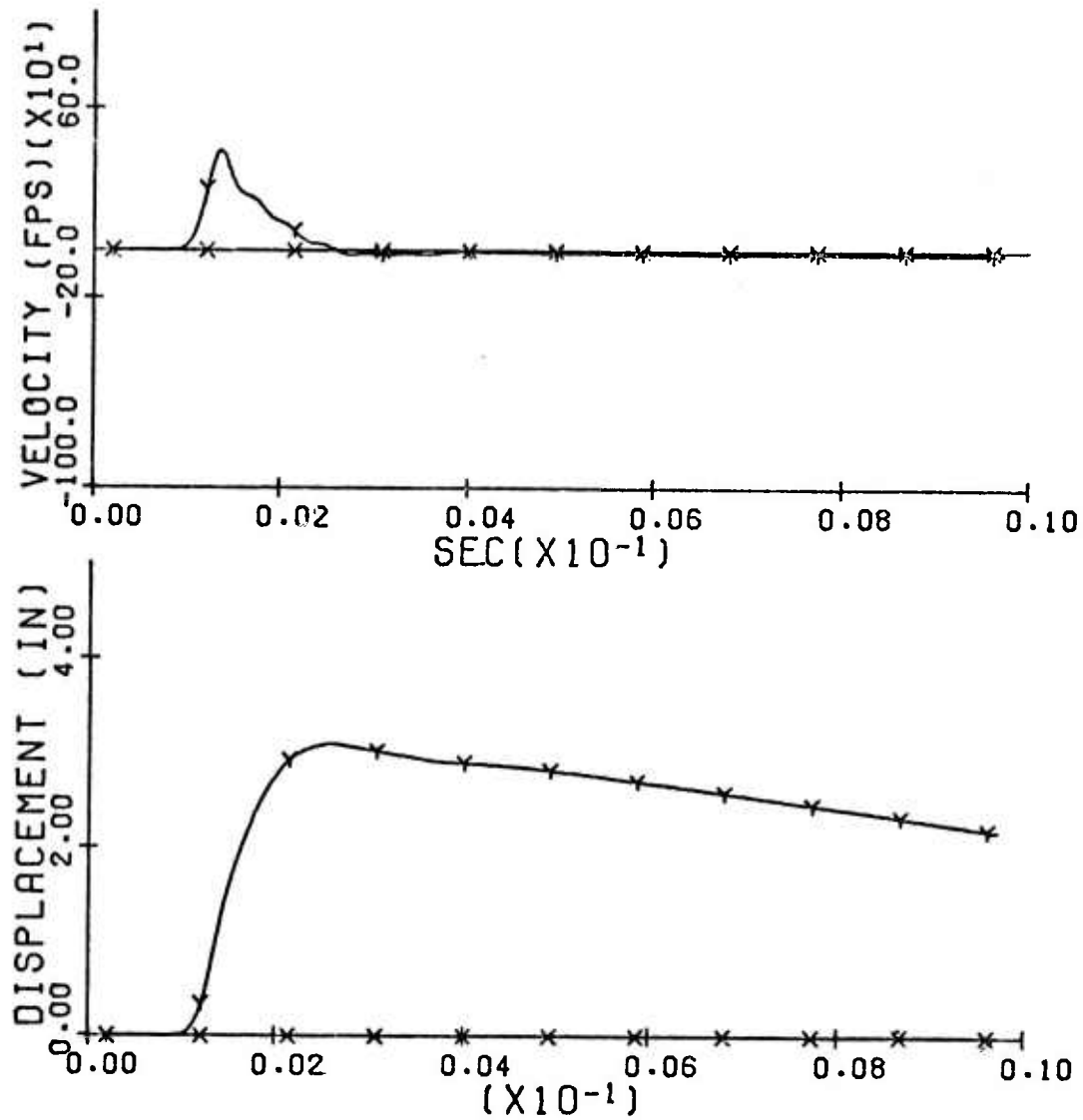
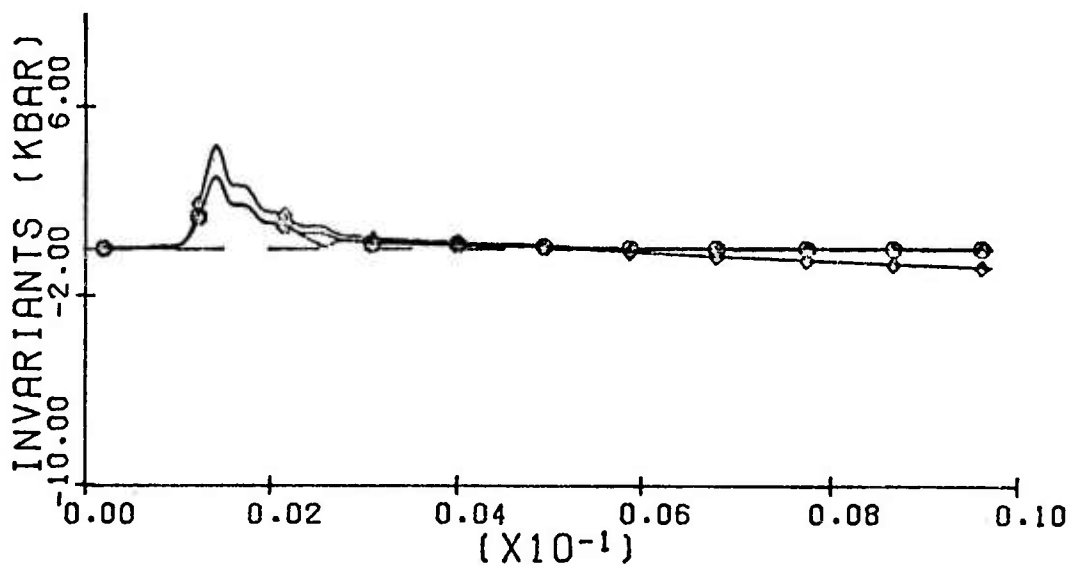
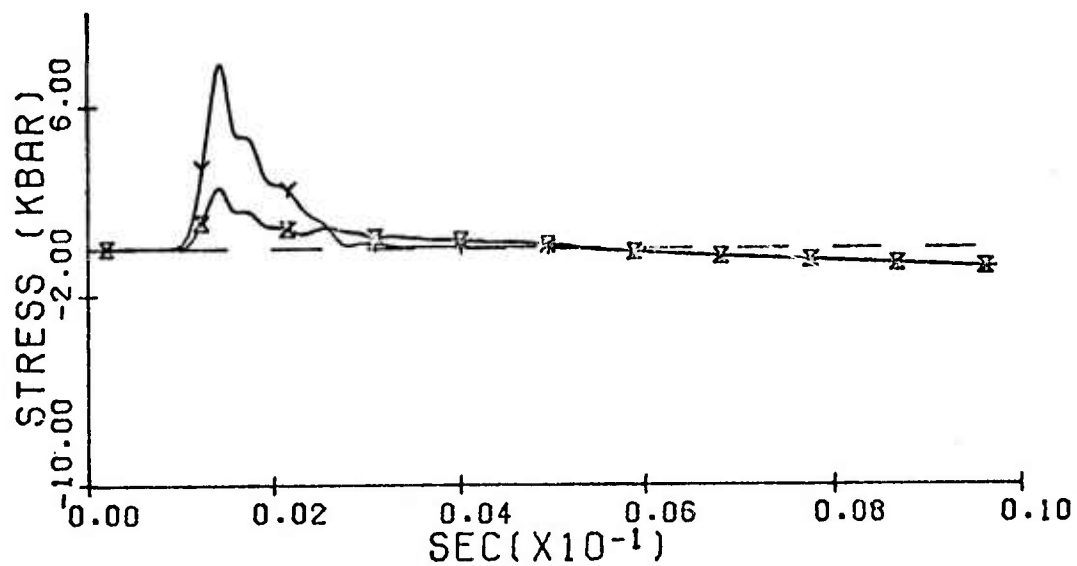


Figure 17. Motion Time History for the Target Point Originally Located on the Vertical Axis at 10 Ft Depth in the MC 2.12 Calculation (Positive Y values indicate downward motion)



- | | |
|----------------|----------------------|
| Y - vertical | ◇ - pressure |
| X - radial | △ - yield condition |
| Z - tangential | ○ - second invariant |

Figure 18. Stress Time History for the Target Point of Figure 17 with Compressive Stresses Positive (Negative stresses indicate material separation)

target point had an upward velocity of 12 ft/sec, which would result in a maximum ballistic displacement of 2.2 feet.

The horizontal motions were examined in the time histories (figures 19 and 20) of the target point initially located at a depth of 8 feet and a distance of 4 feet from the vertical axis. This point was first driven radially away from the origin by the compressional wave. The principal shear wave, which arrived near 2.2 msec, produced the inward velocity with a small enhancement of the downward velocity. The symmetry condition "reflected" the shear wave at the vertical axis, which resulted in a second shear arrival near 2.7 msec that produced upward and outward motion. Subsequent shear waves continued until the material separated, at 4.5 msec, after which the target point continued ballistically.

As noted before, a second region of primarily horizontal motion occurred in the calculation, centered near 18 feet range and 4 feet depth. Time histories in this region (figures 21 and 22) showed an active period of 4 msec after which a condition of constant velocity was achieved. The constant-velocity condition was associated with no material density decrease, as shown by the stresses remaining near zero in contrast to the large negative stresses shown in the time histories below ground zero. Thus, the materials were moving radially outward, and into a larger volume, in a velocity-range relation that resulted in a constant density. This region eventually formed the model true crater wall.

Two additional results of this simulation were of interest for shock-wave cratering studies. First was a contour map (figure 23) of peak pressures as a function of original position. This contour map indicated, by the absence of the 40-kbar contour, that the maximum pressure experienced anywhere in the calculational medium was less than 40 kbar. The transmission of high pressures in the medium below the 1.8 foot soil layer, and the absence of high pressures in the soil layer, indicated that only direct-induced signals were important in the lower medium. The increase of acoustic impedance in the layer between 11.4 and 19.2 feet depth also resulted in modification of the relation between maximum pressure and range. Second, the motion of the target point initially located at a range of 6 feet and a depth of 1 foot (figure 24) simulated the path of material ejected to a long range. The particle path was similar to the motion of particles suggested by Gault, et al., (1968) during the excavation stage of a crater formed by hypervelocity impact.

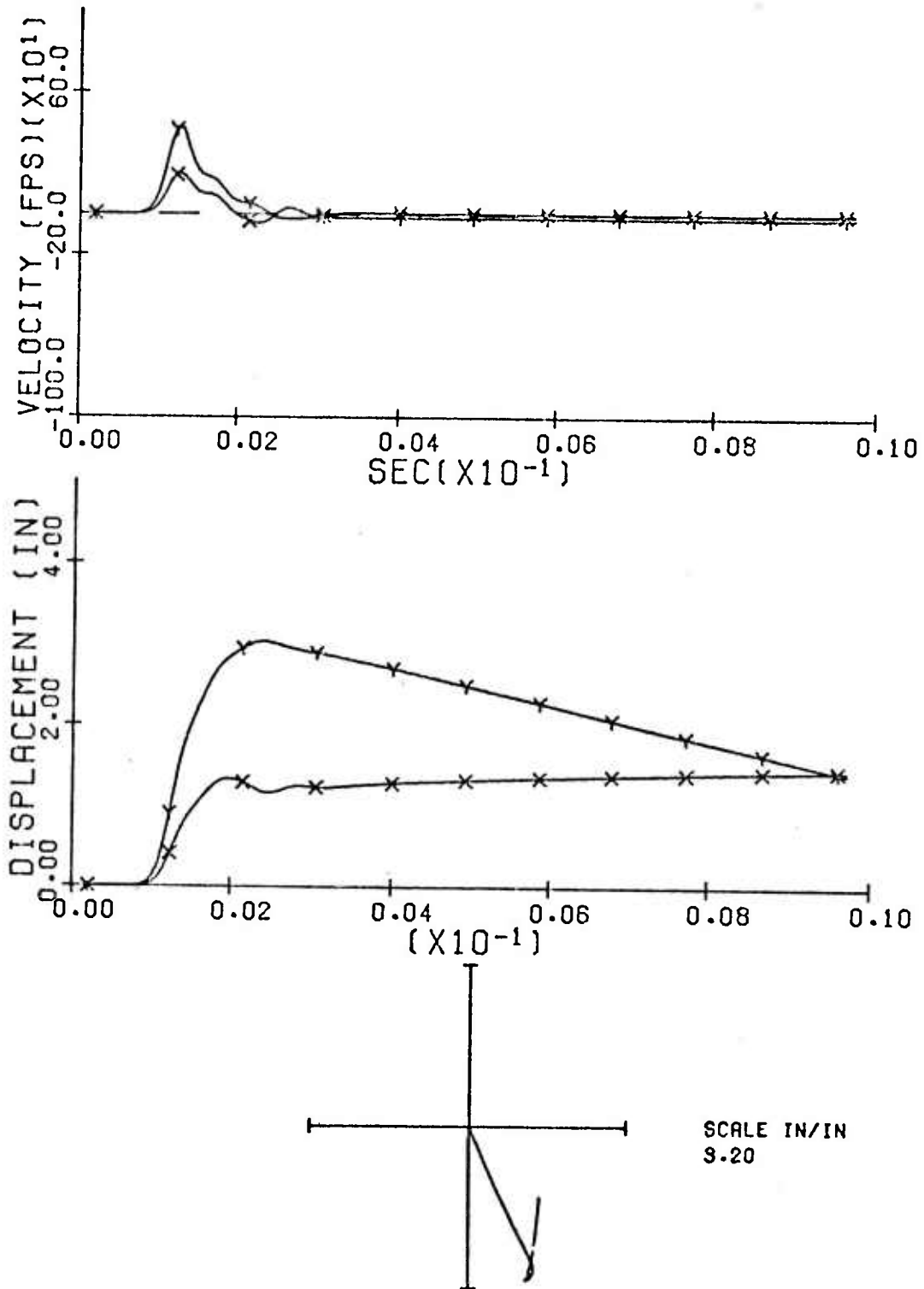
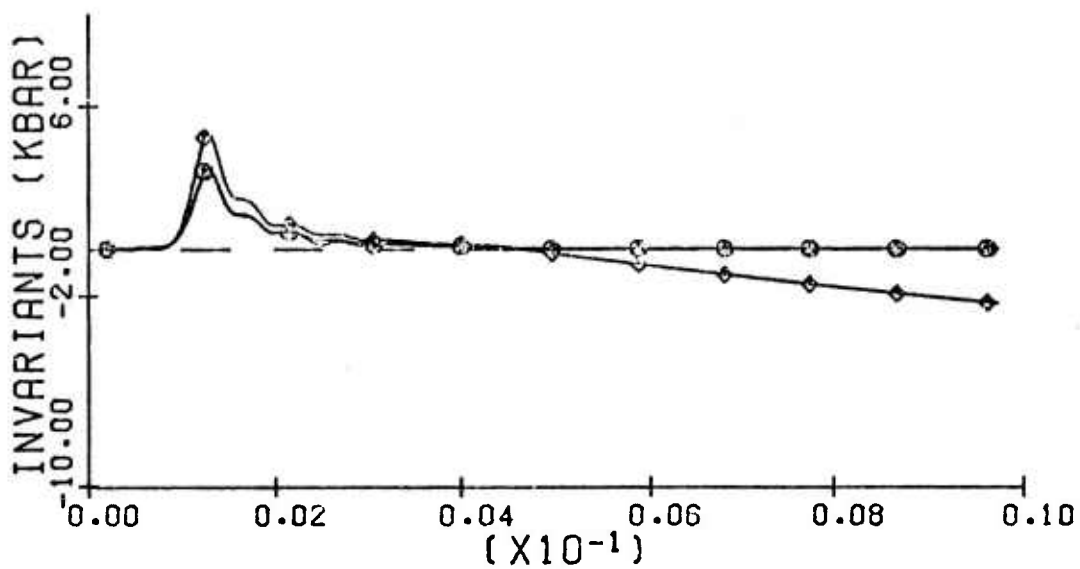
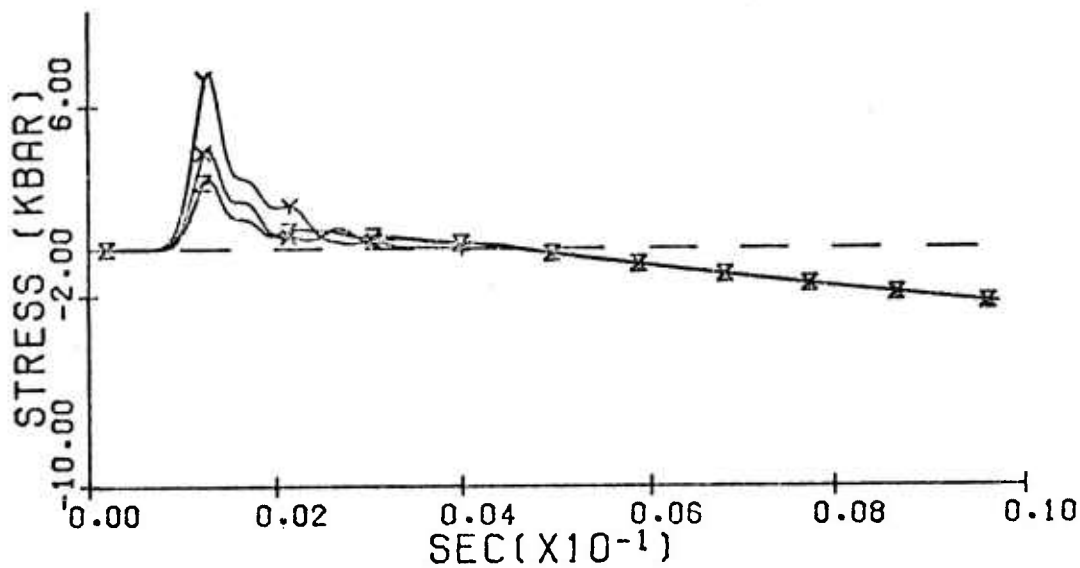


Figure 19. Motion Time History of the Target Point Originally Located at 4 Ft Range and 8 Ft Depth in the MC 2.12 Calculation (Positive Y values indicate downward motion; positive X values indicate outward motion; target point path shown with downward motion down and outward motion to the right)



- Y - vertical
- X - radial
- Z - tangential
- ◇ - pressure
- △ - yield condition
- - second invariant

Figure 20. Stress Time History for the Target Point of Figure 19 with Compressive Stresses Positive (Negative stresses indicate material separation)

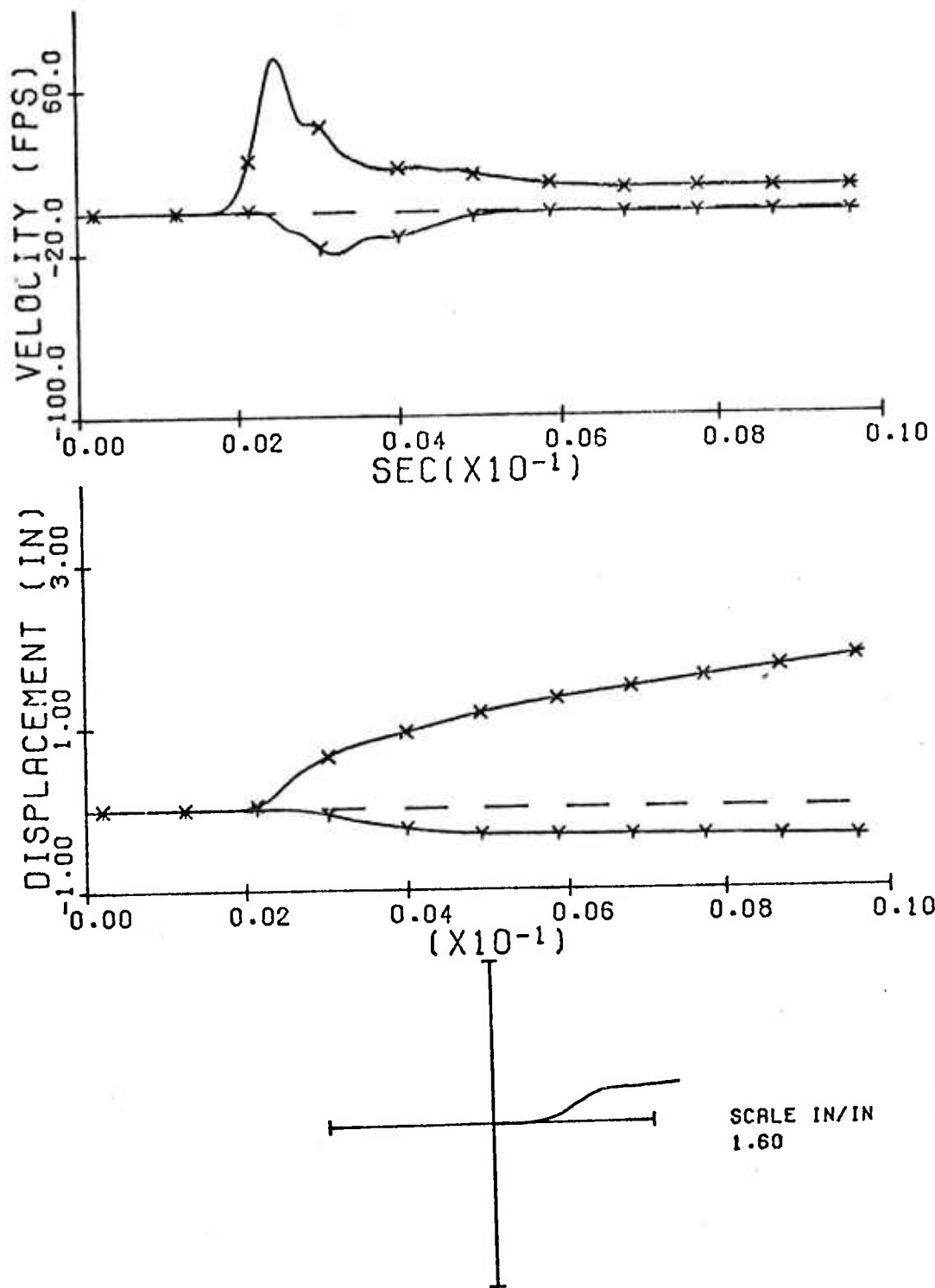
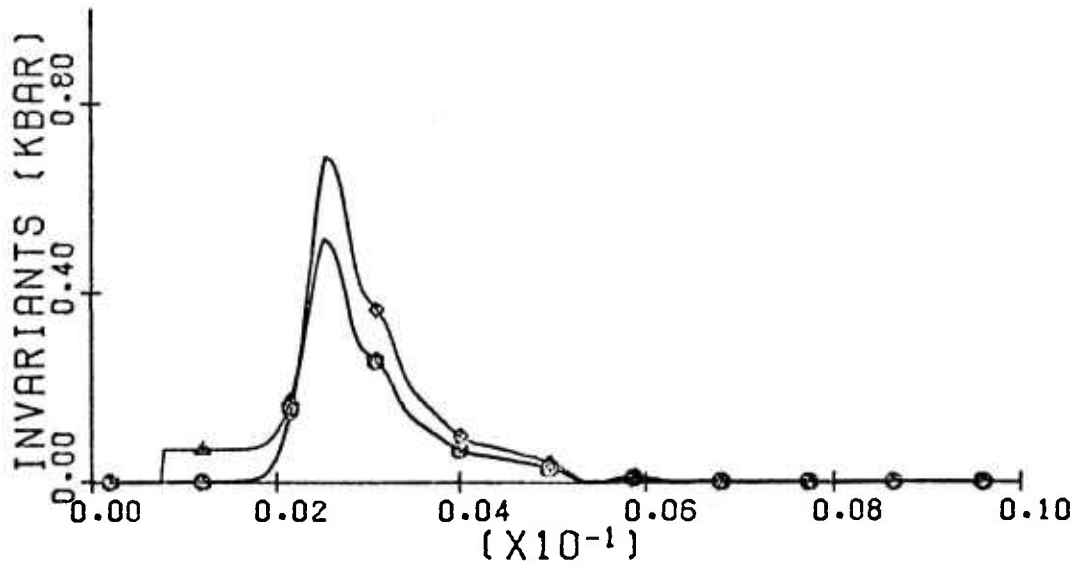
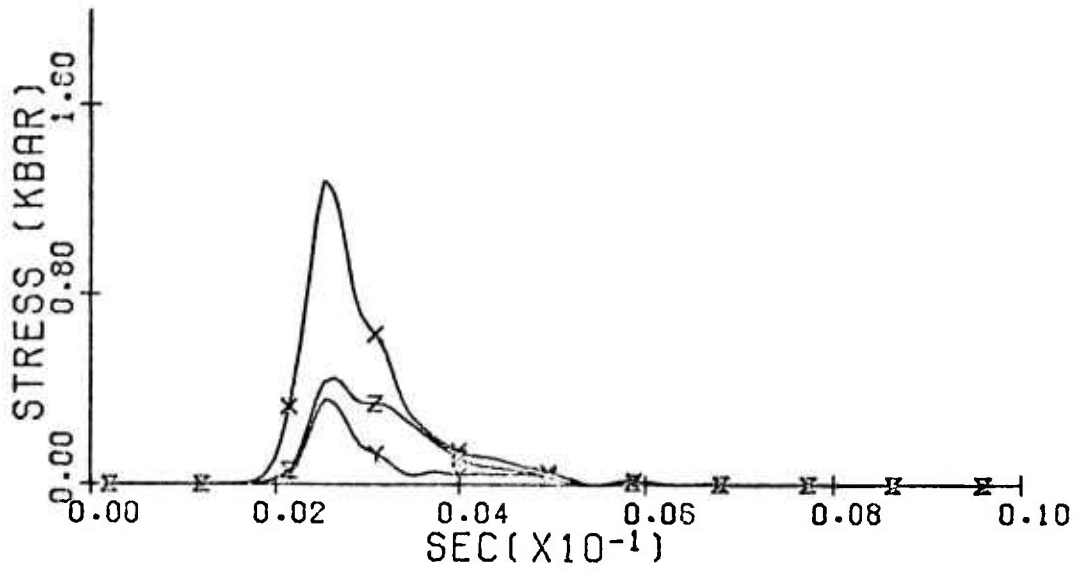


Figure 21. Motion Time History of the Target Point Originally Located at 18 Feet Range and 4 Ft Depth in the MC 2.12 Calculation (Positive Y values indicate downward motion; positive X values indicate outward motion; target point path shown with downward motion down and outward motion to the right)



- Y - vertical
- X - radial
- Z - tangential
- ◇ - pressure
- △ - yield condition
- - second invariant

Figure 22. Stress Time History for the Target Point of Figure 21 with Compressive Stresses Positive

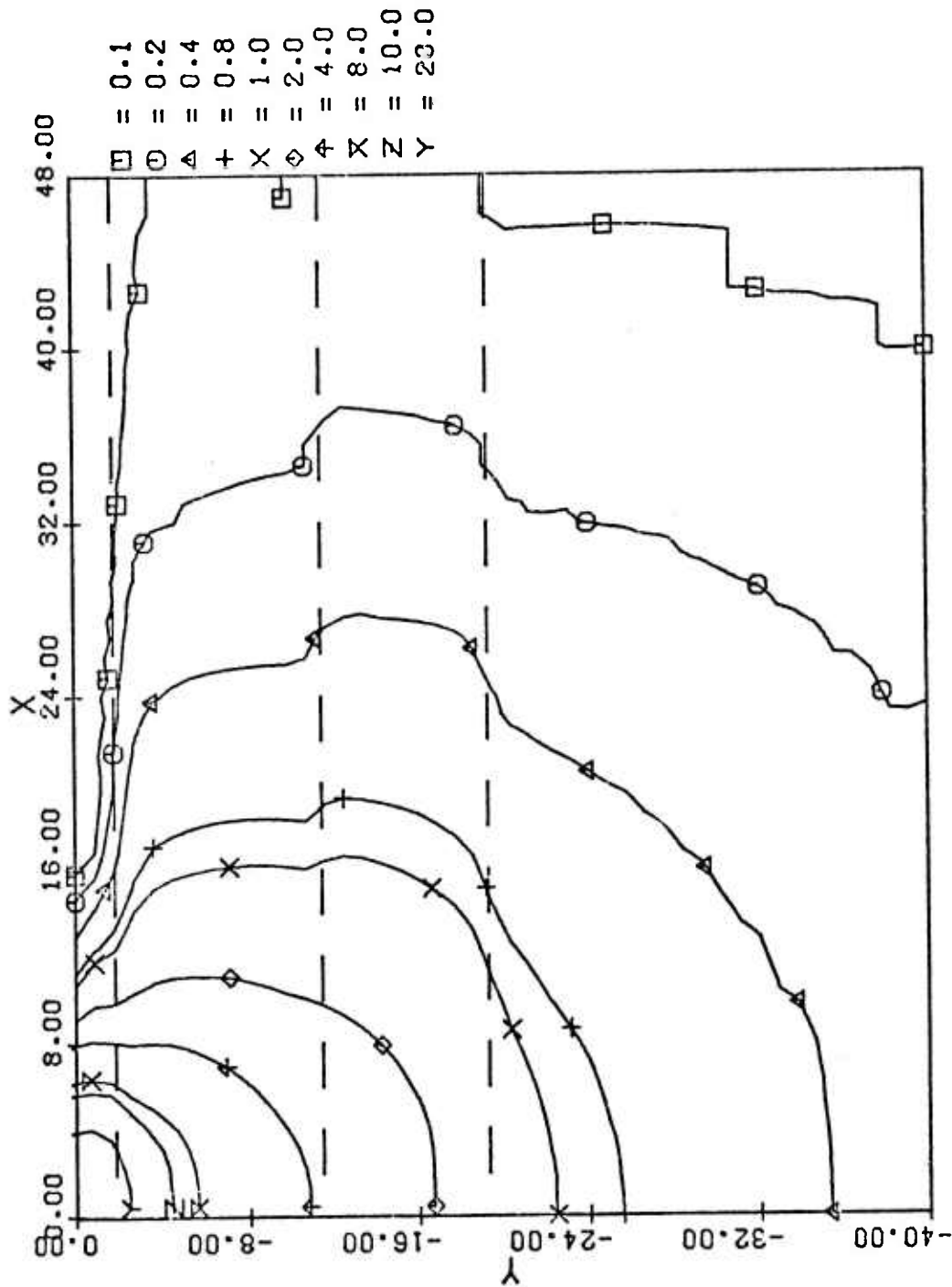


Figure 23. Maximum Pressure Contours as a Function of Original Position for the MC 2.12 Calculation (Dashed lines indicate layer interfaces; peak pressures are in kbars; axes are in feet)

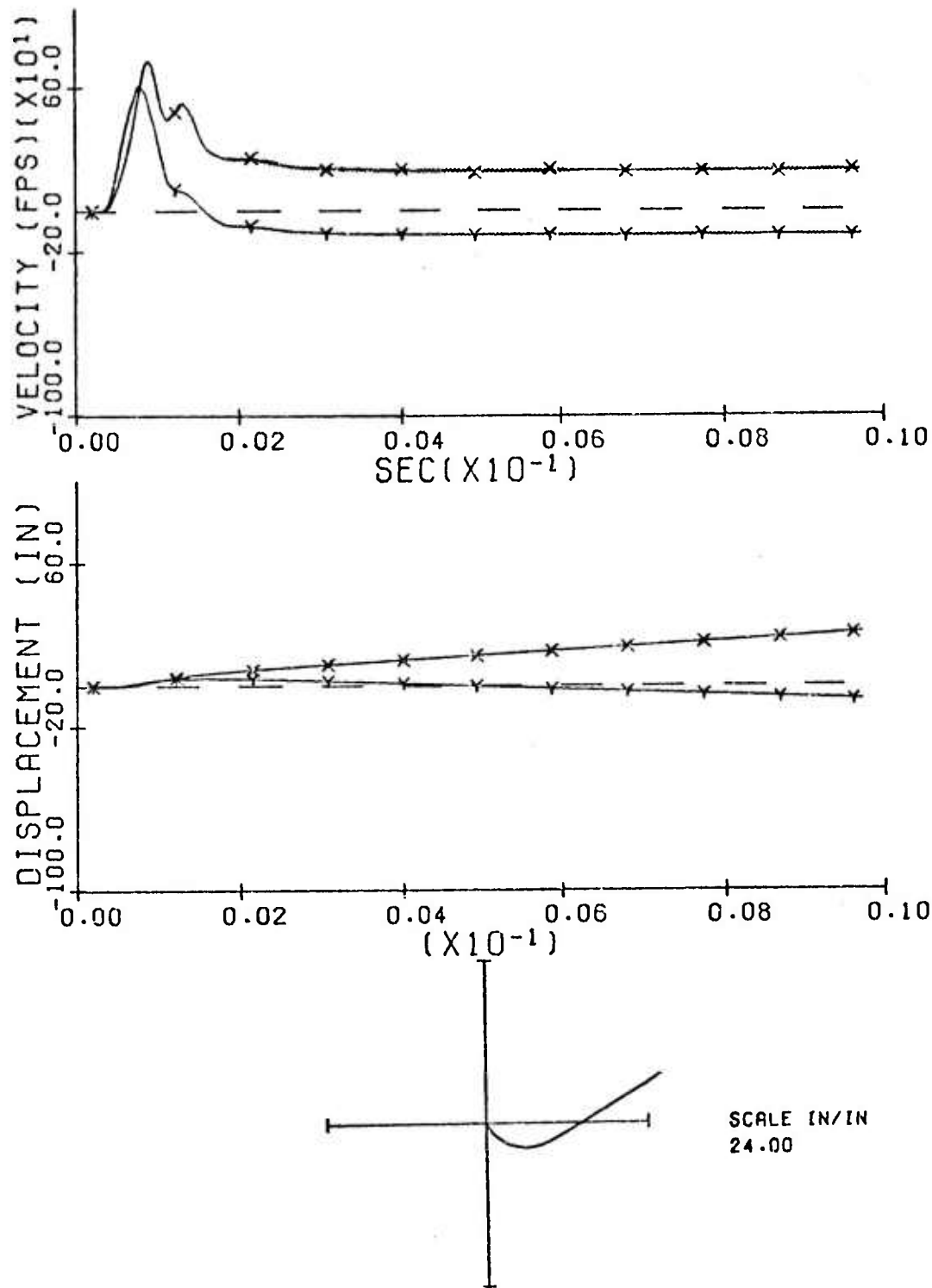


Figure 24. Motion Time History of the Target Point Originally Located at 6 Feet Range and 1 Foot Depth in the MC 2.12 Calculation (Positive Y values indicate downward motion; positive X values indicate outward motion; target point path shown with downward motion down and outward motion to the right)

4. NUMERICAL PARAMETRIC STUDY

The results of the MIXED COMPANY II numerical simulation, MC 2.12, were applicable only to that experiment. Extension of those results to other occurrences of central mounds required information concerning the effects of material properties on central mound mechanics. This information was obtained through a parametric study of the influences of compactibility, layering, and material yielding models. In addition, as a first attempt to apply the study of central mounds to an examination of lunar evolution, the influence of a "fluid" material below a solid layer was examined. The results of the calculations in this parametric study indicated that (1) the calculation of upward motions below the crater was dependent on the material compaction model, (2) the layering included in the MIXED COMPANY II simulation only slightly influenced the upward velocities below the crater, (3) the bulking model included in the associated flow rule contributed significantly to the calculated upward motions, (4) upward velocities for grid points on the axis of symmetry were first calculated where strength effects were important, and (5) the presence of a lower, "fluid" layer modified the calculated response in an overlying, solid layer in a manner that may have eventually resulted in upward motions.

a. Compaction Model Effects

The results of the DISTANT PLAIN 6 and Nuclear Explosion numerical simulations had indicated that increased compaction of materials reduced the calculated upward velocities. The effects of changes in the compaction model on the MC 2.12 results were examined in two numerical experiments. In the first experiment, the values of the initial unloading sonic velocities, c_u , in the lower three layers were changed to $c_u = c_L + 3000$ which increased the compactibility of the materials to 30 percent. In the second experiment, no compaction of the material in the lower three layers was allowed.

Calculation MC 2.13, which included the increased compactibility, resulted in a complete lack of upward motions below the crater. By 9.5 msec, all vertical velocity components, (figure 25), below the crater region were either downward or had completely stopped. Further, there were no compressive stresses in the material below the crater to a depth of 35 feet to produce significant upward velocities after this time. A ballistic extrapolation of this velocity field would be expected to produce a crater of about 22 feet radius and a maximum depth below the original ground surface of 3 feet directly below ground zero with no central mound. These results occurred even though

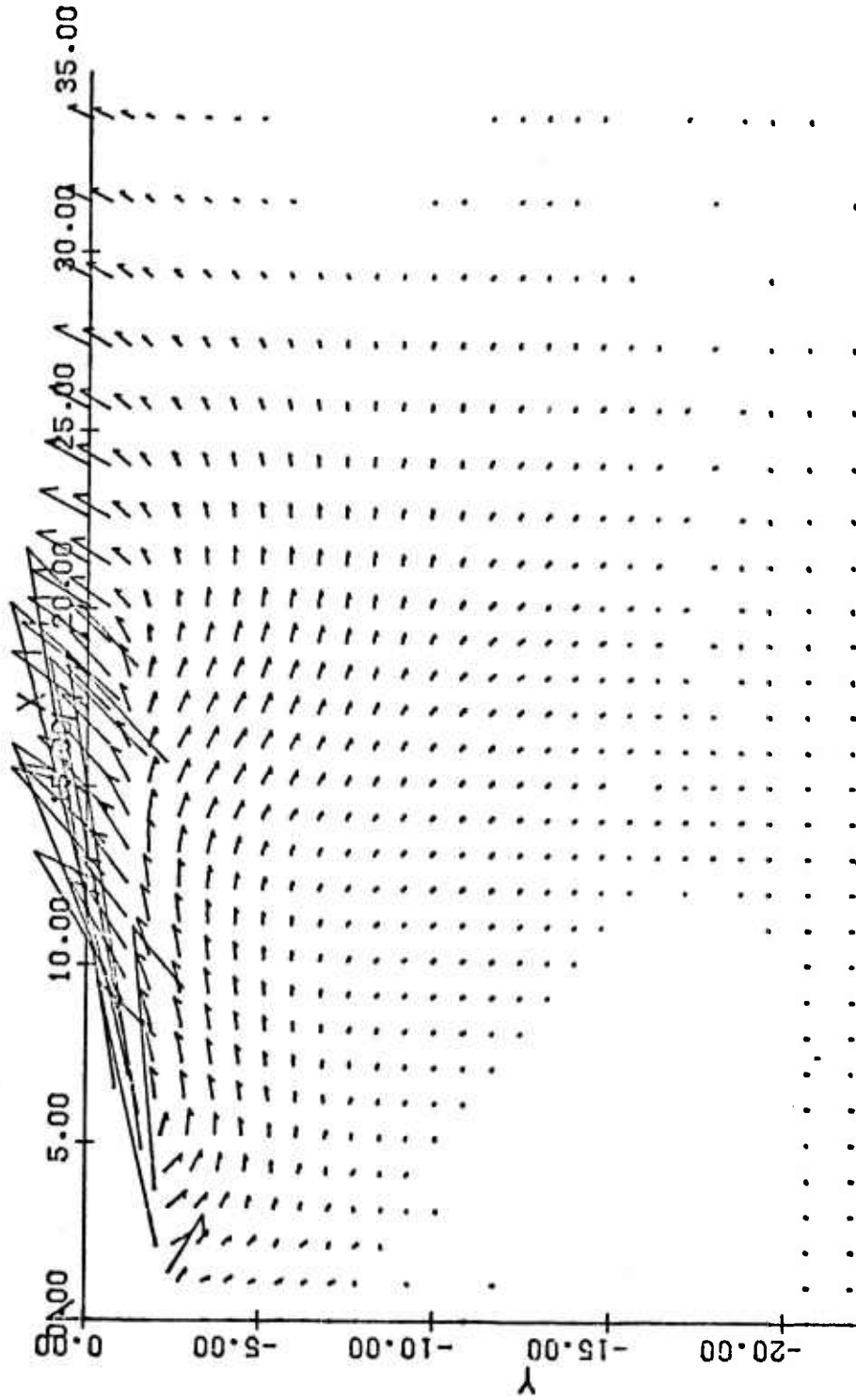


Figure 25. Velocity Vector Plot for MC 2.13 at 9.5 msec after Detonation (Velocity is proportional to the vector length with the distance between axis marks equal 100 ft/sec; axes are in feet)

the calculated primary shear wave produced inward velocities, but not a change in maximum stress direction, as it propagated down the vertical axis.

The results of the calculation with incompactible lower layers, MCP-03, indicated motions qualitatively similar (figure 26) to the MC 2.12 calculation, but with larger velocity magnitudes below the crater. The upward velocity after material separation for the target point on the vertical axis and initially 3 feet below the surface was 83 ft/sec, which was a factor of 2 greater than the velocity for the similar target point in the MC 2.12 calculation. However, because the magnitude of the upward velocity decreased more rapidly with depth in the MCP-03 results, the velocity of the target point at the 10-foot depth was only 16.3 ft/sec, or a factor of 1.35 greater than the equivalent value in the MC 2.12 calculation. That velocity would produce a ballistic displacement of only 4.1 feet upward. Also, because velocity conditions in the entire flow field were increased, the model crater produced by a ballistic extension of this calculation would be expected to be less consistent with the observed crater than the MC 2.12 crater model. Therefore, a simple reduction in the model compactibility would not provide an explanation of the discrepancy between the heights of the observed and calculated central mound.

A third numerical experiment, MCP-09, was accomplished because of the contrast in the results between the MC 2.12 calculation, with 10 percent compactibility, and the MC 2.13 calculation. The calculation MCP-09 was used to determine whether the upward velocities below the crater were dependent on the material compactibility or the entire unloading relation. In the MCP-09 calculation, the same values of c_u as MC 2.13 were used, but the compaction values were reduced to the MC 2.12 values.

The results of calculation MCP-09 indicated that the value of the final density after a cycle of loading and unloading was more important to central peak formation than an accurate description of the unloading path. The calculated flow field at 9.5 msec (figure 27) was similar to the MC 2.12 calculation, with only small differences existing. The differences included a maximum 20 percent difference in the calculated vertical velocities along the axis of symmetry. In the MCP-09 calculation, the final velocities were all lower than the MC 2.12 results above 9 feet depth and higher below that depth, which would increase the height of the calculated central mound. Also, the horizontal velocities were generally lower and tended to be more inward in the MCP-09 calculation.

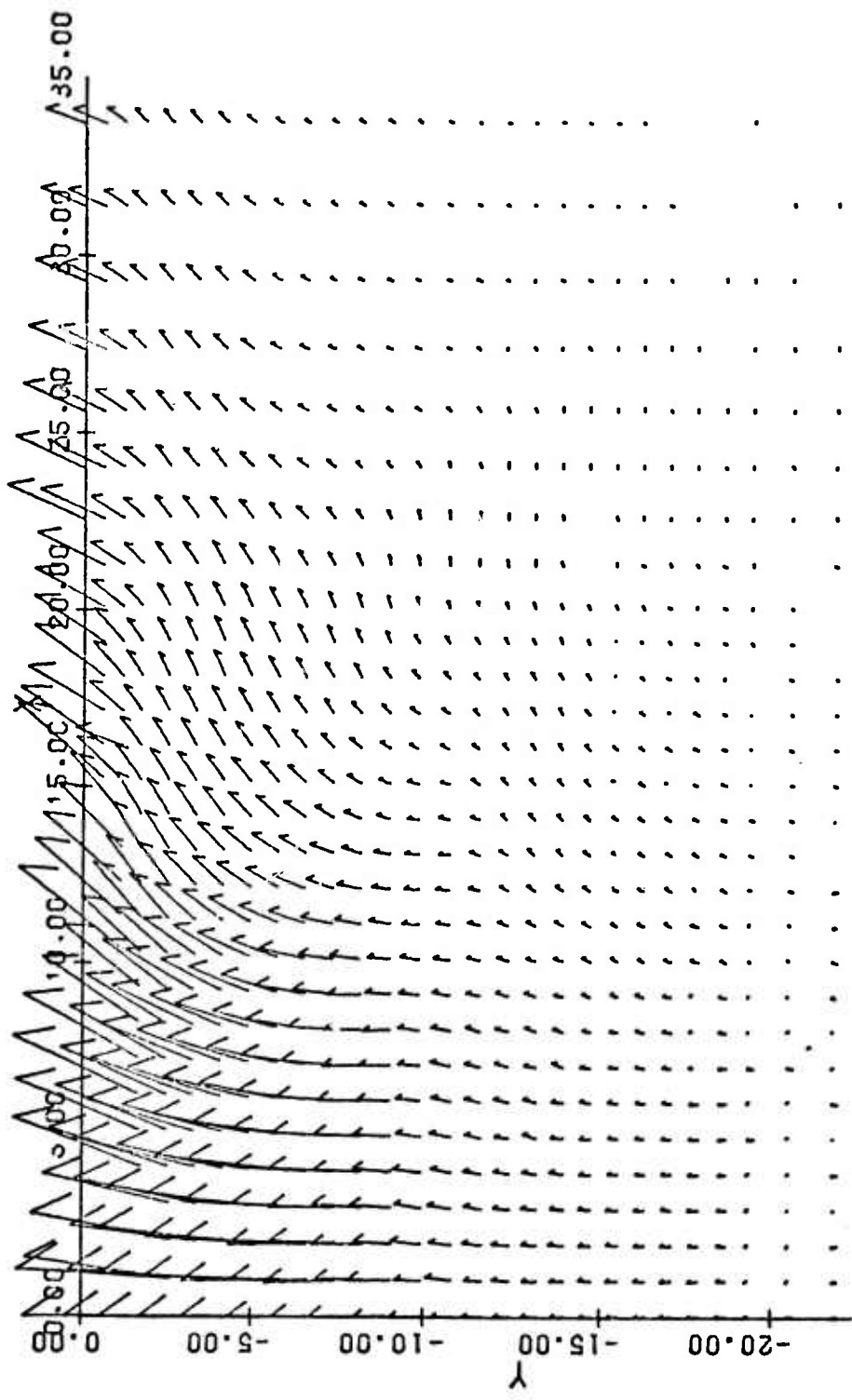


Figure 26. Velocity Vector Plot for MCP-03 at 8.2 msec after Detonation (Velocity is proportional to the vector length with the distance between axes marks equal 100 ft/sec; axes are in feet)

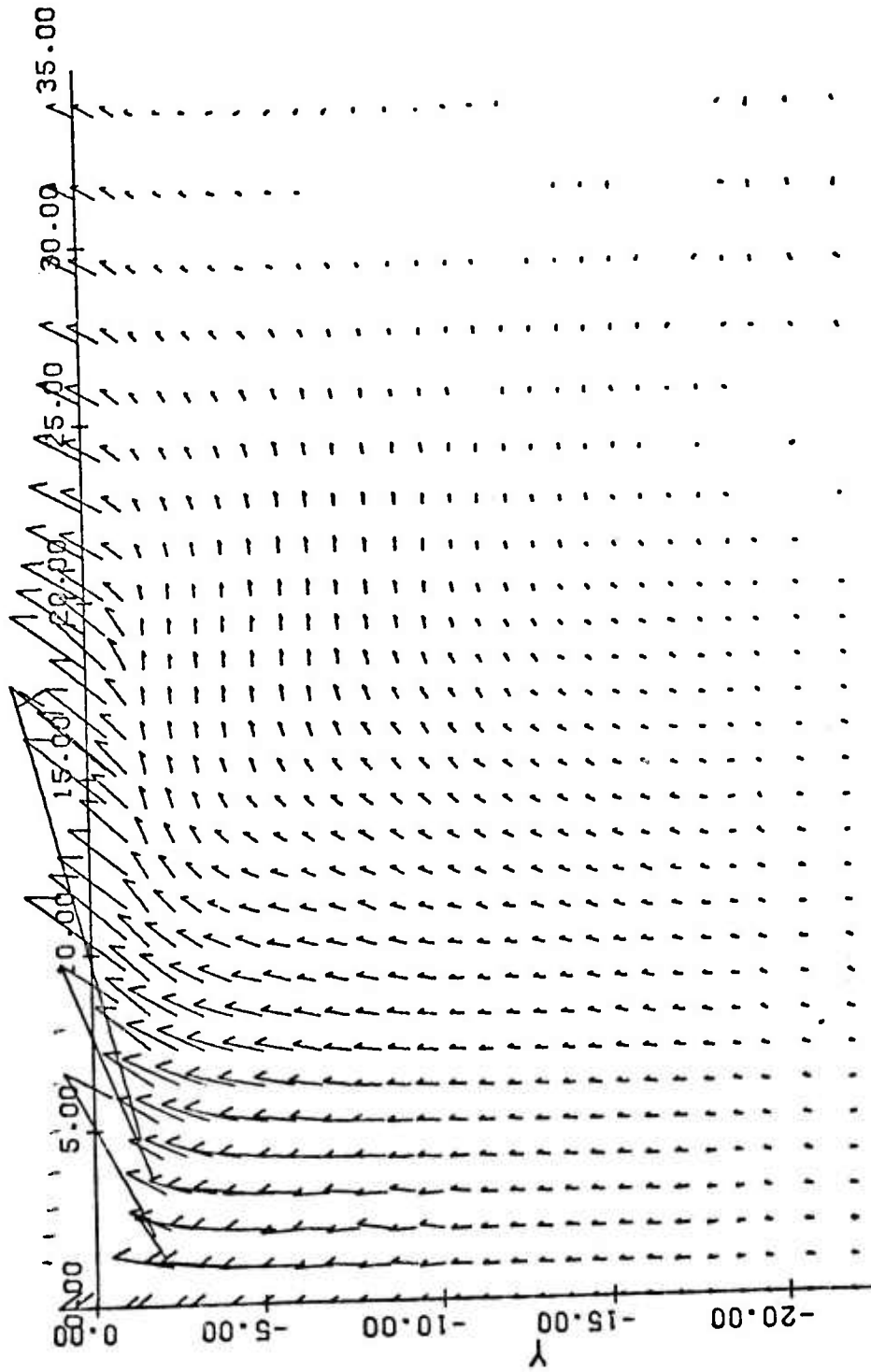


Figure 27. Velocity Vector Plot for MCP-09 at 9.5 msec after Detonation (Velocity is proportional to the vector length with the distance between axis marks equal 100 ft/sec; axes are in feet)

The similarity existed between the MC 2.12 and MCP-09 calculations despite a completely different early history of the two models. The flow field at 2.8 msec for MCP-09 (figure 28) was much different from the MC 2.12 flow field (figure 15) at 3.0 msec. The primary shear wave produced lower inward velocities close to the axis as it passed. The maximum inward velocity in the MCP-09 calculation was 13 ft/sec at 11.6 ft depth; while in the MC 2.12 calculation, it was 28 ft/sec at 12.3 ft depth. Also, upward velocities along the vertical axis did not occur below 9 feet depth, which was significantly shallower than the primary shear wave or even its calculated reflection. Finally, in contrast to the MC 2.12 calculation, the maximum stress remained the vertical stress after the shear wave passed. All of these differences were caused by the different wave speeds of the two models.

b. Layering Effects

Three numerical calculations were used to determine the influence of the material layers that were modeled in the MIXED COMPANY II simulation. Incompactible models for the lower three layers were used to simplify the analysis of the results and to emphasize the rebound effects. The first calculation, MCP-01, consisted of a homogeneous, incompactible halfspace with the properties of the second layer. In the second calculation, MCP-02, the soil layer of MC 2.12 was used over the MCP-01 halfspace. In the third experiment, MCP-03, the incompactible third-layer model was included from 11.4 feet to 19.2 feet depth, as previously described.

The influence of the soil layer was indicated by a comparison of velocity-vector plots (figures 29 and 30) near 9 msec. These plots showed that near the vertical axis the flow field was similar. The flow was mostly upward, with velocities along the vertical axis 20 percent greater for MCP-02 than for MCP-01. However, there was much greater upward motion of the region centered near 18 feet range and 4 feet depth in MCP-01 than in MCP-02. These results were caused by the hydrostat for the soil model. Since the maximum pressures in the soil near 18 feet were less than 100 bars (figure 23), the soil responded as a soft material with lower density than the material below it. Therefore, the air overpressures were not effectively coupled at either the airground interface or the material interface at this range. Furthermore, the soil layer was 72 percent compactible, which reduced the subsequent upward motion of this layer. When the direct-induced wave arrived in the lower material, a larger amount of the upward momentum was transferred to the soil to

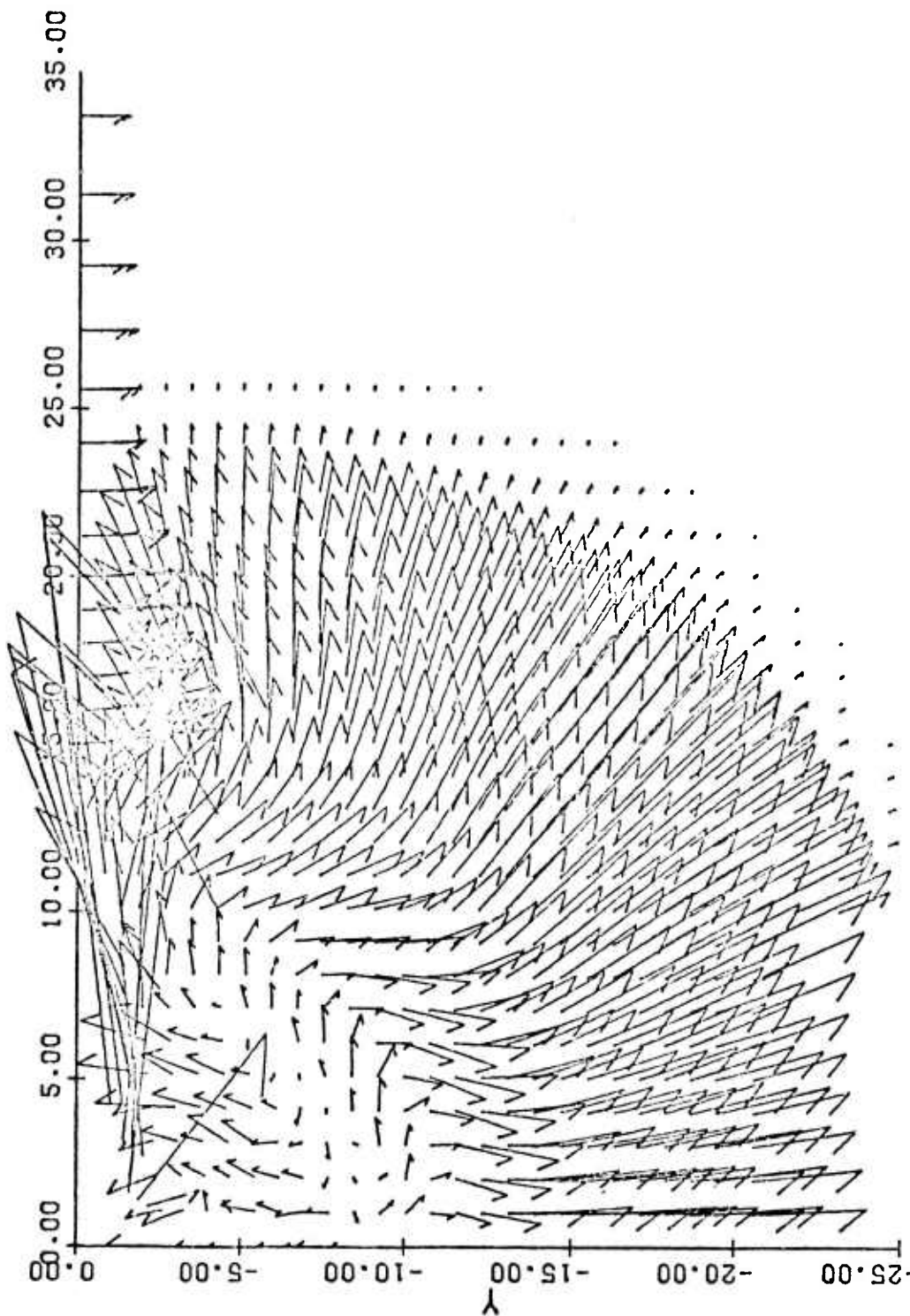


Figure 28. Velocity Vector Plot for MCP-09 at 2.8 msec after Detonation (Velocity is proportional to the vector length with the distance between axis marks equal 100 ft/sec; axes are in feet)

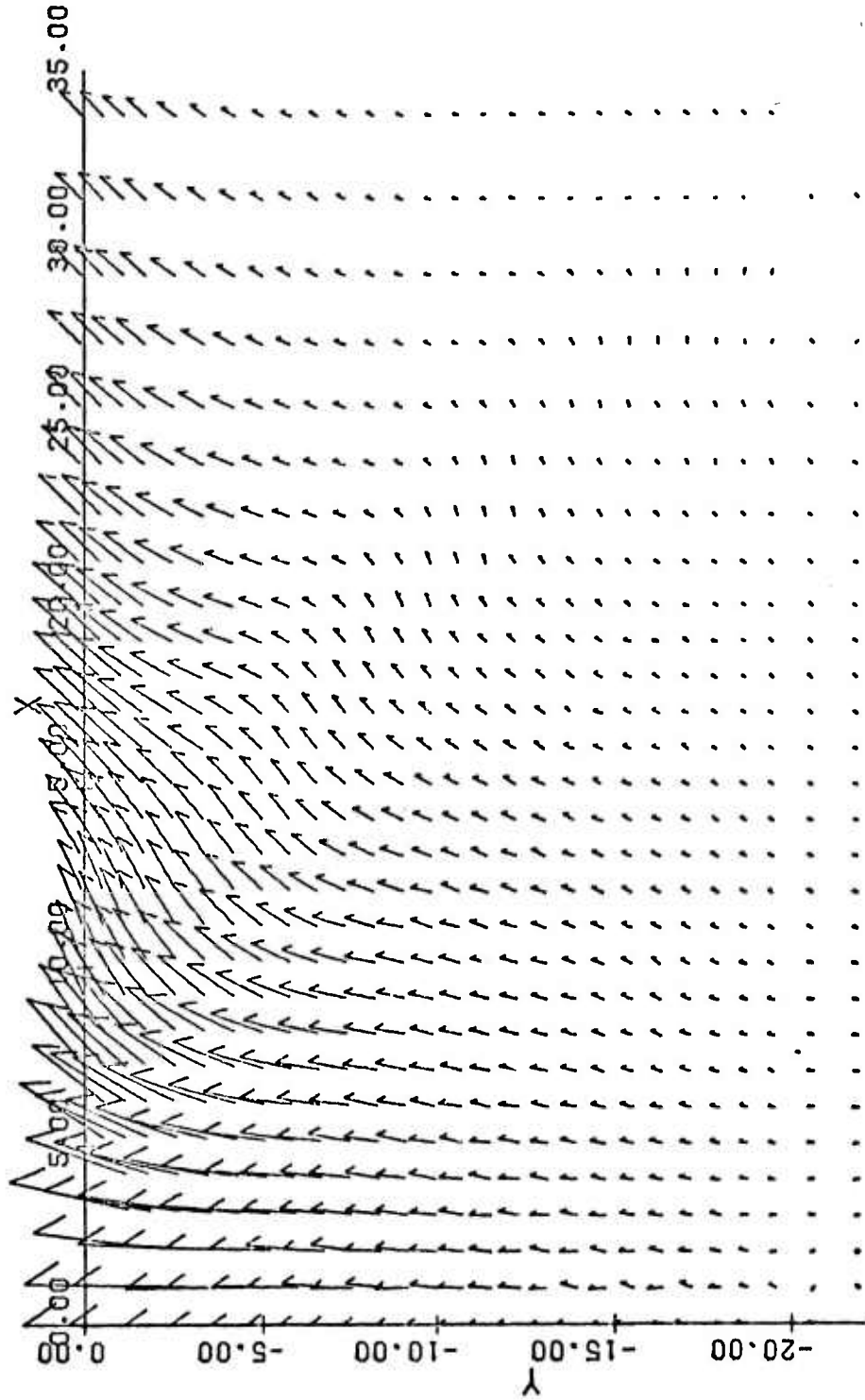


Figure 29. Velocity Vector Plot for MCP-01 at 8.4 msec after Detonation (Velocity is proportional to the vector length with the distance between axis marks equal 100 ft/sec; axes are in feet)

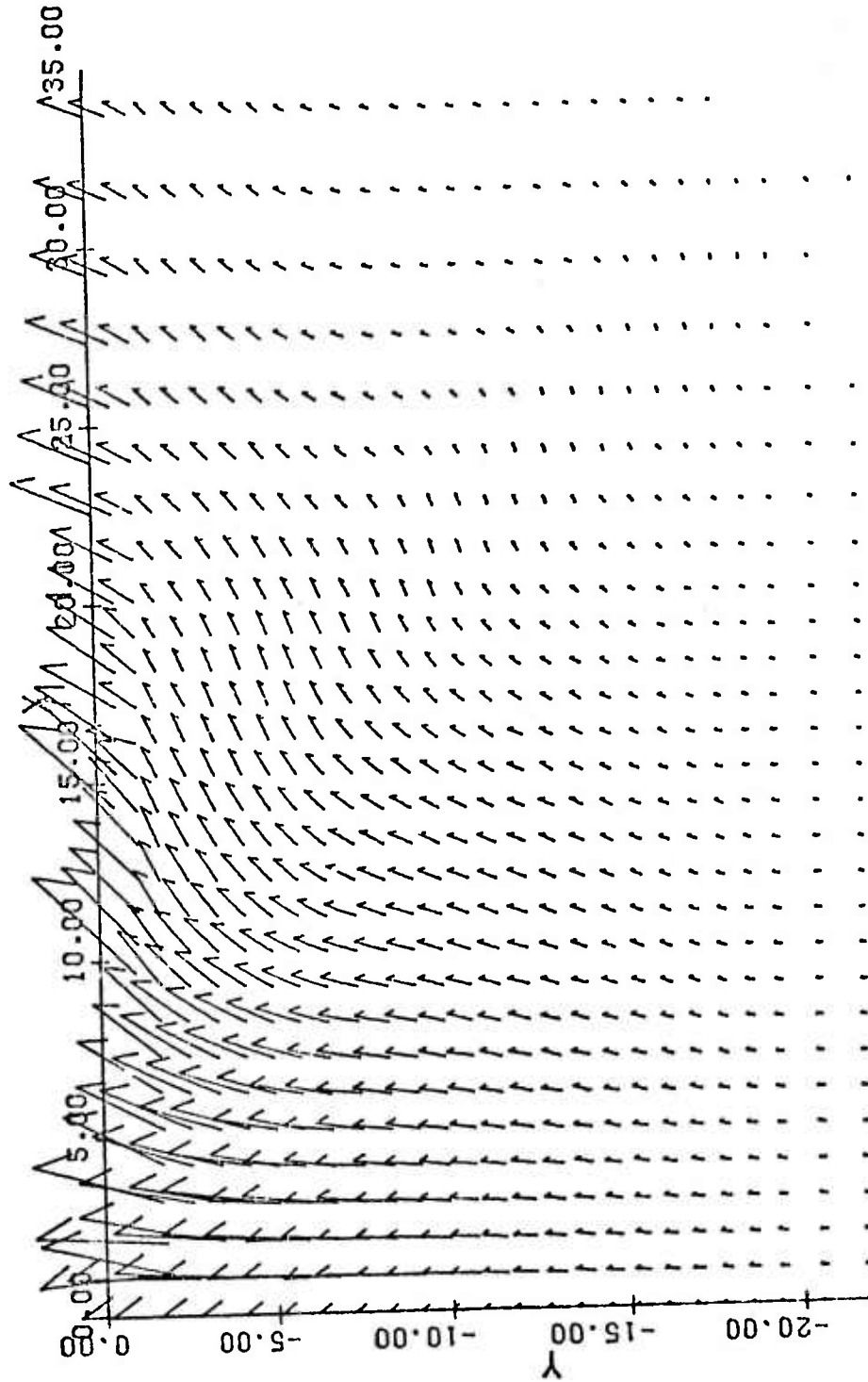


Figure 30. Velocity Vector Plot for MCP-02 at 9.5 msec after Detonation (Velocity is proportional to the vector length with the distance between axis marks equal 100 ft/sec; axes are in feet)

produce upward motions in the soil. However, at the 20-kbar pressures in the material below ground zero, both the soil and the lower material had similar densities and bulk moduli, which resulted in effective stress-wave transmission in this region. The result was that the soil layer only slightly affected the strong direct-induced signal in the lower material, but reduced significantly the effects of the air shock away from ground zero.

Comparisons between the MCP-02 and MCP-03 calculations showed that the increased acoustic impedance of the third layer only slightly influenced the upward motions that contributed to the calculated central uplift. The final upward velocities for target points on the vertical axis and initially located from 3 to 6 feet depth were 18 ft/sec higher for MCP-03 than for MCP-02. However, those target points were located in material that was calculated to be ejected from the crater. At deeper target points, the relationship between velocities changed until the final upward velocity of the target point at 10 feet depth in MCP-02 was 19 ft/sec, or almost 3 ft/sec higher than the value computed in MCP-03. The final velocities for lower target points on the vertical axis were also nearly equivalent in the MCP-02 and MCP-03 calculations.

In the calculations that included the third layer, the modeled von Mises yield strength controlled the yield condition during maximum stress conditions to a range of 6 feet above 16 feet depth in that layer. Although an additional calculation indicated that this control was not important to the calculated motions because of the limited region involved, the change of yield mode showed that the calculated response would be modified by increased stress-conditions.

c. Yield Model Effects

The yield model in the MC 2.12 calculation included a model of material strength that contained an assumed method of shifting the yield surface once the yield condition was met. This method had not been included in earlier numerical simulations of shock-wave cratering events. Therefore, the requirement for the shift and alternate ways of accomplishing the shift were examined in three numerical experiments.

The requirement for the shift of the yield surface was tested by a calculation, MC 2.15, to examine if a complete absence of tensile strength would also produce the observed crater without shifting the yield surface. The same model as MC 2.12 was used in the MC 2.15 calculation except the parameter

S was never changed from zero and the material was assumed to separate whenever negative pressures occurred. This model resulted in a completely different flow field that was not consistent with the observed crater. The plot of velocity vectors at 8.4 msec (figure 31) showed that in the second layer the material had large upward velocities only to a range of 8 feet and a depth of 6 feet. All the upward velocities below that depth were less than 10 ft/sec. Since there were no calculated stress conditions remaining at that time which would produce a change in this flow field, the MC 2.15 model was considered to be inadequate. This result indicated that a material model with no cohesion was required to simulate the formation of the central mound in the MIXED COMPANY II event.

Alternate methods of accomplishing the shift of the yield surface were tested in two numerical experiments. The MCP-02 calculation (the two-layer model of soil on an incompactible halfspace) was used as the standard model for these numerical experiments. In one calculation, the parameter S was incremented by 0.04 only during each of the first 25 calculational cycles that the yield condition was satisfied. In the second calculation, the parameter S was incremented by 0.04 only after the calculation of the yield condition was complete, which affected the yield surface only during subsequent calculational cycles. The calculated conditions during both of these numerical experiments showed little variation from the MCP-02 values.

The inclusion of a yield model in the computer code was a theoretical complication required because materials have finite strengths. To demonstrate the effects of the yield model on the calculated results, a no-yield assumption was used in one calculation. The MCP-02 model was used as a standard for this calculation, designated MCP-06, but the yield condition in the half-space below the soil was completely ignored.

A comparison of velocity-vector plots at 3.2 msec (figures 32 and 33, note change in velocity scale) showed that the yield model reduced the velocities experienced during the unloading from maximum stresses. In the no-yield model, the maximum downward velocity and maximum normal stress of the compressional wave near the vertical axis were nearly equal to the analogous values when the yield model was included. However, in the no-yield case these values were immediately reduced after maximum compression, so that the downward velocity was only 5 ft/sec by 20 feet depth. The change in velocity direction that occurred at a 21-foot radius from the origin was associated with a change from

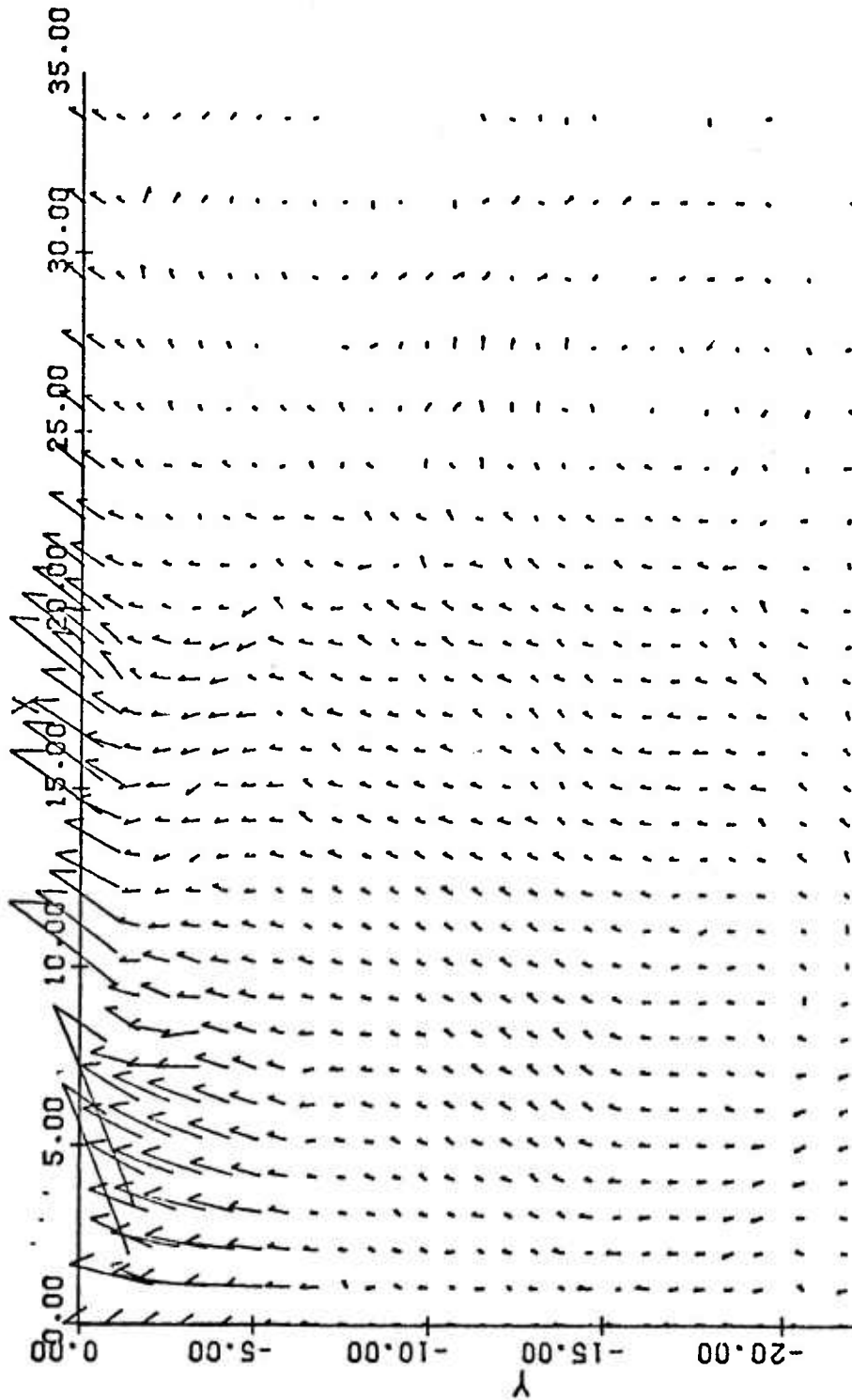


Figure 31. Velocity Vector Plot for MC 2.15 at 8.4 msec after Detonation (Velocity is proportional to the vector length with the distance between axis marks equal 100 ft/sec; axes are in feet)

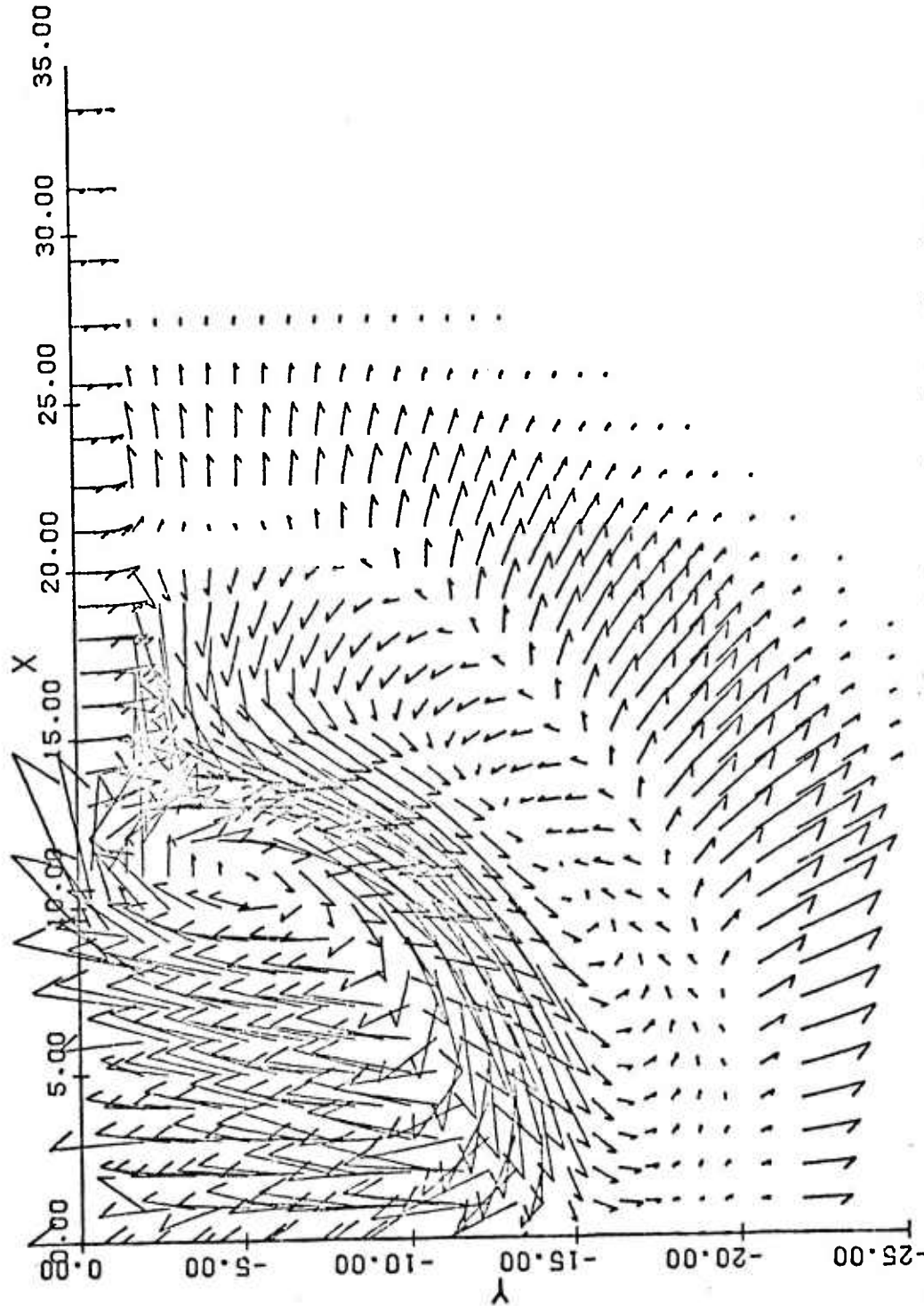


Figure 32. Velocity Vector Plot for MCP-06 at 3.2 msec after Detonation (Velocity is proportional to the vector length with the distance between axis marks equal 200 ft/sec; axes are in feet)

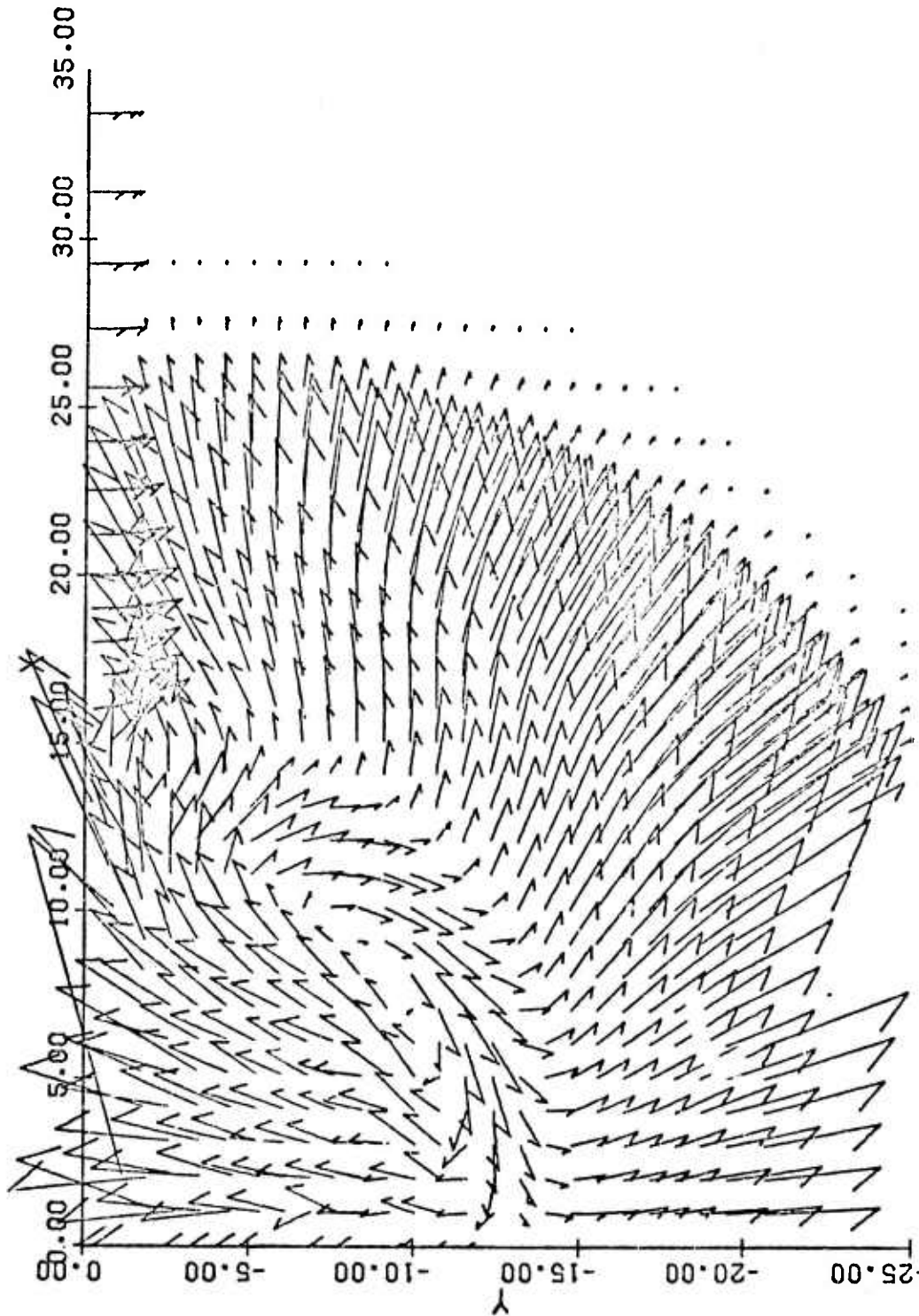


Figure 33. Velocity Vector Plot for MCP-02 at 3.2 msec after Detonation (Velocity is proportional to the vector length with the distance between axis marks equal 100 ft/sec; axes are in feet)

positive to negative pressures, which did not occur in the MCP-02 calculation. Significant inward velocities, as high as 127 ft/sec at 2.6 feet depth and 17 feet range, occurred before the arrival of the shear wave caused clockwise rotation. The shear wave produced downward velocities as high as 135 ft/sec near the surface with inward velocities as high as 150 ft/sec at the 12.3-foot depth and 7-foot range. These values were five times as large as velocities produced by the calculated shear wave in the MCP-02 model. Behind the shear wave, the upward velocity on the vertical axis reached 147 ft/sec at 12.3 feet depth and remained near 100 ft/sec to 1.8 feet depth.

The yield model in the MIXED COMPANY II numerical simulation included the associated flow rule, the use of which in numerical ground-motion simulations is a recent development. As late as 1971, the Prandtl-Reuss flow rule was used to describe plastic stress-strain relations in numerical ground-motion simulations (Zelasko and Baladi, 1971; Trulio, et al., 1969). As noted before, the only difference between the two flow rules, if the yield surface is independent of the third invariant of the deviator stresses, is the bulking included in the associated flow rule when the yield surface is a function of pressure. The effect of the associated flow rule was examined in a numerical experiment, MCP-05, in which the Prandtl-Reuss flow rule was used with the MCP-02 model.

The MCP-05 calculation resulted in a completely different response of the medium to the applied boundary conditions. Calculated motion remained predominantly downward and away from the axis of symmetry until 10 msec with no rotational motion, which was an outstanding feature of the MCP-02 calculation at 3.2 msec. At 10 msec, inward velocities as high as 2 ft/sec were calculated to a depth of 26 feet and range of 33 feet; however, vertical motion was still downward at velocities less than 10 ft/sec within a range of 15 feet. By the simulated time of 11.4 msec, the downward motion near the vertical axis had stopped and upward velocities as high as 10 ft/sec were calculated near the vertical axis to a depth of 20 feet. Also, at this time, the motion below 9 feet depth was inward with velocities less than 2 ft/sec, and material separation has occurred along the axis to a depth of 4 feet. The material separation front proceeded downward and outward at a speed of 3000 ft/sec until, by 19.9 msec, the flow pattern shown in figure 34 has developed with stresses within a 23-foot radius from the origin calculated to be near zero. During the entire calculation, upward velocities never exceeded 15 ft/sec in the halfspace below the model soil layer.

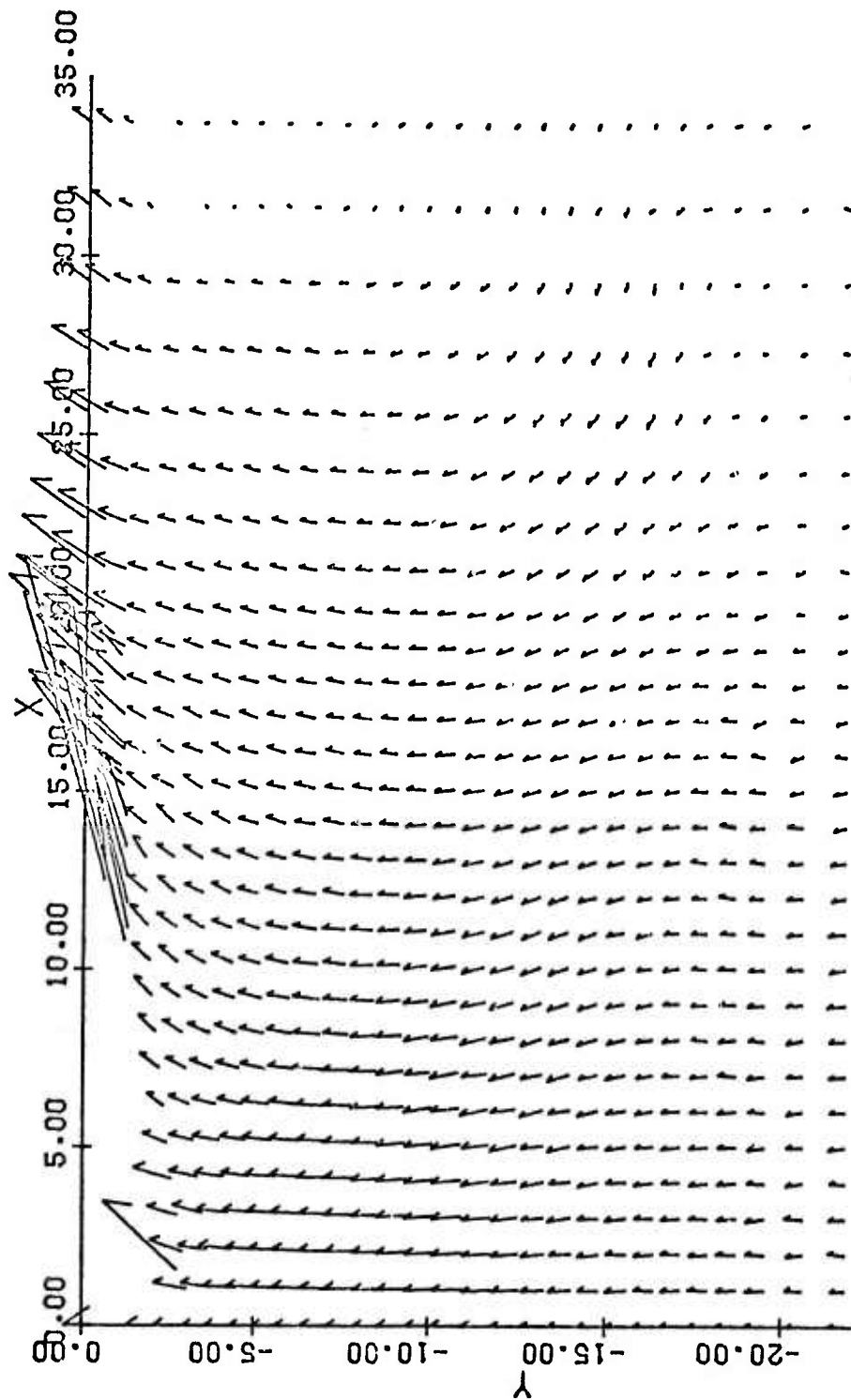


Figure 34. Velocity Vector Plot for MCP-05 at 19.9 msec after Detonation (Velocity is proportional to the vector length with the distance between axis marks equal 50 ft/sec; axes are in feet)

In the MIXED COMPANY II numerical simulation and all subsequently described calculations, the yield condition for the material below the soil layer was usually determined from the Mohr-Coulomb relation as a result of the high von Mises limits. Therefore, the effect on the MCP-02 calculation of lowering the von Mises limit was tested. For this test, designated MCP-21, the von Mises limit in the material below 1.8 feet depth was set at 0.21 kbar; and, because calculated displacements were too large to allow calculation with a completely Lagrangian coordinate system, the generalized coordinate capability of the AFTON-2A code (Trulio, 1966) was used for grid points initially at and above 10.6 feet depth. The grid points in that region had fixed radial coordinates but were allowed to move vertically to retain proper stratigraphic relations. The properties of the mass that was transported across calculational faces were determined from the values in the zone out of which the material was being transported, and were "backward" transport terms (Trulio, 1964; Cooper, 1971). The coordinate system remained Lagrangian below 10.6 feet depth.

The time and location of the first upward motion on the vertical axis were accurately determined in this calculation. Near the vertical axis, upward velocities were first calculated between 5.6 msec (figure 35) and 6.9 msec (figure 36) with downward motion near the axis still calculated below 18 feet and above 7 feet depth. The velocity transition region, near 16 feet depth and 5 feet range, was not associated with exceptional stress or acceleration conditions and only represented the null region of a continuous decrease in outward velocities. Continuation of the calculation to 10.5 msec (figure 37) showed that velocities with inward components as large as 2.5 ft/sec and upward components as large as 20 ft/sec were calculated below 10 feet depth. The first upward motion on the vertical axis occurred near 12 feet depth at a simulated time of 6.3 msec.

The motion and stress histories (figures 38 and 39) of that target point were, therefore, especially pertinent to an examination of the mechanics of central mound formation. The first signal was an elastic precursor that arrived at 1.4 msec and caused the stress conditions to reach the yield surface. The plastic wave then arrived at 1.9 msec, when the maximum compression and downward velocity were reached. In this plastic wave the stress deviators were controlled by the von Mises yield condition and, therefore, the associated flow rule became equivalent to the Prandtl-Reuss flow rule. Also, there was a significant difference between the maximum and minimum normal-stress values. After

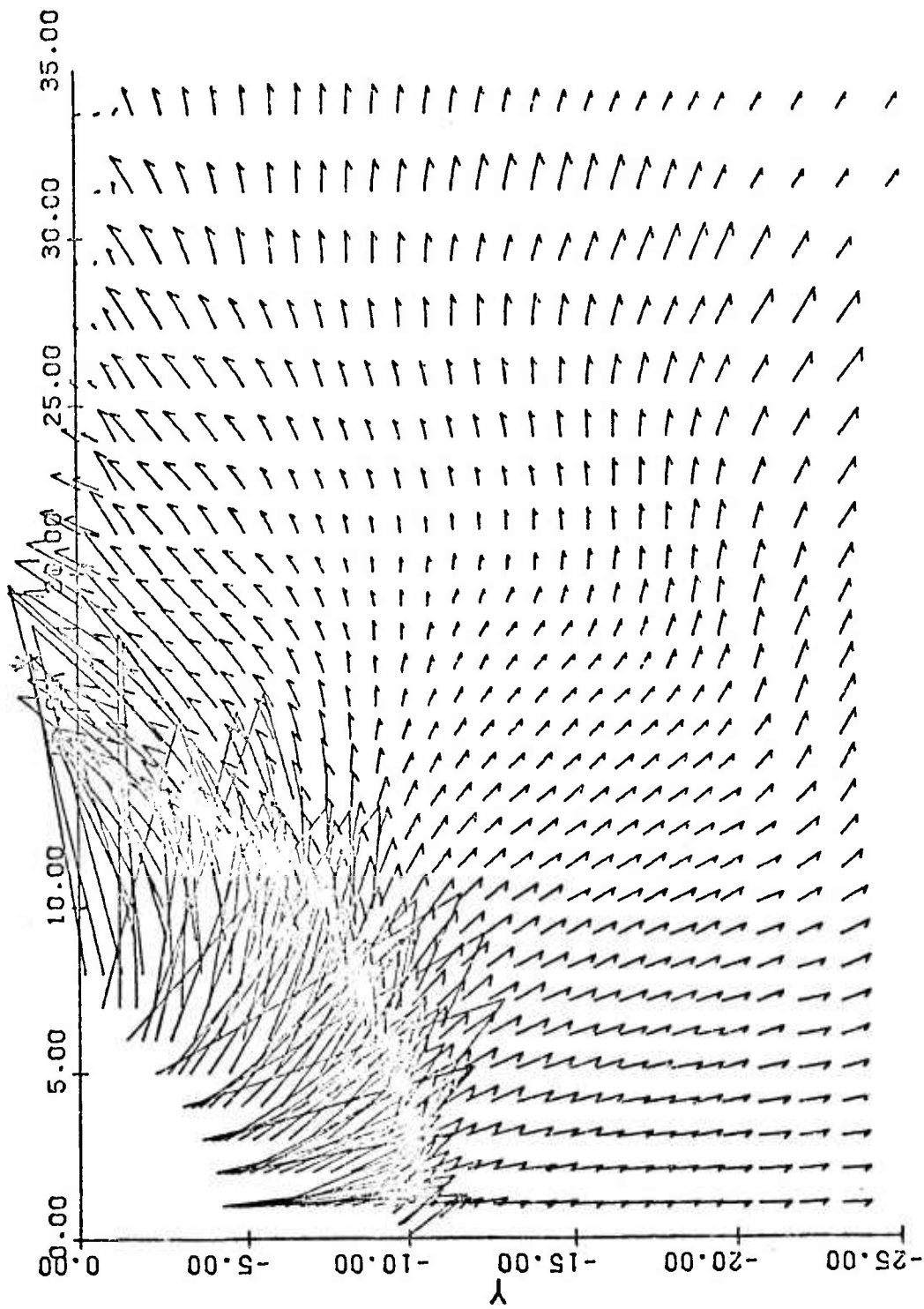


Figure 35. Velocity Vector Plot for MCP-21 at 5.6 msec after Detonation (Velocity is proportional to the vector length with the distance between axis marks equal 100 ft/sec; axes are in feet)

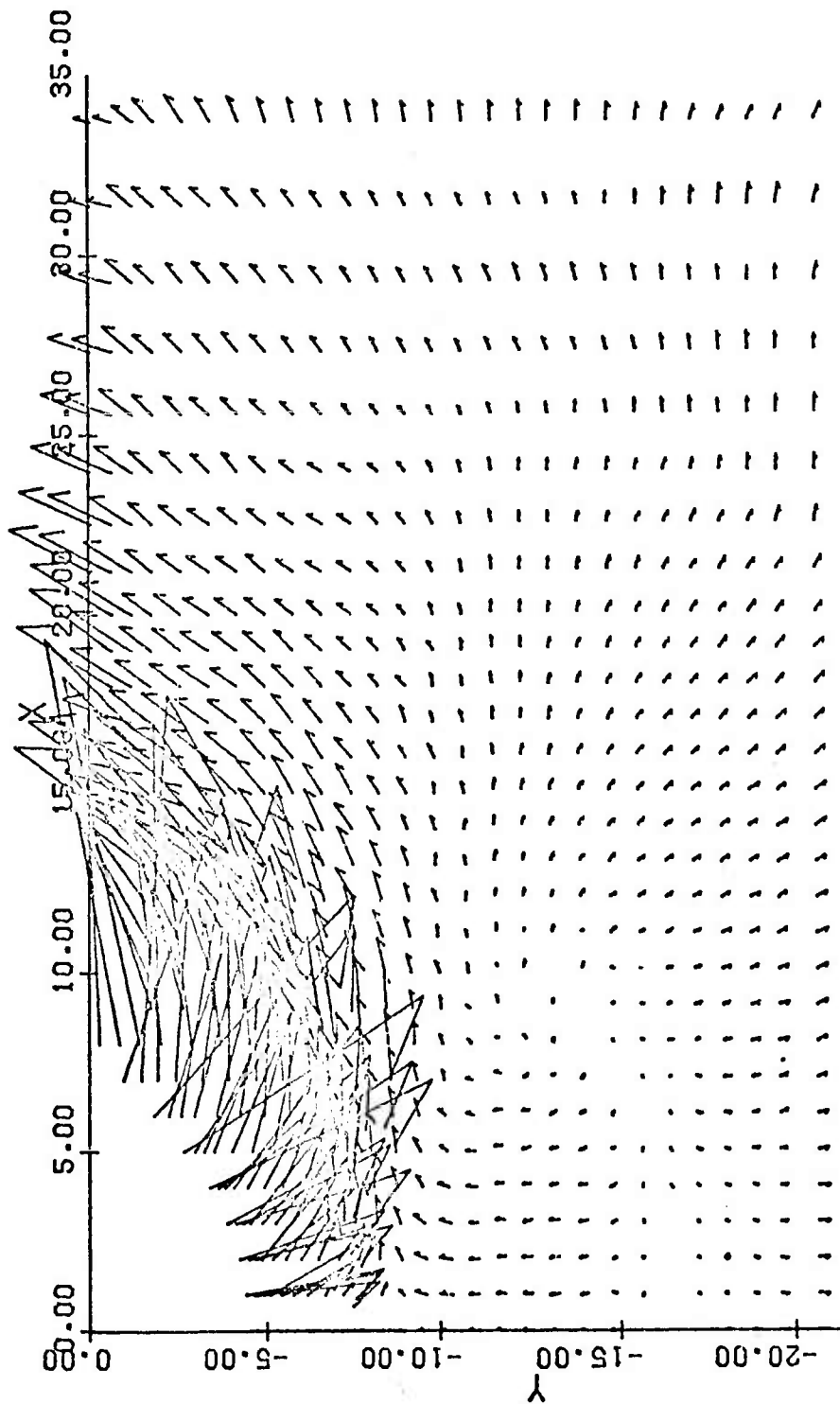


Figure 36. Velocity Vector Plot for MCP-21 at 6.9 msec after Detonation (Velocity is proportional to the vector length with the distance between axis marks equal 100 ft/sec; axes are in feet)

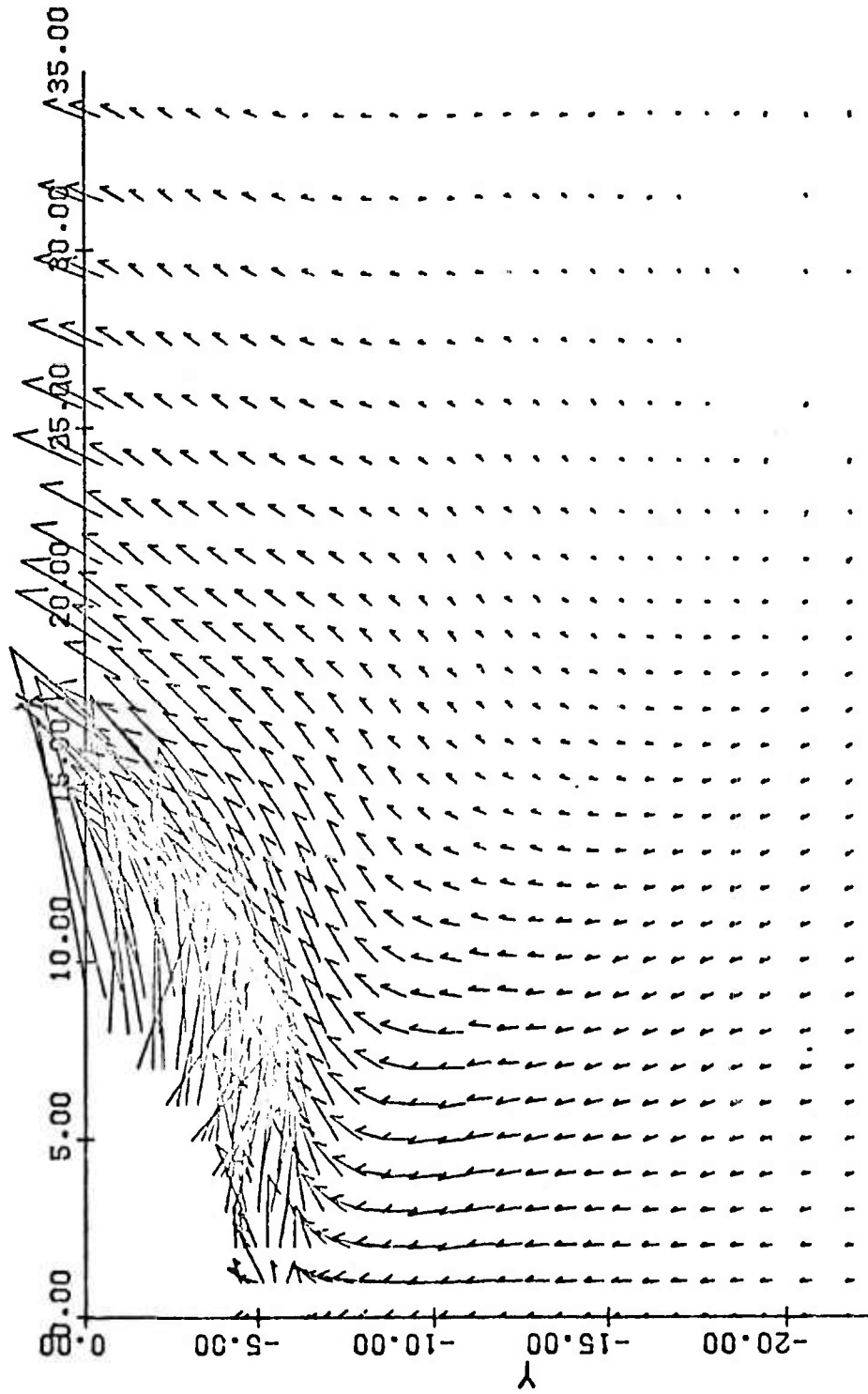


Figure 37. Velocity Vector Plot for MCP-21 at 10.5 msec after Detonation (Velocity is proportional to the vector length with the distance between axis marks equal 100 ft/sec; axes are in ft)

2

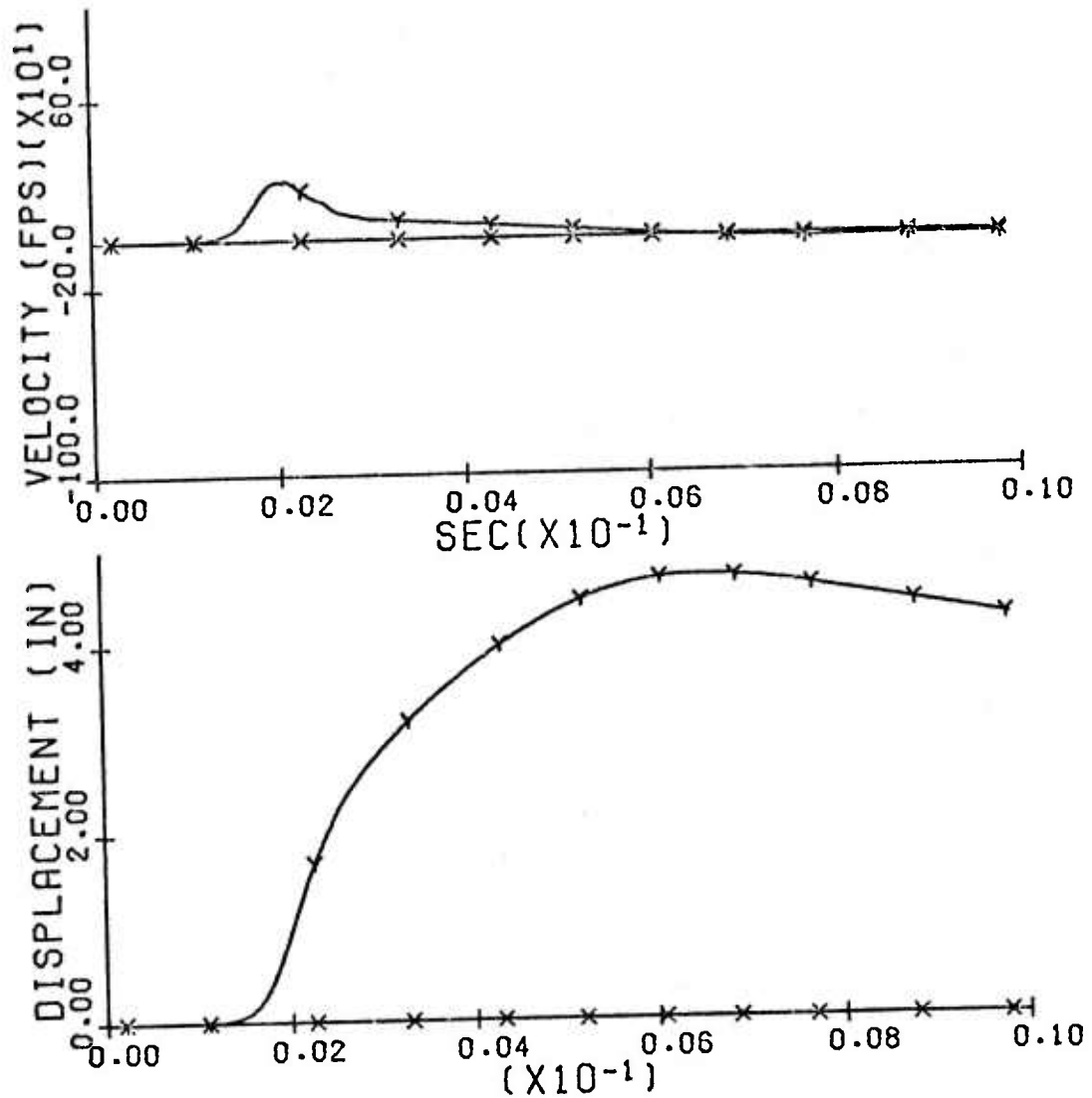


Figure 38. Motion Time History for the Target Point Originally Located on the Vertical Axis at 12 Feet Depth in the MCP-21 Calculation (Positive Y values indicate downward motion)

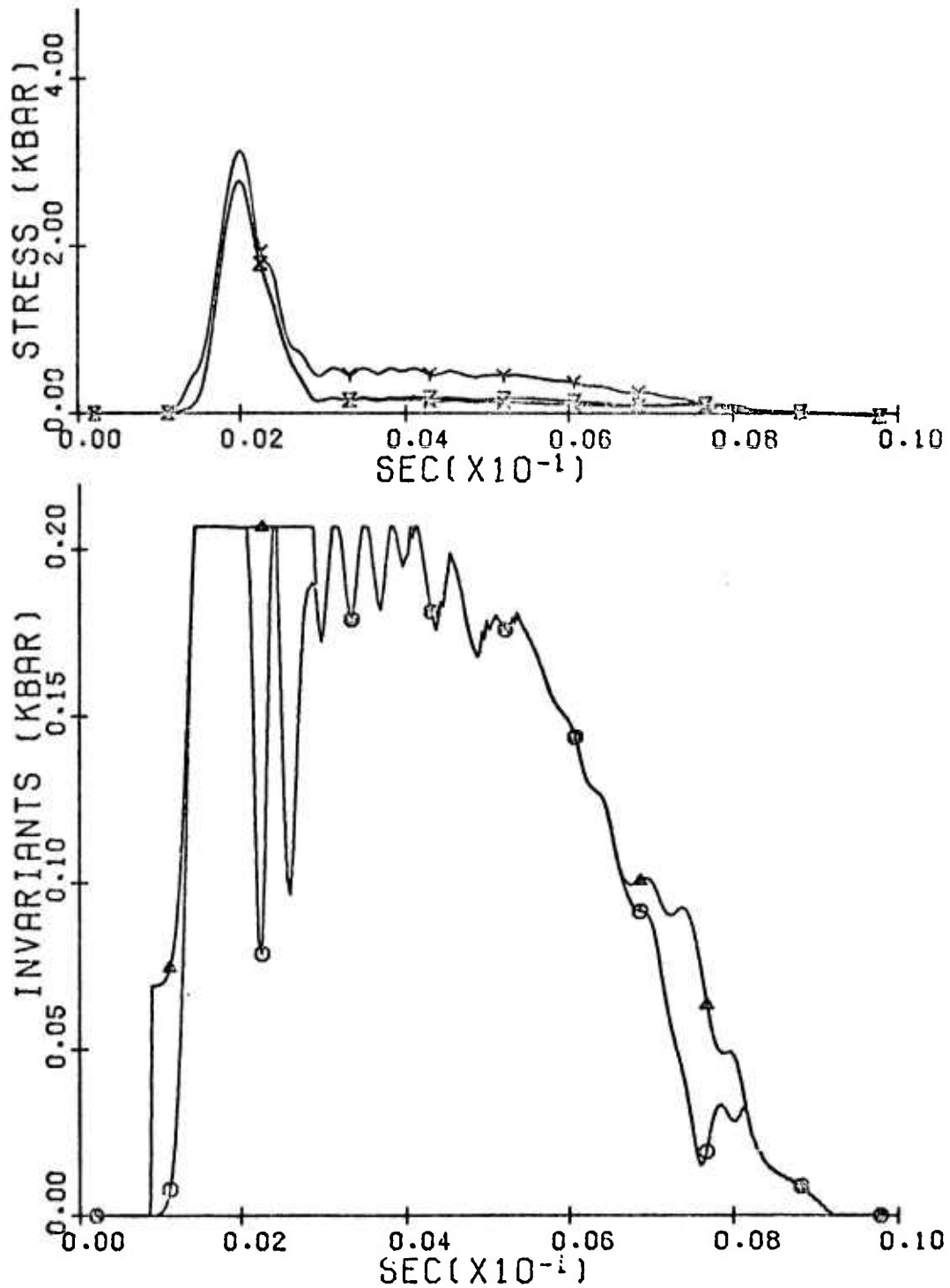


Figure 39. Stress Time History for the Target Point of Figure 38 with Compressive Stresses Positive (Y is vertical; X is radial; Z is tangential; Δ is yield condition; O is the second invariant of the deviator stresses; the constant yield condition between 1 and 3 msec is the von Mises yield condition)

the maximum stresses occurred, the stresses were rapidly reduced, under elastic conditions, interrupted only by the second compressional signal. A lower stress state was then reached and maintained for a period of 3 msec, during which the yield surface again controlled the deviator stresses. This time, however, the yield surface was controlled by the Mohr-Coulomb relation, which resulted in volumetric bulking. Thus, while nearly constant stress conditions were maintained, because of the downward momentum of the material above this target point, the downward velocity was continuously reduced until the motion stopped at 6.3 msec and reversed direction. After 6.3 msec, the vertical compressive stress was reduced while the horizontal normal stresses remained significant, which resulted in elastic deformation while the vertical stress approached zero. The reduction of the vertical stress lowered the pressure and, therefore, the yield condition so that the horizontal stresses were finally reduced by material yield until material separation occurred at 9 msec.

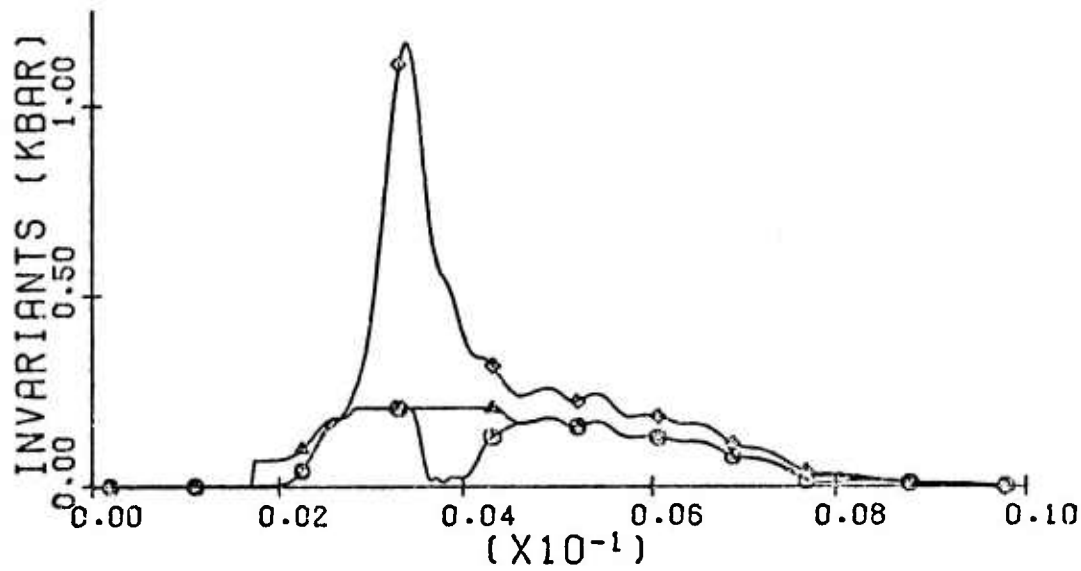
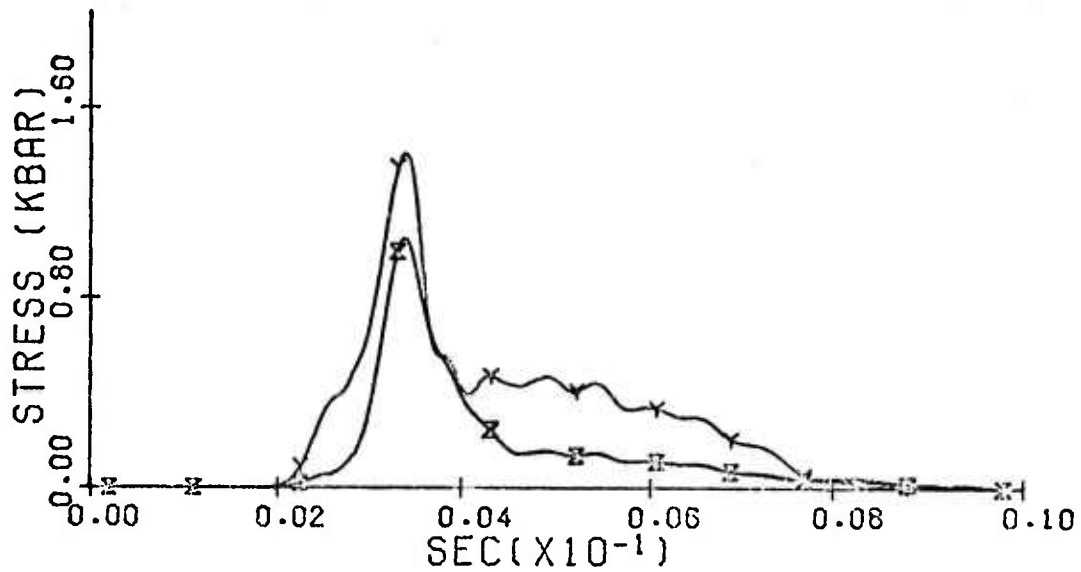
The stress time history of the target point on the vertical axis and initially at 20 feet depth (figure 40) provided an example of the elastic-precursor development that is actually observed in shock experiments (Ahrens and Rosenberg, 1968), and served as a simple demonstration that strength effects were properly treated by the AFTON-2A code. The first calculated stress wave arrived near a simulated time of 2.5 msec, after traveling most of the distance from the surface at a compressional wave speed of 8000 ft/sec. The main plastic wave, however, travelled with the stresses controlled by the von Mises yield condition, and the wave speed was

$$c_b = \left(\frac{K}{\rho_i} \right)^{1/2} \quad (16)$$

which from relation (4), became

$$c_b = c_p \left[\frac{1 + \nu}{3(1 - \nu)} \right]^{1/2} \quad (17)$$

The wave speed, c_b , computed from equation (17) was 5656 ft/sec, which was consistent with the maximum-pressure arrival near 3.5 msec. Further, from Ahrens and Rosenberg (1968), the Hugoniot elastic limit is related to the von Mises yield condition by



- Y - vertical
- X - radial
- Z - tangential
- ◇ - pressure
- △ - yield condition
- - second invariant

Figure 40. Stress Time History for the Target Point Originally Located on the Vertical Axis at 20 Feet Depth in the MCP-21 Calculation (Compressive stresses are positive)

$$Y_{MAX} = \frac{3GP_e}{3B + 4G} \quad (18)$$

with P_e the maximum elastic normal stress and B the bulk modulus. Relation (18) was transformed to

$$P_e = 2Y_{MAX} \left[\frac{1 - \nu}{1 - 2\nu} \right] \quad (19)$$

by elastic relations between B , G , and ν . With the values used in MCP-21, relation (19) implied a P_e of 0.56 kbar, which was the maximum normal stress at the time the von Mises yield condition was reached.

d. Lower "Fluid" Layer

An initial attempt was also made to apply the study of central mounds to an examination of lunar evolution. Two lunar craters, Lansberg (0°N, 26.5°W) and Reinhold (3°N, 23°W) are very similar except that Lansberg has a central peak while Reinhold has no such feature. Reinhold is 27.5 miles in diameter and 1.7 miles deep (Schmitt, et al., 1967), and Lansberg is 25 miles in diameter and 1.6 miles deep (Eggleton, 1965). These two craters are within 125 miles of each other (both southwest of Copernicus in Oceanus Porcellarum) and are probably located in similar material. The main difference between the two craters, other than the presence of a central mound, is that Lansberg is overlain by Oceanus Porcellarum material while Reinhold overlies that material (Schmitt, et al., 1967).

One explanation of the relationship between these two craters is that conditions favoring central mound formation existed at the time Lansberg was formed and were sufficiently modified by the time of the Reinhold event to prevent the formation of a similar mound. Perhaps, at the time Lansberg was formed, a solid crust, approximately one crater radius thick, existed over a molten layer; while, by the time Reinhold was formed, the crust was much thicker. Such a relation of a growing crust is contained in several published thermal models (Toksoz, et al., 1972; McConnell and Gast, 1972) and is used by Simmons, et al., 1973, to account for the discontinuous increase in seismic velocity at a depth of 15 miles with a constant seismic velocity in the depth interval 15 to 30 miles on the moon.

The impact calculations required to test fully such a model of the relation between these two craters were not accomplished. However, a calculation, MCP-12, was completed that inserted a model "fluid" halfspace below 16.2 feet depth in the MCP-02 model to provide a preliminary test of the influence of such a medium. In the MCP-12 calculation, the "fluid" was modeled by an incompactible hydrostat, with the values

Initial density - 2.47 gm/cc
Seismic velocity - 6000 ft/sec
 u_3 - 0.0229
Poisson's ratio - 0.45

and to simulate viscosity a constant yield surface value of 34.5 bars for compressive pressures with material separation assumed for negative stresses. Also, since the transmitting boundary assumed impinging elastic waves, the bottom boundary was located at 156.2 feet depth. A special "sliding" interface condition, which limited the shear stress transmitted across the interface to the shear capability of the fluid (Niles, et al., 1971), was used at the solid-fluid interface.

The calculated flow field at 16.6 msec (figure 41) showed that the "fluid" layer extensively influenced the motions of the solid material above the interface. This effect was particularly strong in a cylindrical region of 15 feet range and below 9 feet depth where the motion, instead of being upward as in the MCP-02 calculation, was downward with velocities as high as 70 ft/sec. This motion was producing large downward material displacements with the cylinder of solid material, which was completely separated, moving into a developing depression in the "fluid." The motion in this "fluid" was similar to that calculated by Harlow and Shannon (1967) for the splash of a liquid drop into a deep pool, and an extension of this calculation would be expected to develop large upward velocities near the axis of symmetry as the fluid recovered under gravitational flow. The amount of this recovery would be controlled by the properties of the fluid, which is speculated to control also the development of a central mound formed by the solid material as that material is redirected upward by the fluid.

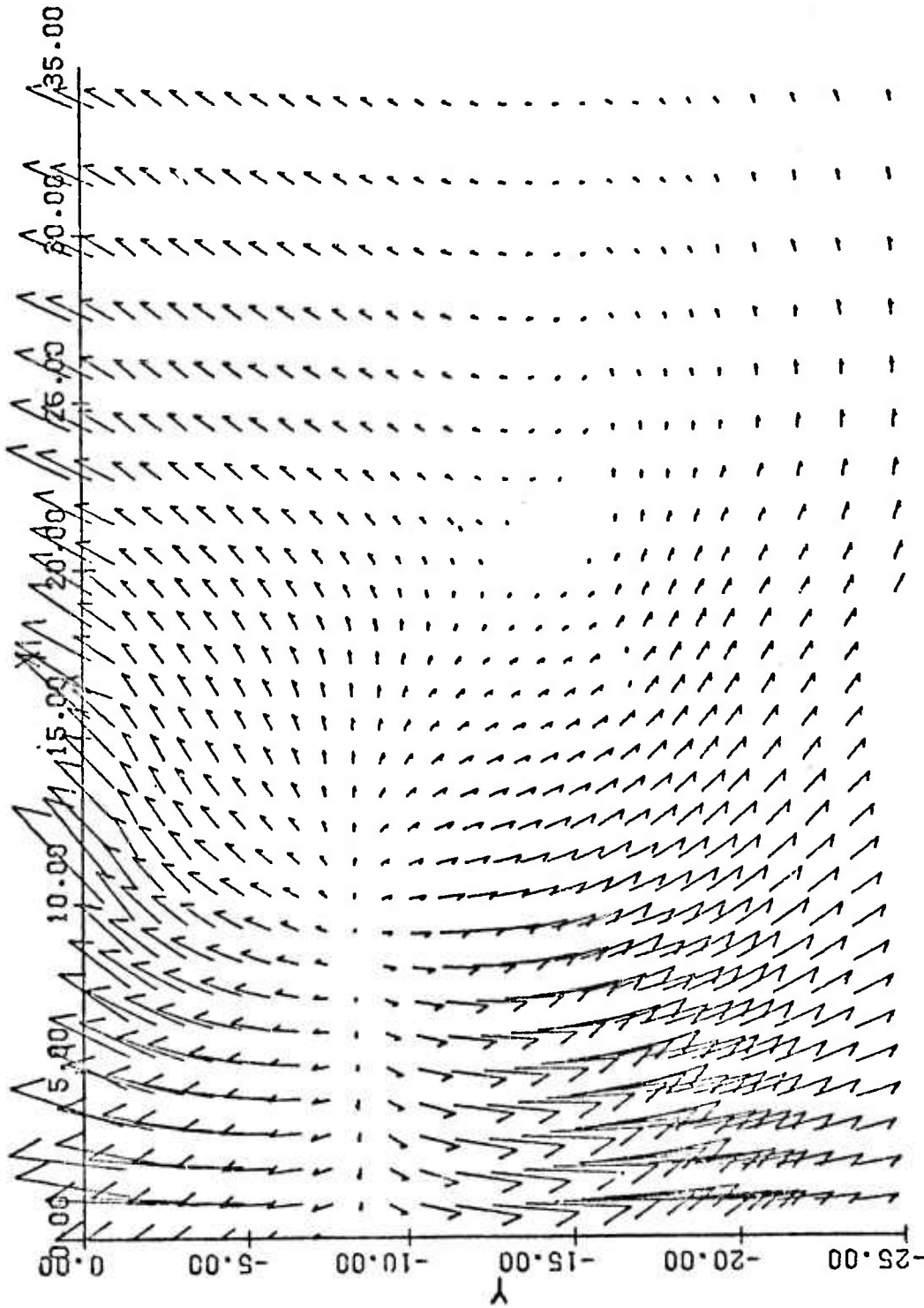


Figure 41. Velocity Vector Plot for MCP-12 at 6.6 msec after Detonation (Velocity is proportional to the vector length with distance between axis marks equal 100 ft/sec; axes are in feet)

SECTION IV
DISCUSSION AND CONCLUSIONS

1. DISCUSSION

a. Evaluation of Results

Numerical modeling of physical events is subject to two basic causes of error. One of these causes is the numerical error caused by replacing the space and time continuums with a discrete grid on which calculations are accomplished at specific moments in time. This form affects the accuracy of the calculated numerical values and usually can be reduced by decreasing the grid spacing and calculational time increments. Evaluation of this form of error in complex calculations can only be inexact; however, from previous investigations of numerical error in the AFTON-2A code (Cooper, 1971; Trulio, et al., 1967), such errors are not expected to seriously affect relations between calculated values. The second, and more serious, cause of error is the use of invalid mathematical models for the actual physical processes. This cause of error can result not only in numerical values that are incorrect, but also in a calculated response that is completely invalid.

The MIXED COMPANY II numerical simulation, MC 2.12, was subject to modeling errors of both forms in the three models. The first was the model of the overpressure boundary condition used to simulate the high-explosive event. This model has been suggested (Trulio and Perl, 1973) to underestimate the overpressure impulse of the MIDDLE GUST III event by at least 40 percent at ground zero. The second was the model of the ground response to the overpressure boundary conditions during the first 16.4 msec. This model included only approximations of (1) the test site, (2) the properties of the materials at that site, and (3) descriptions of physical relations. The third model was the ballistic extension of the calculated conditions at 16.4 msec.

A necessary but not sufficient condition for the models to provide a simulation of the actual physical processes is that the calculated final conditions are the same as the final conditions observed after the physical event. The results of the MIXED COMPANY II numerical simulation do not completely meet this condition; however, the calculation may still be useful to a study of

central peak mechanics if the inadequacies of the models do not include the causes of central mound formation.

Thus, the interpretation that the model produced insufficient displacements below ground zero is considered to be the major discrepancy of the simulation. Since the ballistic extension model is not expected to underestimate the displacements, the cause of this discrepancy is thought to exist in at least one of the first two models. One possible cause is that the impulse of the model overpressure was too low. An increase of the overpressure impulse would cause a stronger shear wave and more bulking, because the stresses and the compressional pressure duration would be greater. Another possible cause is that the dependence of the yield surface on the third invariant of the deviator stresses was not included in the yield model. In many natural materials, the yield surface is dependent on the third invariant (White, 1973), which indicates that the yield model used in the numerical calculations was incomplete. Other possible causes of the discrepancy include errors in the values used to model the test site and numerical error.

b. Mechanical Model of Central Mound Formation

However, the development of a model of the causes of central mound formation is warranted because the final conditions calculated in the MIXED COMPANY II numerical simulation are sufficiently similar to the observed conditions after the physical experiment. The results of the numerical experiments (table 4) can be used as a guide to this model. In this model, the principal cause of central mound formation is the rebound of material following the maximum shock pressure. If this rebound is sufficiently reduced by compaction of the materials, a central mound will not form in the crater unless there is a material below the bottom of the crater that responds like a fluid to produce a gravitational splash jet. The rebound must occur in the region where material strengths are sufficient to retard some of the outward displacements caused by the initial compressional wave. The formation of the central mound is enhanced by the bulking of material as the material brecciates and by the inward motion caused by the principal shear wave. Inward displacements, however, are associated with a ductile response of the material. The presence of material discontinuities below the forming crater will reflect stress waves that might add to the formation of a central mound. Because of the reduced density in the region forming the central uplift, a period of material separation exists that

Table 4

SUMMARY OF NUMERICAL SIMULATION RESULTS

	<u>Model Designation</u>	<u>Baseline Model</u>	<u>Model Change</u>	<u>Major Result</u>	<u>Page Ref.</u>
1.	MC 2.12*	Numerical simulation of MIXED COMPANY II with a hydrostatic compaction factor (page 41) of 10 percent		Generally consistent with observations	61
2.	MC 2.13*	MC 2.12	30% compaction	No central mound	80
3.	MCP-09*	MC 2.13 MC 2.12	10% compaction different release adiabat	Like MC 2.12	84
4.	MC 2.15	MC 2.12	Cohesion retained	No central mound	91
5.	MCP-02*	No compaction two layers	-	Central mound	87
6.	MCP-01	MCP-02	No soil	Little change in central mound	87
7.	MCP-03	MC 2.12	No compaction	Increased velocities	83
8.	MCP-05*	MCP-02	4 layers	Little change	90
9.	MCP-06	MCP-02	No bulking (Page 45)	Completely different	97
10.	MCP-07	MCP-02	No yield	Large transient velocities	96
11.	MCP-08	MCP-02	Shift during yield	No change	93
12.	MCP-12*	MCP-02	Shift after yield	No change	93
13.	MCP-21*	MCP-02	"Fluid" layer	Probable fluid splash	112
			0.21 kbar yield	Deeper upward motions	99

*Important implications for central peak formation

may allow the gravitational sliding of the crater walls along deep slip surfaces to produce additional inward displacements.

c. Applications to Previous Information

The general applicability of this mechanical model of central mound formation can be tested by comparisons with previous observations of central

mound occurrence. Such a model should also provide a means of understanding and evaluating previous calculations.

Comparisons should first be made with the high-explosive experiments to determine if such a model is successful under loading conditions similar to those for which the model was first determined. The absence of central peaks in the 20-ton detonations in Canada would be attributed to the compactibility of the top 25 feet of soil at that site. The presence of central mounds in the higher-yield experiments would indicate that the lower, less-compactible material was being significantly influenced. The ductile characteristics of the deformation in those central mounds can either be attributed to the independence of the yield surface on confining pressure or to a "fluid" action of the material below 25 feet depth. The occurrence of a central mound in the 100-ton spherical event and not in the 100-ton hemispherical event can be attributed to an increased precompaction of the soil below the spherical charge combined with an increased overpressure impulse at ground zero. The mechanical model is also applicable to the MIXED COMPANY test series. The MIXED COMPANY I and III high-explosive detonations certainly caused higher stresses in the medium (which caused more ductile-like behavior of the layer at 12 feet) than the MIXED COMPANY II experiment. This ductile-like behavior resulted in less-pronounced central mounds in the first and third experiments than the large breccia cone of the MIXED COMPANY II event. Further evidence of the effect of a change in yield mode is provided by the central mound of the MIXED COMPANY I experiment with the intact flanks and the brecciated central core. The MIDDLE GUST series is less easily interpreted because of the jointing in the test sites; however, the test series does indicate that the more ductile-like behavior of the material at the MIDDLE GUST sites than at the MIXED COMPANY site resulted in more subdued central mounds. The transition from central mounds to the central trough of the MIDDLE GUST III event was caused by the higher stresses that reached the lower shale layer. Comparisons between the three test series illustrate the influence of compactibility on the occurrence of central mounds and of yield mode on the deformation in the central mound.

Comparisons with impact structures provide a test of the applicability of the model to a different form of loading. As the presence of shatter cones indicates, the maximum stresses in the central mounds were above but near the Hugoniot elastic limit, producing ductile failure with eventual inward displacements. The change in the yield mode at increased depths results in a central

mound with a breccia core of reduced density. The dependence on gravity, suggested by Hartmann (1972), would be caused by the initial overburden stresses reducing the porosity of deeper material, combined with the additional rebound caused by the dynamic excavation of the crater. The increased pressures caused by the lithostatic load would also cause a higher Mohr-Coulomb yield value, which would increase the bulking and shear-wave magnitude. The change from central peaks to peak rings may be caused by a gravitational collapse of the breccia core or a complete penetration of a solid crust. The transition from simple to complex impact structures in Canada may be caused by similar gravity influences combined with a weathering of the Canadian shield to a depth of one to two miles, with an increased jointing, porosity, and a reduced material strength.

A further test of the model is actually provided by its use to explain why central peaks do not occur in some shock-wave cratering events. The Barringer crater has no central mound because it was formed in porous sandstone. All the nuclear tests occurred in or over compactible material. The hyper-velocity impact experiments in loose sand targets produced only simple crater shapes.

An understanding of the results of previous calculations is facilitated by use of the mechanical model. Since the ELK-31 soil model was precompacted before the beginning of the calculation, upward motions were calculated only in that numerical simulation of the DISTANT PLAIN 6 experiment. Upward motions were calculated in the Sierra Madera numerical simulation, which was considered to successfully model the event. However, the motions in this calculation resulted from invalid physical models. In particular, a no-strength condition was assumed once the calculated pressure in a zone was negative. Because of this assumption, the calculation actually simulated the response to gravitational force of a perfect fluid surrounding an initial void. Evidence supporting this interpretation of the calculation is that the calculated motions required a simulated time of 15 seconds to develop fully and were still prevalent at a simulated time of 30 seconds. Errors in the calculational model which probably reduced the earlier upward velocities included the use of information from only a Hugoniot curve to determine all the parameters of an equation of state, and an initial yield strength of 0.2 kbar that was independent of pressure.

THIS REPORT HAS BEEN DELIMITED
AND CLEARED FOR PUBLIC RELEASE
UNDER DOD DIRECTIVE 5200.20 AND
NO RESTRICTIONS ARE IMPOSED UPON
ITS USE AND DISCLOSURE.

DISTRIBUTION STATEMENT A

APPROVED FOR PUBLIC RELEASE;
DISTRIBUTION UNLIMITED.

2. CONCLUSIONS

Based on results of the numerical calculations, four major conclusions were reached:

- a. A central peak will form in a crater in a solid medium when the rebound of material from maximum compression is sufficient.
- b. The rebound mound must occur in the region of the medium where material yields but the material strength is significant compared to the maximum stresses.
- c. The rebound mound is significantly enhanced by plastic volumetric increases that occur during yielding when material strength is a function of pressure.
- d. The presence of a fluid-like material below a solid layer might also cause the formation of a central peak in a shock-produced crater.

These conclusions form the basis of a model of the mechanics of central peak formation.

Because the observed occurrence and structural relations of central peaks in craters produced by high-explosive, nuclear, and hypervelocity impact events can be explained using the mechanical model, I conclude that this model describes the causes of central mound formation in shock-wave cratering events. These peaks are structures that are controlled primarily by the properties of the cratered medium. The properties of the source of energy for the cratering event influence central mound formation only by modifying the stress distribution in the cratered medium. Shear waves and stress-wave reflections from discontinuous increases in acoustic impedance enhance central mound formation but are not the primary cause. Deep gravitational sliding may occur and increase the inward displacement of material, but this process is an effect rather than a cause of central mound formation.

Also, since the occurrence and structure of a central uplift are controlled by the properties of the cratered medium at the time of the shock-wave cratering event, these structures provide a record of those properties. With the mechanical model as a guide, this record may be useful in examining the evolutionary and spatial relations of the media in which shock-wave cratering events have occurred. Evolutionary models of solar-system bodies can be constrained by the structure of craters observed in spacecraft photography.

Because the processes of the mechanical model are described in the calculational code, that code becomes a tool that can be used to examine occurrences of central peaks. Such an application to larger-scale events with higher maximum pressures and different loading conditions will require extensive modifications to the actual code used during this study. These changes include a more general equation of state, an active inclusion of initial lithostatic stresses, and a different scheme of grid definition. However, the modifications can be made within the present calculational structure of the AFTON-2A code.

3. FUTURE WORK

The results of the MCP-12 numerical experiment indicate that the presence of a "fluid" below a solid crust will significantly change the response of the crust to a shock-wave cratering event. The manner of this change is speculated to eventually result in the development of upward motions in the solid medium. Therefore, the structural relations between the craters Lansberg and Reinhold might be the result of a growing lunar crust. A program to simulate numerically the events which caused these two craters is recommended. While such a simulation could be completely accomplished with the AFTON-2A code, it is recommended that only the early part of the Lansberg calculation be accomplished with that code to develop the velocity distribution in the lower layer. The results of this part would then be used as initial conditions in a code that explicitly and more efficiently treated viscous flow.

Both laboratory and numerical experiments should be accomplished to determine if the momentum and energy density of a hypervelocity impact have any special influence on the general structural characteristics of an impact crater. Since crater size has been related to the energy of the event (Baldwin, 1973), if the influence of momentum could be determined then the mass and velocity of the impacting body could be estimated. If the influence of energy density on crater structure could be determined, then the density of the impacting body could also be determined.

In the yield model used to accomplish the calculations, the assumption that the yield surface was independent of the third invariant of the deviator stresses is not generally valid. The general associated-flow-rule is dependent on the third invariant (Trulio, et al., 1969), and at least one model of the dependence of the yield surface on the third invariant exists (White, 1973). The need for including this addition in the AFTON-2A yield model should be examined further.

Data on occurrence of central peaks should be reviewed for spatial and age relationships. For example, if the lunar craters of 25 miles diameter that had central mounds has similar age characteristics, then conditions favorable to central mound formation would have occurred at the time those craters were formed. Then, if that time varied with crater size, the evolution of those conditions could be examined. Also, Manley, et al., 1973, reported that the distribution of central peaks in the cratered areas on Mars is characterized by clusters and seems nonrandom. They stated that the curve of central peak frequency versus crater diameter has a maximum at a crater diameter of 5 to 7.5 miles and decreases rapidly as the diameter increases. They also reported that large numbers of central peaks occur in craters of 2.5 to 7.5 mile diameters, with 10 percent of those craters having multiple peaks. The physical model of Mars should be examined for special conditions which would favor central mound formation between 1 and 4 miles deep. Similar examinations should also be made of the photographic information on Mercury. Such studies would provide important guides to evolutionary models.

APPENDIX A
COMPUTATION PARAMETERS

The complete set of computation parameters for all the numerical experiments described in the text may be divided into two categories. The first category includes the parameters that were not varied during any of the problems. These parameters are given once in this appendix and apply to all the numerical experiments. The second category includes the parameters that were varied for at least one of the numerical experiments. These parameters are given for the reference calculations and the variations are described for each of the other numerical experiments.

CONSTANT NUMERICAL PARAMETERS

1. Explosive yield - 20 tons TNT
2. Initial time - 0.206 msec
3. Gravitational acceleration - 32.2 ft/sec
4. Artificial viscosity coefficients
 - Bulk linear constant - 0.06
 - Bulk quadratic constant - 4.0
 - Deviatoric quadratic constant - 4.0
 - Deviatoric linear constant - 0.06
5. Calculation grid definition

RADIAL COORDINATES

	<u>Initial (ft)</u>	<u>Number</u>	<u>Initial Spacing (ft)</u>	<u>Growth Rate</u>
First Region	0	21	1.0	1.0
Second Region	20	40	1.2	1.1

VERTICAL COORDINATES

	<u>Initial (ft)</u>	<u>Number</u>	<u>Initial Spacing (ft)</u>	<u>Growth Rate</u>
First Region	0.	4	-0.6	1.0
Second Region	-1.8	22	-0.8	1.0
Third Region	-19.4	16*	-1.13	1.1

*For MCP-12, changed to 27.

6. Initial target point coordinates - 100 locations formed by combination of
 X Coordinate (ft) 0., 2., 4., 6., 8., 10., 14., 18., 22., 26.
 Y Coordinate (ft) -1., -2., -3., -4., -6., -8., -10., -12., -16., -20.

7. Material properties

	<u>Layer 1</u>	<u>Layer 2</u>	<u>Layer 3</u>	<u>Layer 4</u>
Initial density (gm/cc)	1.875	2.35	2.47	2.35
u_3	0.2366	0.051	0.0229	0.051
u_s	0.50	0.30	0.27	0.30
K_m (kbars)	680	680	680	680
Sublimation energy ($\times 10^{12}$ ergs/gm)	0.02	0.02	0.02	0.02
$A(\times 10^{-12}$ gms/erg)	3	3	3	3

8. Problem specifications

MC 2.12

	<u>Layer 1</u>	<u>Layer 2</u>	<u>Layer 3</u>	<u>Layer 4</u>
Depth to top (ft)	0.0	-1.8	-11.4	-19.4
c_L (ft/sec)	500	8000	9000	8000
c_u (ft/sec)	1250	9000	10000	9000
c_v (ft/sec)	500	8000	9000	8000
Poisson's ratio	0.25	0.20	0.25	0.20
t_0 (bars)	0.7	68	51	68
$\tan \phi$	0.466	0.7	0.75	1.0
Y_{MAX} (kbars)	0.5	7.5	2.1	11.6
Tension limit (bars)	0	-68	-68	-68

MC 2.13: MC 2.12 with the changes

	<u>Layer 1</u>	<u>Layer 2</u>	<u>Layer 3</u>	<u>Layer 4</u>
c_u (ft/sec)	1250	11000	12000	11000

MC 2.15: MC 2.12 with no yield surface shift and the changes

	<u>Layer 1</u>	<u>Layer 2</u>	<u>Layer 3</u>	<u>Layer 4</u>
Tension limit (bars)	0	0	0	0

MCP-01: MCP-02 with Layer 2 in the Layer 1 position also

MCP-02

	<u>Layer 1</u>	<u>Layer 2</u>
Depth of top (ft)	0.0	-1.8
c_L (ft/sec)	500	8000
c_u (ft/sec)	1250	8000
c_v (ft/sec)	500	8000
Poisson's ratio	0.25	0.20
t_0 (bars)	0.7	68
$\tan \phi$	0.466	0.7
Y_{MAX} (kbars)	0.5	7.5
Tension limit (bars)	0	-68

MCP-03: MCP-02 with the changes

	<u>Layer 3</u>
Depth to top (ft)	-11.4
Depth to bottom (ft)	-19.4
c_L (ft/sec)	9000
c_u (ft/sec)	9000
c_v (ft/sec)	9000
Poisson's ratio	0.25
t_0 (bars)	51
$\tan \phi$	0.75
Y_{MAX} (kbars)	2.1
Tension limit (bars)	-68

MCP-05: MCP-02 with the Prandtl-Reuss flow rule only

MCP-06: MCP-02 with no yield allowed

MCP-07: MCP-02 with yield surface shifted only before yield calculation

MCP-08: MCP-02 with yield surface shifted only after yield calculation

MCP-09: MC 2.12 with the changes

	<u>Layer 1</u>	<u>Layer 2</u>	<u>Layer 3</u>	<u>Layer 4</u>
c_u (ft/sec)	1250	11000	12000	11000
c_v (ft/sec)	500	4775	6164	4775

MCP-12: MCP-02 with the changes

	<u>Layer 3</u>
Depth to top (ft)	-16.2
c_L (ft/sec)	6000
c_u (ft/sec)	6000
c_v (ft/sec)	6000
Poisson's ratio	0.45
t_0 (bars)	34
$\tan \phi$	0.75
Y_{MAX} (bars)	34
Tension limit (bars)	0

MCP-21: MCP-02 with the change that Y_{MAX} in Layer 2 was 0.21 kbars.

APPENDIX B
THE AFTON-2A CODE

The theory of the AFTON-2A code has been documented in Air Force Weapons Laboratory technical reports (Trulio, 1966; Trulio, et al., 1969; Niles, et al., 1971). Since the work accomplished during this study did not include any modification of that theory, this description is not significantly different from the descriptions provided in those reports. However, in order to provide a more complete document, the description of the theory of the AFTON-2A code by Niles, et al., 1971 will be repeated.

1. FINITE DIFFERENCE MESHES AND ZONES IN AFTON-2A

The finite difference technique used in the AFTON codes is of the "time-marching" kind; that is, the space continuum is replaced by a discrete mesh of points. Starting with a system in a known state at some initial time, the variables of the motion are updated by a discrete time increment at all points of the space mesh, according to the finite difference equations of motion. The updating process is then repeated using the just-calculated values of the variables of the motion as fresh initial value data. Owing to the assumed symmetry of the motion, a space mesh for AFTON-2A need only be defined as an array of points in a single azimuthal plane, the variables of the motion having identical values at corresponding points of all azimuthal planes. The points of an AFTON-2A finite difference mesh are logically equivalent to the corner points of a set of unit squares which cover a rectangular region in one-to-one fashion. The mesh points are therefore the vertices of quadrilaterals which can be produced by the continuous distortion of a rectangular array of unit squares. The region of two-dimensional axisymmetric flow is thus covered by elementary quadrilaterals; these quadrilaterals are the "zones" of the finite difference mesh. Actually, it is basic to the method of differencing which underlies the AFTON codes that real physical systems have finite extension in a direction normal to the symmetry plane in which the quadrilaterals lie. Thus, a quadrilateral zone is just a cross section of a quadrilateral wedge in a single azimuthal plane of symmetry. The quadrilateral wedge, a solid figure, is the basic geometric entity of the AFTON-2A finite difference mesh and is shown schematically in figure B-1. It is a polyhedron bounded by two nearly parallel

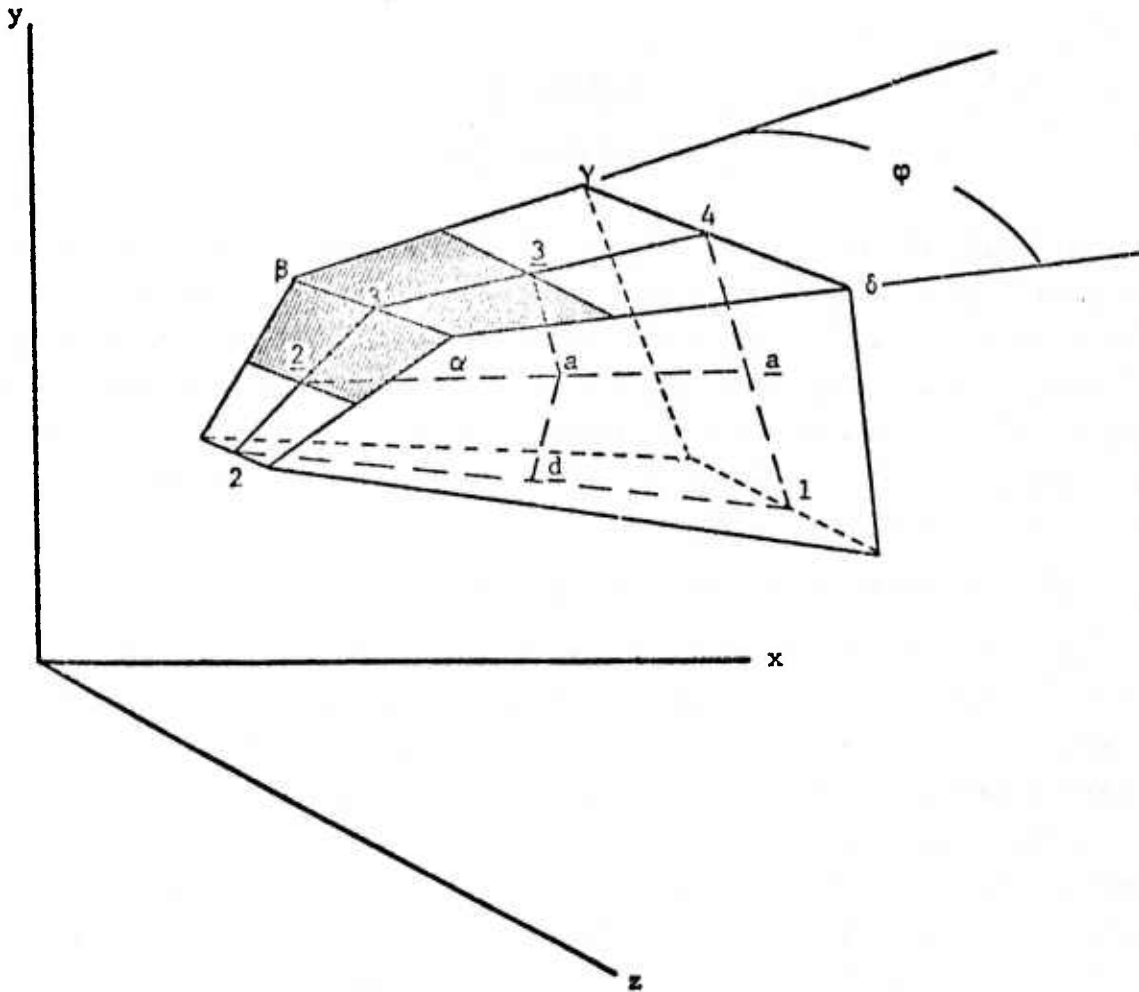


Figure B-1. Quadrilateral Wedge

azimuthal planes with similar quadrilateral cross sections in all azimuthal planes between the two. Four trapezoidal faces normal to the central quadrilateral complete the polyhedron.

The integral equations and associated finite difference equations which are basic to AFTON-2A have been written in sufficient generality to include non-Lagrangian as well as Lagrangian descriptions of continuum motion. The code itself contains a subroutine which defines the coordinate system to be used for any given problem. However, the Lagrangian case will be discussed because the finite difference technique as it applies to AFTON-2A is most simply explained for that case. The points of the finite difference mesh are then mass points whose velocities provide a discrete approximation to the material velocity field of the continuous medium.

In the Lagrangian case each quadrilateral wedge is a finite mass element consisting of the same material particles at one time as at any other time, and a quadrilateral zone--a cross section of a quadrilateral wedge in a symmetry plane--is defined by one specific set of coplanar particles. Motion of the vertices of a quadrilateral wedge therefore produces a distortion or strain in the wedge and causes changes in all the flow variables for a finite element of material.

2. THE CALCULATION OF THERMODYNAMIC VARIABLES IN AFTON-2A FOR LAGRANGIAN MESHES

The variables of the motion are divided into two classes; namely, those associated with the vertices of zones, and those associated with their interiors. The first class (dynamic variables) consists of mesh or grid point positions and their time derivatives (i.e., their velocities) while the second class (thermodynamic variables) includes strain, stress, and internal energy. For the calculation of zone-centered variables two assumptions are made.

- a. A material element which initially occupies the region enclosed by a quadrilateral wedge always has the shape of a quadrilateral wedge, i.e., straight lines of mass points deform to straight lines of mass points.
- b. Zone-centered variables are constant in value throughout a quadrilateral wedge at any given time, and also change at a constant rate during any particular timestep.

With respect to assumption (a), the particles initially comprising a side of a quadrilateral zone will, in general, not remain colinear; likewise, the corresponding face of the quadrilateral wedge associated with the zone usually will not, in physical reality, remain a quadrilateral. Rather, a trapezoidal Lagrangian surface of the quadrilateral wedge will deform into a more general curved shape. Assumption (a), therefore, imposes a nonphysical constraint on the system, which is part of the price paid for replacing the space continuum by a discrete mesh of points. Obviously, assumption (b) entails a similar nonphysical restriction; real physical stresses and strains generally vary continuously over finite distances.

The calculation of the change in the volume of a quadrilateral wedge produced by the motion of the vertices of its associated quadrilateral zone provides the key to the construction of the finite difference equation of AFTON-2A. In making the calculation, the following definitions and conventions are adopted.

- a. V , \underline{R} , \underline{U} , \underline{A} denote volume, position vector, material velocity vector, and vector area, respectively.
- b. The superscripts n and $n-1$ refer to a "later time" t^n , and an "earlier time" t^{n-1} , separated by the interval $\Delta t^{n-1/2} = t^n - t^{n-1}$.
- c. If no superscript is attached to a variable, it is understood to be defined at some time between t^{n-1} and t^n . In particular, the position vector of a point without a superscript is by definition equal to the arithmetic mean of the positions of the point at the two times t^n and t^{n-1} , i.e.,

$$\underline{r} = 1/2 (\underline{r}^n + \underline{r}^{n-1}) \quad (\text{B-1})$$

- d. The particle velocity of a point is related to its position \underline{r}^{n-1} and \underline{r}^n at the times t^{n-1} and t^n according to

$$\underline{u} = \frac{\underline{r}^n - \underline{r}^{n-1}}{\Delta t^{n-1/2}} \quad (\text{B-2})$$

- e. Position and velocity subscripts refer to the mesh points labeled as numbers in figures B-1 and B-2.

The underlined subscripts $\underline{2}$, $\underline{3}$, \underline{a} , and \underline{d} , shown schematically in figure B-2, refer to points on the side of zone "a". The coordinates of point $\underline{2}$, for example, are defined by the equations

$$x_{\underline{2}} = \left(\frac{x_2^2 + x_2 x_3 + x_3^2}{3} \right)^{1/2} \quad (\text{B-3})$$

and

$$y_{\underline{2}} = \frac{(x_3 - x_2) y_2 + (x_2 - x_3) y_3}{x_3 - x_2} \quad (\text{B-4})$$

The coordinates of the points $\underline{3}$, \underline{a} and \underline{d} are found in a similar fashion.

Equation (B-2) involves the kind of discretization error entailed in assumption (b) above; in this case, the velocity is taken to be constant over a finite time interval; namely, Δt . An exact calculation of the volume of a quadrilateral wedge shows that

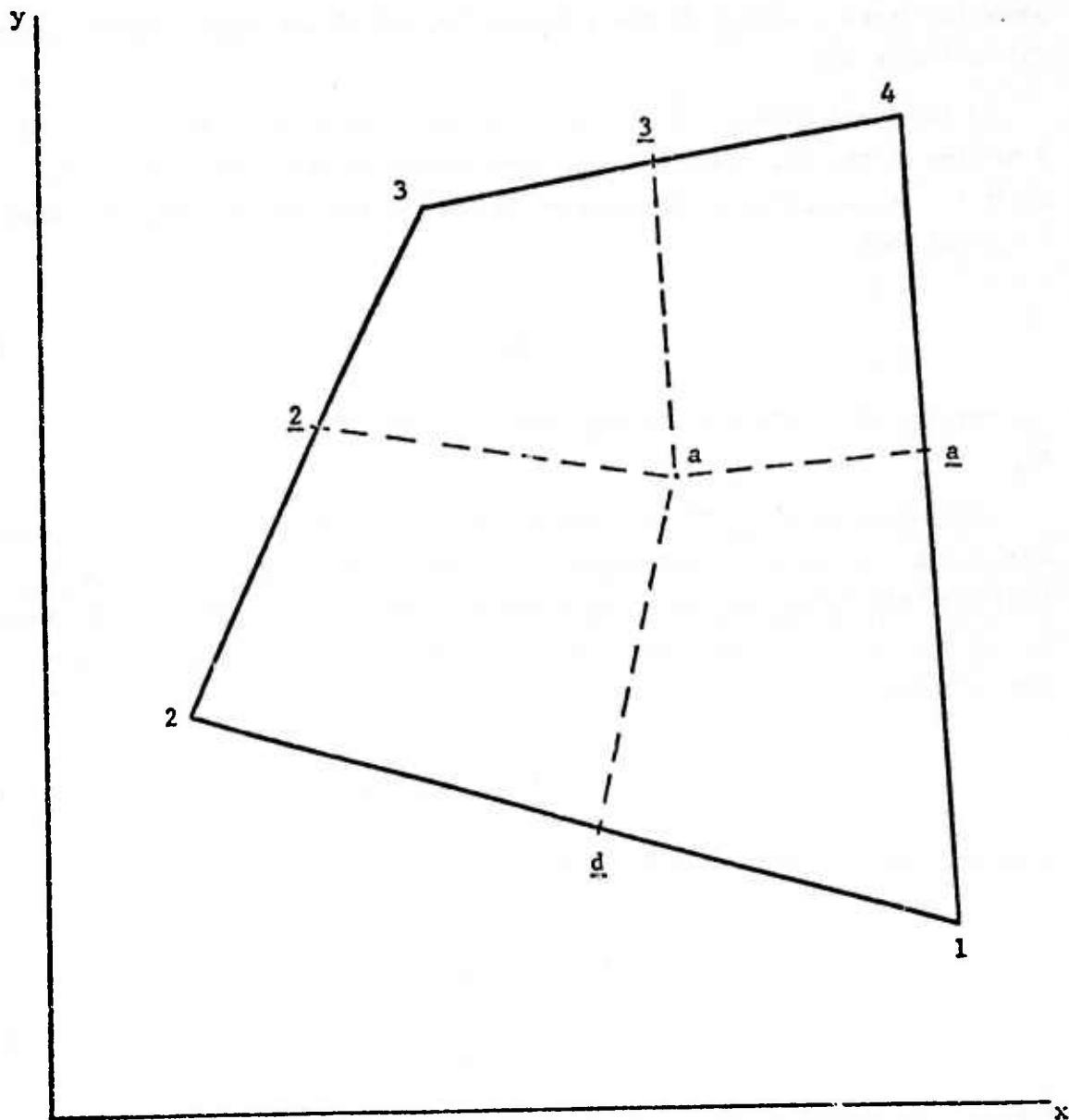


Figure B-2. Projection of the Cross Section of a Quadrilateral Zone in the x-y Plane

$$\frac{v^n - v^{n-1}}{\Delta t^{n-1/2}} = \sum_{i=1}^4 A_i^{n-1/2} \cdot \underline{u}_i^{n-1/2} \quad (B-5)$$

where the index i refers to the vertices 1,2,3,4 of the quadrilateral designated "a" in figure B-2.

In the limit of an infinitesimal timestep, the vector area \underline{A}_i is composed of a portion of the two trapezoidal surfaces whose intersection contains the point i . For example, \underline{A}_3 corresponds to the shaded area in figure B-1 when $i = 3$ and thus

$$\underline{A}_3 = \underline{A}_{23} + \underline{A}_{33} \quad (B-6)$$

\underline{A}_{23} and \underline{A}_{33} are calculated as described below for the general vector area, \underline{A}_{ij} .

The vector area \underline{A}_{ij} is the trapezoidal surface of the quadrilateral wedge between the vertices i, j of figure B-1. The sense of the vector area \underline{A}_{ij} is that of the outer normal to the surface. Thus, for example, if one encounters point $i = 3$, and then the point $j = 4$, as the perimeter of the quadrilateral wedge is traversed clockwise, then

$$\underline{A}_{ij} = \underline{A}_{34} = 1/2 \left[\left(\underline{r}_\beta - \underline{r}_\delta \right) \times \left(\underline{r}_\alpha - \underline{r}_\gamma \right) \right] \quad (B-7)$$

which per angle ϕ can be shown to reduce to

$$\underline{A}_{34} = 1/2 (x_3 + x_4) \begin{bmatrix} y_3 - y_4 \\ x_4 - x_3 \\ 0 \end{bmatrix} \quad (B-8)$$

However, the vector areas \underline{A}_i can be expressed directly in terms of the vertices of quadrilateral "a" as shown below for \underline{A}_3

$$\underline{A}_3 = \begin{bmatrix} A_{3x} \\ A_{3y} \\ 0 \end{bmatrix} = 1/6 \begin{bmatrix} y_2(x_2 + x_3) - y_4(x_3 + x_4) + A_{23} + A_{34} \\ -x_2(x_2 + x_3) + x_4(x_3 + x_4) \\ 0 \end{bmatrix} \quad (B-9)$$

where

$$A_{23}^n = x_2^n y_3^n - x_3^n y_2^n \quad (B-10)$$

Equation (B-5) has the geometric interpretation that the change in the volume of a quadrilateral wedge in a time interval Δt is equal to the algebraic sum of the volumes swept out by the four trapezoidal faces of the wedge normal to the x-y plane, if appropriate portions of each face move with a uniform velocity equal to the velocity of the vertex. The volume change so calculated is exact, regardless of the time interval Δt or of the positions of the vertices of the quadrilateral zone at the beginning and end of the interval.

According to assumption (b), thermodynamic variables such as stresses and internal energies are considered to be properties of quadrilateral wedges as a whole. These variables are updated for general stresses and strains by an extension of a standard numerical hydrodynamic procedure in which a finite difference analog of the First Law is satisfied simultaneously with the constitutive equation for a given medium. In the hydrodynamic case, the change in the internal energy of a quadrilateral wedge is just its volume change given by equation (B-5), multiplied by the negative of the arithmetic mean of the pressures in the wedge at the times t^{n-1} and t^n .

$$E^n - E^{n-1} = -PQ(V^n - V^{n-1}) \quad (B-11)$$

where PQ denotes $(P + Q)^{n-1/2}$. If an equation of state is used to eliminate the new pressure (i.e., the pressure at time t^n) from the finite difference analog of the First Law, then the fact that equations of state generally involve the internal energy renders the First Law analog an implicit equation for the new internal energy.

$$p^n = g(\rho^n, E^n) \quad (B-12)$$

Here g , the equation of state, is some (known) function of two variables, and P , E , ρ denote the pressure, internal energy and density of the quadrilateral wedge, respectively, the mass being constant in the Lagrangian case under discussion. Also, Q is a generalization of the artificial viscosity of von Neumann and Richtmyer (1950). Q is computed explicitly knowing V , while P^n and E^n should be obtained by solving equations (B-11) and (B-12) simultaneously.

In the calculation, it is worth noting that if the pressure in the quadrilateral wedge were indeed uniform and equal to its mean value on the time interval Δt , then the calculation of the change in the internal energy of the wedge as well as its volume change would be exact.

For general axisymmetric two-dimensional motion, the procedure for writing an exact finite difference analog of the First Law is not so obvious as for hydrodynamic motion. In fact, an exact analog of the First Law can be written only for triangular zones and not for more general polygons such as quadrilaterals.

In obtaining a finite difference analog of the First Law for general stress and strain, the change in the volume of the zone, as given in equation (B-5), is of prime importance. Introducing this expression for the volume change into equation (B-11) leads directly to a finite difference analog of the First Law which can be used for any stress, hydrodynamic or otherwise, and which is exact in the hydrodynamic case under assumptions (a) and (b). This combination of equations (B-5) and (B-11) for the zone "a" is

$$E^n - E^{n-1} = \Delta t \sum_{i=1}^4 \underline{U}_i \cdot \underline{F}_i \quad (\text{B-13})$$

where for hydrodynamic motion, the forces $\underline{F}_1, \dots, \underline{F}_4$ in equation (B-13) are given by the equations of the form

$$\underline{F}_1 = (PQ) \left(\underline{A}_{a1} + \underline{A}_{1d} \right) \quad (\text{B-14})$$

To compute the change in internal energy for general stresses, the scalar hydrodynamic stress (PQ) of equation (B-14) is replaced by the stress tensor σ_{ij} . Again, in accord with assumption (b), σ_{ij} is assumed to be constant during a timestep throughout any particular quadrilateral wedge. The definitions of the forces $\underline{F}_1, \dots, \underline{F}_4$ then become

$$\underline{F}_1 = \sigma_{ij} \cdot \left(\underline{A}_{a1} + \underline{A}_{1d} \right) \quad (\text{B-15})$$

etc., where the multiplication called for in equation (B-15) is that of a matrix with a vector.

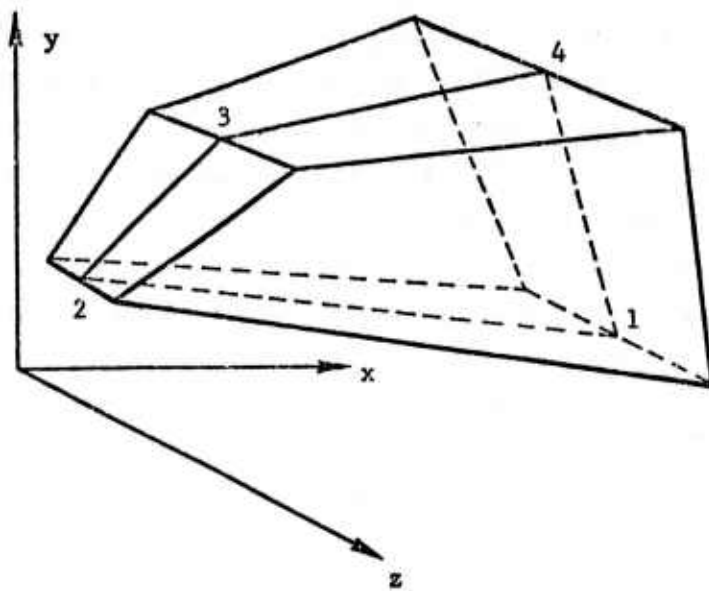
As an expression for the change of internal energy, the right-hand member of equation (B-13) presents one obvious problem: its terms are all defined only on the surface of a material element, whereas "internal" energy is, in fact, a quantity associated in an essential way with the interior of a material region. To transform equation (B-13) so that it involves only interior areas of a quadrilateral wedge, an elementary geometric theorem is used. This theorem, which is a cornerstone of the finite difference method embodied in the AFTON codes, simply states that the sum of the vector areas of any polyhedral surface is zero, where the sense of the vector area associated with each face of the polyhedron is understood to be that of the outer normal to the enclosed volume. The meaning of the theorem can be exhibited in the following geometric way. Viewed from any aspect at a sufficiently great distance, a polyhedron presents a cross section which is at one and the same time the projection of the front side of the polyhedron on a plane normal to the viewer's line of sight, and also of its back side. The area of the cross section is equal in magnitude to the component of the resultant vector area of the plane surfaces making up the front side of the polyhedron, and is also the negative of the corresponding component of the resultant area of the faces of the back side (see figure B-3). Since the faces of the front and back side make up the entire (closed) polyhedral surface, the sum of all the vector areas is plainly zero.

With respect to the calculation of internal energy changes, equation (B-13) can be transformed so that its forces refer only to trapezoidal surfaces in the interior of the quadrilateral wedge plus the wedge faces. The theorem just discussed implies, for example, that the sum of the trapezoidal area \underline{A}_{1d} , \underline{A}_{da} , \underline{A}_{aa} , and \underline{A}_{a1} , plus the sum of the areas of the two azimuthal surfaces of the wedge, \underline{A}_{w1} , is zero. Therefore,

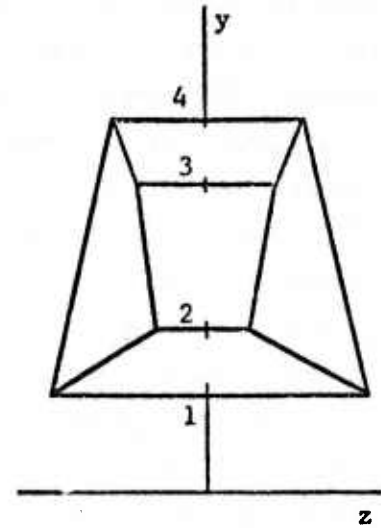
$$\underline{A}_{a1} + \underline{A}_{1d} = -(\underline{A}_{da} + \underline{A}_{aa} + 2\underline{A}_{w1}) \quad (\text{B-16})$$

The vector area, \underline{A}_{w1} , of the quadrilateral cross section or wedge face is defined as follows

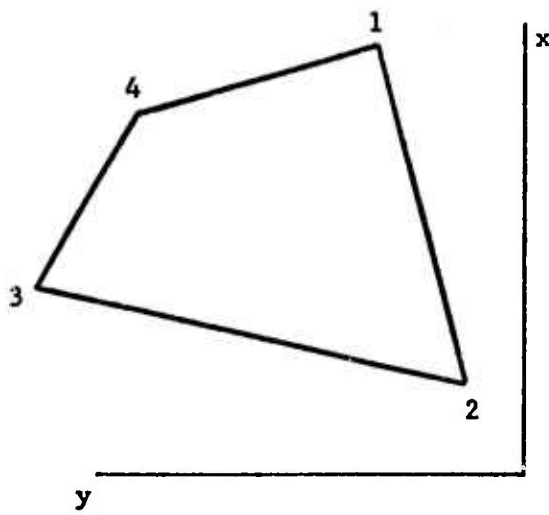
$$\underline{A}_{w1} = 1/2 \left[\left(\underline{r}_d - \underline{r}_a \right) \times \left(\underline{r}_1 - \underline{r}_a \right) \right] \quad (\text{B-17})$$



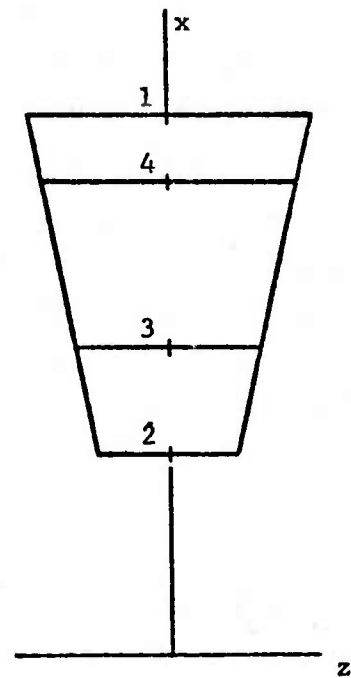
(a)



(b)



(c)



(d)

Figure B-3. Quadrilateral Wedge and Its Projections into the x-y, y-z, and x-z Planes

Thus, equation (B-13) can be written in the form

$$\begin{aligned}
 E^n - E^{n-1} = \Delta t \left[& F_{\underline{aa}}(\underline{U}_1 - \underline{U}_4) + F_{\underline{da}}(\underline{U}_2 - \underline{U}_1) \right. \\
 & + F_{\underline{2a}}(\underline{U}_3 - \underline{U}_2) + F_{\underline{3a}}(\underline{U}_4 - \underline{U}_3) \\
 & \left. + F_{\underline{w1}} \cdot \underline{U}_1 + F_{\underline{w2}} \cdot \underline{U}_2 + F_{\underline{w3}} \cdot \underline{U}_3 + F_{\underline{w4}} \cdot \underline{U}_4 \right] \quad (B-18)
 \end{aligned}$$

Equation (B-18) can be interpreted as a sum of internal energy changes produced by the extension of material in directions normal to the forces exerted on specific interior or wedge face surfaces of the quadrilateral wedge.

3. CALCULATION OF MOMENTUM

In addition to updating the thermodynamic variables of a zone, new velocities and positions of the mesh points also need to be calculated. The procedure used to update velocities is based on the principle of momentum conservation, as applied to a spatial region known as a "momentum zone."

As in the case of velocities and positions, momentum zones are centered at mesh points. The momentum zone associated with a mesh point is comprised of a precisely defined portion of each of the four thermodynamic zones which share the mesh point as a common vertex. A thermodynamic zone is therefore divided into four pieces each of which is associated with one, and only one, vertex for the purpose of the momentum calculation. The division is made by joining an interior point of the zone, called its "mid-point," to certain points of its edges; for example, the point labeled a in figure B-1 is connected to the points a, d, 2 and 3. The trapezoidal surfaces bounded by pairs of points such as (a,a) or (a,2) (shaded in figure B-4) represent a major portion of the interior areas upon which the stresses are imposed. The remaining portion of the area acted upon by stress is subtended by the wedge faces of the zone. The momentum zone contains a mass of material equal to the sum of a precise portion of each of the four thermodynamic zones which have as a common vertex the point about which the momentum zone is centered (i.e., the shaded area in figure B-5). The momentum zone in AFTON-2A is then a polyhedron of ten faces. Forces exerted on the eight trapezoidal faces and two wedge faces of the momentum zone produce an acceleration of the momentum mass. If assumption (b) is true for both the forces acting on the momentum zone and the velocity of the zone during an entire

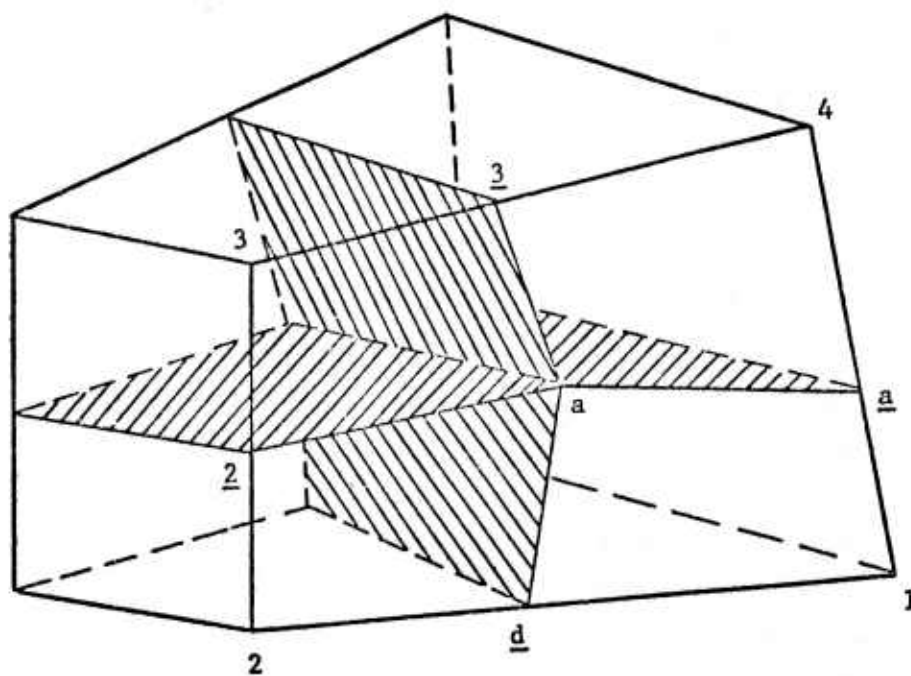


Figure B-4. Interior Areas of a Quadrilateral Wedge

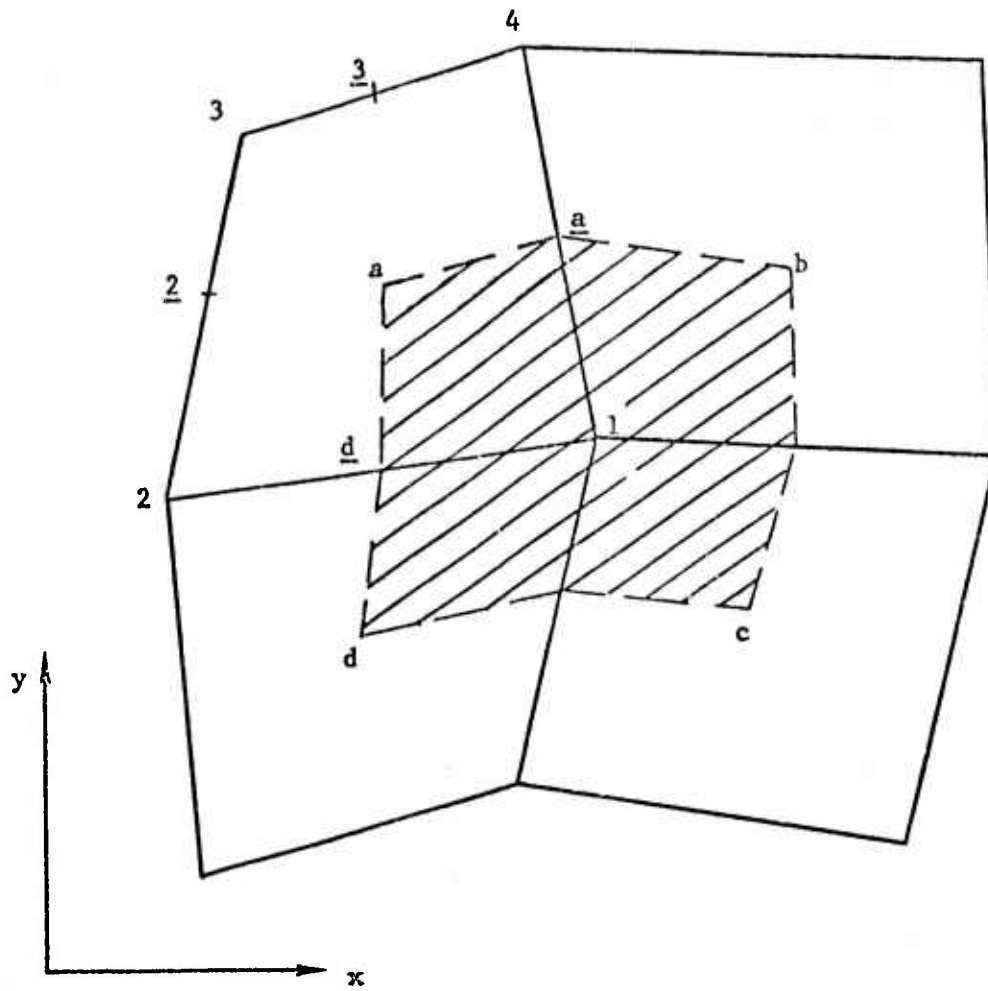


Figure B-5. Momentum Zone Centered at Point 1 Projected Into the x-y Plane; Point 1 is the Vertex Common to the Four Thermodynamic Zones Labeled a, b, c, d

timestep, then the change in momentum during a timestep may be calculated exactly. The momentum \underline{M}^n at time t^n can now be updated from its value at time t^{n-1} . For the momentum zone conservation of momentum is expressed by the equation

$$\underline{M}^n - \underline{M}^{n-1} = \Delta t \left[\underline{F}_{1a} + \underline{F}_{2b} + \underline{F}_{3c} + \underline{F}_{4d} \right] \quad (\text{B-19})$$

In the above expression, the force \underline{F}_{1a} is related to three of the forces which appear in equation (B-18), as follows

$$\underline{F}_{1a} = \underline{F}_{aa} + \underline{F}_{da} + \underline{F}_{w1}$$

or

$$\underline{F}_{1a} = \begin{bmatrix} \sigma_{11} (A_{1x} - a) + \sigma_{12} A_{1y} + \sigma_{33} a \\ \sigma_{12} (A_{1x} - a) + \sigma_{22} A_{1y} \\ 0 \end{bmatrix} \quad (\text{B-20})$$

and similarly for \underline{F}_{2b} , \underline{F}_{3c} and \underline{F}_{4d} . The sense of the forces \underline{F}_{1a} , ..., \underline{F}_{4a} is illustrated in figure B-6. a is the scalar area of the wedge face whose vertices are l , d , a , a . The velocity of the mesh point on which the momentum zone is centered is related to the momentum by the equation

$$\underline{U}^n = \frac{\underline{M}^n}{m} \quad (\text{B-21})$$

where m is the mass of the momentum zone. A forward extrapolation in time is used to advance the velocity from one timestep to the next.

$$\begin{aligned} \underline{U}^{n+1/2} &= 2\underline{U}^n - \underline{U}^{n-1/2} \\ &= \frac{2\underline{M}^n}{m} - \underline{U}^{n-1/2} \end{aligned} \quad (\text{B-22})$$

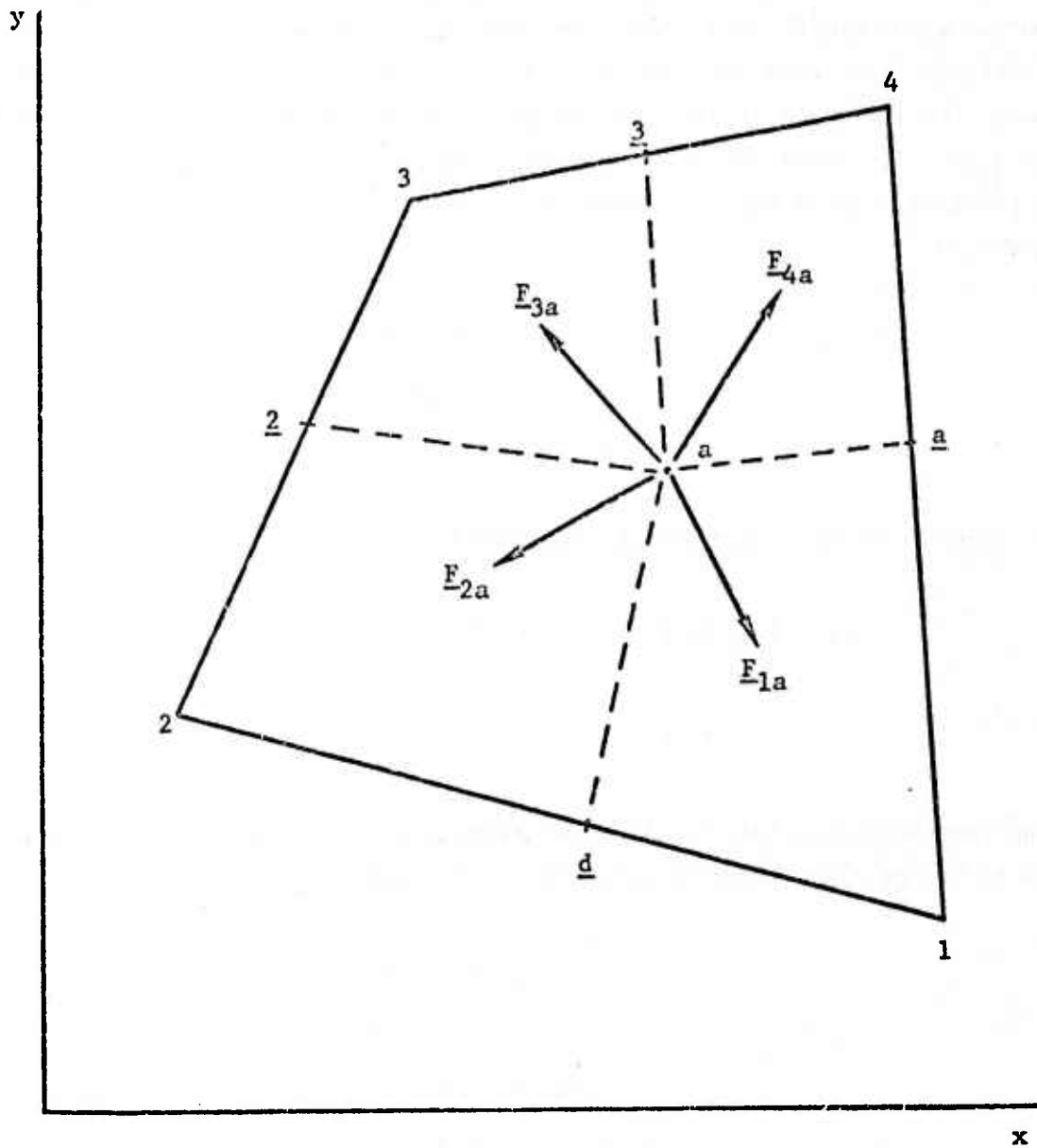


Figure B-6. Illustration of the Sense of the Forces F_{1a} , F_{2a} , F_{3a} , and F_{4a}

4. CALCULATION OF STRAIN

The discussion of the calculation of strain will be initially restricted to considering an axially symmetric wedge (axis of symmetry is the y-axis) whose cross section in the x-y plane is a triangle. The calculation of strain for wedges with quadrilateral cross sections will be treated later. Consider a triangular zone with vertices 1, 2, 3 in its unstrained configuration which, under the influence of external forces, is strained to a new configuration (figure B-7). Then, in axial symmetry, the linear transformation which takes a point (x,y,z) in the unstrained state to the strained state (x', y', z') is given by

$$\begin{aligned}x' &= a_{11} x + a_{12} y \\y' &= a_{21} x + a_{22} y \\z' &= a_{33} z\end{aligned}\tag{B-23}$$

In general for any point (x, y, z), define

$$\begin{aligned}\alpha_i &= (x - x_i) & ; & & \alpha'_i &= (x' - x'_i) \\ \beta_i &= (y - y_i) & ; & & \beta'_i &= (y' - y'_i)\end{aligned}\quad i = 1, 2, 3$$

Now form four equations in the four unknowns a_{11} , a_{12} , a_{21} , a_{22} , which are elements of the point-transformation matrix A' , namely,

$$\begin{aligned}\alpha'_1 &= a_{11} \alpha_1 + a_{12} \beta_1 \\ \alpha'_2 &= a_{11} \alpha_2 + a_{12} \beta_2 \\ \beta'_1 &= a_{21} \alpha_1 + a_{22} \beta_1 \\ \beta'_2 &= a_{21} \alpha_2 + a_{22} \beta_2\end{aligned}\tag{B-24}$$

from which

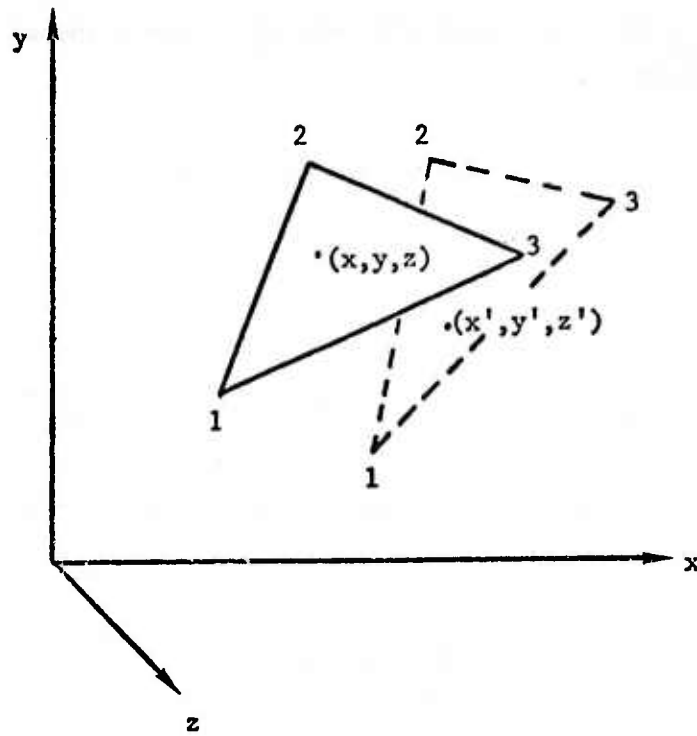


Figure B-7. Schematic of an Unstrained and Strained Triangular Zone

$$a_{11} = \frac{(\alpha'_1\beta_2 - \alpha_2\beta_1)}{A_{\alpha\beta}} \quad ; \quad a_{12} = \frac{(\alpha'_1\alpha_1 - \alpha_2\alpha_2)}{A_{\alpha\beta}}$$

$$a_{21} = \frac{(\beta'_1\beta_2' - \beta_2\beta_1)}{A_{\alpha\beta}} \quad ; \quad a_{22} = \frac{(\alpha_1\beta_2' - \alpha_2\beta_1')}{A_{\alpha\beta}} \quad (B-25)$$

where $A_{\alpha\beta} = \alpha_1\beta_2 - \alpha_2\beta_1$.

Using the elements of the transformation matrix A, a new matrix, T, can be formed

$$T = \begin{bmatrix} a_{11}^2 + a_{12}^2 & a_{11}a_{21} + a_{12}a_{22} \\ a_{11}a_{21} + a_{12}a_{22} & a_{21}^2 + a_{22}^2 \end{bmatrix} = \begin{bmatrix} t_{11} & t_{12} \\ t_{12} & t_{22} \end{bmatrix} \quad (B-26)$$

The eigenvalues λ_1 and λ_2 of T are now related to the principal extensions E_1 and E_2 , as follows:

$$E_1 = \lambda_1^{1/2} \quad ; \quad E_2 = \lambda_2^{1/2} \quad (B-27)$$

where

$$\left. \begin{array}{l} \lambda_1 \\ \lambda_2 \end{array} \right\} = 1/2 \left\{ (t_{11} + t_{12}) \pm \sqrt{(t_{11} - t_{22})^2 + 4t_{12}^2} \right\} \quad (B-28)$$

The third principal extension E_3 is found from the ratio of the strained to unstrained volumes according to the equation

$$\frac{V}{V_0} = E_1 E_2 E_3 \quad (B-29)$$

The three principal strains are related to the extensions by

$$\epsilon_x = E_1 - 1 \quad ; \quad \epsilon_y = E_2 - 1 \quad ; \quad \epsilon_z = E_3 - 1 \quad (B-30)$$

The principal strain axes are found from the eigenvectors of T, namely, $\underline{\Lambda}_1$, $\underline{\Lambda}_2$, where

$$\begin{aligned} \underline{\Lambda}_1 &= \left[(t_{11} - \lambda)^2 + t_{12}^2 \right]^{-1/2} \begin{bmatrix} -t_{12} \\ t_{11} - \lambda \end{bmatrix} \\ \underline{\Lambda}_2 &= \left[(t_{22} - \lambda)^2 + t_{12}^2 \right]^{1/2} \begin{bmatrix} t_{22} - \lambda \\ -t_{12} \end{bmatrix} \end{aligned} \quad (B-31)$$

Of the four possible vectors which can be formed when λ_1 and λ_2 are substituted in the above equations, the two with the largest positive x- and y- components are chosen as the principal strain axes.

For a wedge whose cross section is a quadrilateral, the strain cannot be defined uniquely. The convention used in AFTON to define the strain employs an averaging technique. Each diagonal of the quadrilateral divides it into two triangles. Elements of A-matrices are found for each of the four possible

triangles formed by the two diagonals. Then, the elements of T for the entire quadrilateral are formed by averaging the values of the elements of the A-matrix obtained for each of the four triangles.

5. CALCULATION OF STRESS

Knowing the principal strain axes, defined by the eigenvectors $\underline{\Lambda}_x$ and $\underline{\Lambda}_y$, the principal strains can then be rotated into the laboratory coordinate system. The components of strain in the laboratory coordinate system are then given by the relations

$$\begin{aligned}\epsilon_{xxL}^n &= (\Lambda_{x1}^n)^2 \epsilon_x^n + (\Lambda_{y1}^n)^2 \epsilon_y^n \\ \epsilon_{xyL}^n &= \Lambda_{x1}^n \Lambda_{x2}^n \epsilon_x^n + \Lambda_{y1}^n \Lambda_{y2}^n \epsilon_y^n \\ \epsilon_{yyL}^n &= (\Lambda_{x2}^n)^2 \epsilon_x^n + (\Lambda_{y2}^n)^2 \epsilon_y^n \\ \epsilon_{zzL}^n &= \epsilon_z^n\end{aligned}\tag{B-32}$$

where the subscript L indicates that the strains are Lagrangian, i.e., they are computed at time n for the mass elements that occupied generalized coordinate cells at time n-1. Total strain increments are then formed as follows:

$$\Delta \epsilon_{ij} = \epsilon_{ij}^n - \epsilon_{ij}^{n-1}\tag{B-33}$$

The deviatoric strain increment is calculated from the equation

$$\Delta \epsilon'_{ij} = \Delta \epsilon_{ij} - 1/3 \delta_{ij} \Delta \epsilon_{ii}\tag{B-34}$$

Next, the Lagrangian compression η^n is calculated from the known mass and volume V_L^n of this material element, according to the equation

$$\eta_L^n = \frac{m^{n-1}}{\rho_0 V_L^n}\tag{B-35}$$

The compression increment $\Delta \eta_L = \eta_L^n - \eta_L^{n-1}$, and the excess compression $u_L^n = \eta_L^n - 1$ are then formed. From the equation of state for the Lagrangian mass

element, the new mean stress, P^n , its derivative $K = dP/du$, and the shear modulus, G , are computed. The deviatoric elastic stress tensor and its second invariant are then computed as follows:

$$\left(\sigma_{ij}^{e'}\right)^n = \left(\sigma_{ij}^i\right)^{n-1} - 2G\Delta\epsilon_{ij}^i \quad (B-36)$$

$$J_2^{e'} = 1/2 \sigma_{ij}^{e'} \sigma_{ij}^{e'} \quad (B-37)$$

and a function Y is evaluated according to the expression

$$Y = \min \left\{ \begin{array}{l} \alpha_1 + \alpha_2 \bar{P} + \alpha_3 \bar{P}^2 \\ K \end{array} \right\} \quad (B-38)$$

where α_i and k are constants and \bar{P} is the average mean stress $(P^n + P^{n-1})/2$; the yield surface equation is $J_2^{e'} = Y^2$. If $J_2^{e'} \leq Y^2$, then

$$\sigma_{ij}^{i'n} = \sigma_{ij}^{e'} \quad (B-39)$$

However, if $J_2^{e'} > Y^2$, then the incremental mean and deviatoric stresses are formed according to the incremental plastic stress-strain equations;

$$\Delta P = \frac{K\Delta u - K \left(\frac{dY}{dP}\right) \sigma_{ij}^i \cdot \frac{\Delta\epsilon_{ij}^i}{Y}}{1 + \left(\frac{dY}{dP}\right)^2 \frac{K}{G}} \quad (B-40)$$

$$\Delta\sigma_{ij}^i = G \left[2\Delta\epsilon_{ij}^i - \frac{\sigma_{ij}^i (\sigma_{ij}^i \Delta\epsilon_{ij}^i)}{2 J_2^i} \right] - \sigma_{ij}^i \frac{\left(\frac{dY}{dP}\right) \Delta P}{Y} \quad (B-41)$$

The deviatoric stress is then computed as follows:

$$\sigma_{ij}^{i'n} = \sigma_{ij}^{i'n-1} + \Delta\sigma_{ij}^i \quad (B-42)$$

The calculation of the updated components of Lagrangian stress is completed using the equation

$$\sigma_{ij_L}^n = \delta_{ij} p^n + \sigma_{ij}^n \quad (\text{B-43})$$

APPENDIX C

AUXILIARY COMPUTATION ROUTINES

In addition to the AFTON-2A code, three computer programs were important to the results and displays contained in this document. The first was the ballistic extension model used to extend the calculated velocity conditions at 16.4 msec in the MIXED COMPANY II simulation to the final grid position at 616.4 msec. The second was a flow-field-parameter display program that used the restart dump tapes to construct spatial displays at a particular simulated time. The final program was the time-history display program which used the target-point data tapes to construct the time histories. This third program involved only data handling and simple manipulations and will not be described. However, the first two programs included calculational procedures that are important to their use.

1. BALLISTIC EXTENSION ROUTINE

The ballistic extension model had to describe what grid points were moving, how that motion changed position and velocity values during one time increment, and what grid points stopped moving during the time increment. The major assumptions of the routine were (1) that all motion occurred under the influence of gravity only, and (2) that only large displacements were of interest.

A parameter, S_t , was used at each grid point to differentiate between moving and stopped grid points. For moving grid points the value of this parameter was zero, and for stationary grid points, S_t was set to one. At the beginning of the ballistic extension to MC 2.12 the grid points above 20 feet depth and within a 35-foot range from the vertical axis were considered moving, while all other grid points were considered stopped. This region was defined because of the primary interest in the crater region and because the velocity conditions outside that region, except in the soil layer, would result in calculated displacements of less than 1 inch under ballistic conditions.

The motion of each grid point inside that region was calculated at time increments, Δt , of 2 milliseconds until three conditions were simultaneously satisfied. The first condition was that at least one of the grid points which were originally either immediately below or radially away from the grid point

being considered had stopped. This condition was met if the value of S_t at either of those neighboring grid points was one. The second condition was that the vertical velocity component, calculated during the previous time increment, was not positive. The third condition was that the material density in the lower, outward quarter volume associated with the grid point was at least 1.5 gm/cc. This density was determined by dividing the mass in that quarter zone, which was constant because of Lagrangian motion, by the volume of the quarter zone calculated, using the volumetric subroutine of AFTON-2A, at the beginning of the time increment. If all three of these conditions were met, the value of S_t at the zone being considered was set to one.

The motion of each grid point was then calculated based on the value of S_t . If the value of S_t at the grid point was one, both the horizontal and vertical velocity components were set to zero and the position coordinates of the grid point remained constant. If the value of S_t at the grid point was zero, then the horizontal velocity component, U_x , remained constant and the vertical velocity component U_y^I , at the end of the time increment was determined by

$$U_y^I = U_y^0 - g\Delta t \quad (C-1)$$

where U_y^0 is the vertical velocity component at the beginning of the time increment and g is the gravitational acceleration. The position coordinates of the grid point (X^1, Y^1) at the end of the time increment were then

$$\begin{aligned} X^1 &= X^0 + U_x \Delta t \\ Y^1 &= Y^0 + \Delta t \left[U_y^0 - \frac{g}{2} \Delta t \right] \end{aligned} \quad (C-2)$$

where (X^0, Y^0) are the position coordinates at the beginning of the time increment.

2. FLOW FIELD DISPLAY ROUTINES

The calculation space displays were used to display calculated motion and thermodynamic parameters at appropriate positions. These values, except for the maximum pressure contour plot, were for a particular moment of simulated time and were represented by vector arrows that began at the calculational position, indicated the vector direction, and had lengths scaled to the

magnitude of the value. A vector would not be drawn, however, if (1) the calculational position was outside the display field, (2) the display length of the vector was less than a minimum value, or (3) the length of the vector would cause it to extend beyond the display borders. Minimum length vectors were 0.01 inch on the velocity vector plots and 0.03 inch on the acceleration, principal stress, and calculation grid plots. The displays that required significant data manipulation were the plots of acceleration vectors, principal stress axes, and maximum pressure contours.

The acceleration vectors and principal stress vectors were represented by arrows with lengths proportional to the square root of magnitude but were constructed to maintain the exact vector direction. The second condition required that

$$\frac{l_x}{l_y} = \frac{A_x}{A_y} \quad (C-3)$$

where l_x and l_y are the x and y components of the display vector, and A_x and A_y are the linearly scaled components of the quantity to be represented. The first condition is satisfied if

$$l_x^2 + l_y^2 = (A_x^2 + A_y^2)^{1/2} \quad (C-4)$$

Solving these two relations for l_y implied

$$l_y = \pm \left[(A_x^2 + A_y^2)^{1/2} / \left(1 + \frac{A_x^2}{A_y^2} \right) \right]^{1/2} \quad (C-5)$$

where the sign for l_y was chosen to be the same as A_y . The value of l_x was then determined from relation (C-3). However, this scheme would not work on a computer if A_y was near zero. Since the Calcomp hardware will not plot distances less than 0.01 inch, an alternate scheme was used when A_y was less than 0.0001. The alternate scheme set l_y equal zero and set

$$l_x = \pm (|A_x|)^{1/2} \quad (C-6)$$

where the sign of l_x was chosen to be the same as A_x .

The acceleration vector was determined from the velocity and timestep information in the restart dumps. The AFTON-2A code retains velocity components (U_x^n, U_y^n) at a simulated time and velocity components ($U_x^{n+1/2}, U_y^{n+1/2}$) extrapolated one-half timestep ahead. The acceleration components (a_x, a_y) were determined by

$$\begin{aligned} a_x &= 2 \left(U_x^{n+1/2} - U_x^n \right) / \Delta t^n \\ a_y &= 2 \left(U_y^{n+1/2} - U_y^n \right) / \Delta t^n \end{aligned} \quad (C-7)$$

where Δt^n is the timestep.

The calculation of principal stresses and principal stress direction was based on the Mohr circle construction. The maximum and minimum principal stresses were found by

$$\begin{aligned} \sigma_1 &= 0.5 \left(\sigma_{xx} + \sigma_{yy} \right) + R \\ \sigma_2 &= 0.5 \left(\sigma_{xx} + \sigma_{yy} \right) - R \end{aligned} \quad (C-8)$$

where $R = \left[0.25 (\sigma_{xx} - \sigma_{yy})^2 + \sigma_{xy}^2 \right]^{1/2}$ and σ_{xx} , σ_{yy} , and σ_{xy} represent the radial, vertical, and shear stresses from the restart dump. The maximum principal stress was considered to be in the x principal axis direction unless σ_{yy} was greater than σ_{xx} . The angle of rotation, θ , of the principal axes from the page coordinates was

$$\theta = 0.5 \tan^{-1} \left(\frac{2\sigma_{xy}}{|\sigma_{xx} - \sigma_{yy}|} \right) \quad (C-9)$$

unless $|\sigma_{xy}| > 100 \cdot |\sigma_{xx} - \sigma_{yy}|$ in which case $\theta = \pm 45^\circ$ with the sign chosen the same as σ_{xy} . A positive θ would rotate the principal stress axes from the page axes in a clockwise manner. This scheme was used unless the stress values indicated the material had separated at the thermodynamic point being considered, in which case an X was centered at the point.

A maximum pressure contour plot involved first locating the original position of the thermodynamic grid point and then determining the maximum pressure experienced by that point. The original position of the grid point was determined by first subtracting the displacements of the four surrounding mesh points from their positions at the time of the restart dump to determine the original grid positions. Then the excess compression value was equated to the maximum excess compression value of the thermodynamic point being considered and the AFTON-2A equation-of-state routine was used to determine the maximum pressure value. These values were then contoured with the use of a contour mapping subroutine which was provided by the computer support division of the Air Force Cambridge Research Laboratories.

BIBLIOGRAPHY

- Aherns, T. J.; Rosenberg, J. T.; "Shock Metamorphism: Experiments on Quartz and Plagioclase," Shock Metamorphism of Natural Materials, French and Short, Eds., Mono Book Corp., Baltimore, MD, pp. 59-82, 1968.
- Amsden, A. A.; Particle-in-Cell Method for the Calculation of the Dynamics of Compressible Fluids, LA-3466, LASL, Los Alamos, NM, 1966.
- Baldwin, R. B.; The Measure of the Moon, Univ. Chicago Press, Chicago, IL, 1963.
- Beals, C. S.; "The Identification of Ancient Craters," Ann. New York Acad. Sci., Vol. 123, Article 2, pp. 904-914, 1965.
- Boon, J. D.; Albritton, C. C., Jr.; "Meteorite Scars in Ancient Rocks," Field and Lab., 5, No. 2, pp. 53-64, 1937.
- Bratton, J. L.; "MIDDLE GUST-MIXED COMPANY Comparisons," Proc. MIXED COMPANY/MIDDLE GUST Results Meeting, Vol. II, G. E. Co., TEMPO (DASIAC), pp. 268-295, 1973.
- Carnes, B. L.; "MIXED COMPANY Event, LN301, Crater and Ejecta Studies-Preliminary Report," Proc. MIXED COMPANY/MIDDLE GUST Results Meeting, Vol. II, G. E. Co., TEMPO (DASIAC), pp. 63-78, 1973a.
- Chromokos, J.; Kelso, J. R.; "Operation MIXED COMPANY," Proc. MIXED COMPANY/MIDDLE GUST Results Meeting, Vol. I, G. E. Co., TEMPO (DASIAC), pp. 74-96, 1973.
- Christensen, D. M.; Godfrey, C. S.; Maxwell, D. E., Calculations and Model Experiments to Predict Crater Dimensions and Free Field Motion, PIFR-072, DASA-2360, Phys. Int. Co., San Leandro, CA 94577, 1968.
- Christensen, D. M.; ELK 40: Prediction Calculation of Ground Motion for DISTANT PLAIN, Event 6, DASA-2471, Phys. Int. Co., San Leandro, CA, 1970.
- Circeo, L. J.; Nordyke, N. D.; Nuclear Cratering Experience at the Pacific Proving Grounds, UCRL-12172, Univ. California, Livermore, CA, 1964.
- Cooper, H. F.; On the Application of Finite Difference Methods to Study Wave Propagation in Geologic Materials, AFWL-TR-70-171, AFWL, Kirtland, AFB, 1971.
- Davis, S. E.; "Experimental Data from MIDDLE GUST and MIXED COMPANY CIST Events," Proc. MIXED COMPANY/MIDDLE GUST Results Meeting, Vol. II, G. E. Co. TEMPO (DASIAC), pp. 439-457, 1973.
- Day, J. D.; "Ground Motion Measurements - MIXED COMPANY Calibration Events," Proc. MIXED COMPANY/MIDDLE GUST Results Meeting, Vol. II, G. E. Co., TEMPO (DASIAC), pp. 148-165, 1973.

BIBLIOGRAPHY (Continued)

- Dence, M. R.; "Shock Zoning at Canadian Craters: Petrography and Structural Implications," Shock Metamorphism of Natural Materials, French and Short, Eds., Mono Book Corp., Baltimore, MD, pp. 169-184, 1968.
- Dence, M. R.; Innes, M. J. S.; Robertson, P. B.; "Recent Geological and Geophysical Studies of Canadian Craters," Shock Metamorphism of Natural Materials, French and Short, Eds., Mono Book Corp., Baltimore, MD, pp. 339-362, 1968.
- Dent, B., "The Formation of Central Uplifts in Large Impact Craters," extract from Ph D. dissertation, Dept. Geophys., Stanford Univ. Stanford, CA, 1974.
- Dietz, R. S.; "Shatter Cones in Cryptoexplosion Structures," Shock Metamorphism of Natural Materials, French and Short, Eds. Mono Book Corp., Baltimore, MD, pp. 267-284, 1968.
- Eggleton, R. E.; Geologic Map of the Rhipaeus Mountains Region of the Moon, I-458, U.S. Geol. Surv., Wash., D.C., 1965.
- Ehrgott, J. Q.; "Preshot Material Property Investigation for the MIXED COMPANY Site: Summary of Subsurface Exploration and Laboratory Test Results," Proc. MIXED COMPANY/MIDDLE GUST Results Meeting, Vol. II, G. E. Co., TEMPO (DASIAC), pp. 491-539, 1973.
- Gault, D. E.; Quaide, W. L; Overbeck, V. R.; "Impact Cratering Mechanics and Structures," Shock Metamorphism of Natural Materials, French and Short, Eds., Mono Book Corp., Baltimore, MD, pp. 87-100, 1968.
- Harlow, F. H.; Shannon, J. P.; "The Splash of a Liquid Drop," J. Appl. Phys., 38, pp. 3855-3866, 1967.
- Hartmann, W. K.; "Interplanet Variations in Scale of Crater Morphology - Earth, Mars, Moon," Icarus, 17, pp. 707-713, 1972.
- Hartmann, W. K.; "Martian Cratering, 4, Mariner 9 Initial Analysis of Cratering Chronology," J. Geophys. Rsch., 78, pp. 4906-4116, 1973.
- Howard, K. A.; Offield, T. W., Wilshire, H. G., "Structure of Sierra Madera Texas as a Guide to Central Peaks of Lunar Craters," Geol. Soc. Am. Bull. 83, pp. 2795-2808, 1972.
- Ialongo, G., "MIXED COMPANY III Prediction Calculation," Proc. MIXED COMPANY/MIDDLE GUST Results Meeting, Vol. II, G. E. Co., TEMPO (DASIAC), pp. 669-694, 1973
- Jones, A. H., et al.; Material Properties Measurements for Selected Materials, NAS 2-3427 Interim Report, General Motors Mat./Struc. Lab., Warren, MI, 48090, 1968.

BIBLIOGRAPHY (Continued)

- McConnell, R. K., Jr.; Gast, P. W.; "Lunar Thermal History Revisited," Moon, 5, pp. 41-51, 1972.
- Manley, W. D.; Schultz, P. H.; Ingerson, E.; "Central Peaks of Martian and Lunar Craters: A Comparison," (Abstract-P 15), EOS, 54, No. 11, p. 1127, 1973.
- Maxwell, D.; Moises, H.; Prediction Calculations of MINE UNDER and MINE ORE, DASA-2526, Phys. Int. Co., San Leandro, CA, 94577, 1971a.
- Maxwell, D.; Moises, H.; Hypervelocity Impact Cratering Calculations, PIFR-190, Phys. Int. Co., San Leandro, CA, 94577, 1971b.
- Meyers, J.; "MIDDLE GUST Crater and Ejecta Studies," Proc. MIXED COMPANY/MIDDLE GUST Results Meeting, Vol. II, G. E. Co., TEMPO (DASIAC), pp. 29-49, 1973.
- Milton, D. J.; Roddy, D. J.; "Displacements within Impact Craters," Proc. Int. Geol. Cong. 24th Ses. Sec. 15, pp. 119-124, 1972.
- Milton, D. J., et al.; "Gosses Bluff Impact Structure, Australia," Sci. 175, No. 4027, pp. 1199-1207, 1972.
- Muskat, M., Meres, W. M.; "Reflection and Transmission Coefficients for Plane Waves in Elastic Media," Geophys. 5, pp. 115-148, 1940.
- Murray, B. C., et al.; "Mariner 10 Pictures of Mercury: First Results," Sci. 184, pp. 459-461, 1974.
- Niles, W. J.; Germroth, J. J.; Schuster, S. H.; Numerical Studies of AFTON-2A Code Development and Applications, Vol. II, AFWL-TR-70-22, AFWL, Kirtland AFB, NM, 1971.
- Pike, R. J.; "Genetic Implications of the Shapes of Martian and Lunar Craters," Icarus, 15, pp. 384-395, 1971.
- Port, R. J.; Gajewski, R.; "Sensitivity of Uniaxial Stress - Strain Relations - on Calculations of MIDDLE GUST Event III," Proc. MIXED COMPANY/MIDDLE GUST Results Meeting, Vol. II, G. E. Co., TEMPO (DASIAC), pp. 540-568, 1973.
- REVROC Calculations, Air Force Weapons Laboratory, (unpublished report) Kirtland AFB, NM, 1973.
- Roddy, D. J.; "The Flynn Creek Crater, Tennessee," Shock Metamorphism of Natural Materials, French and Short, Eds., Mono Book Corp., Baltimore, MD, pp. 291-322, 1968.
- Roddy, D. J.; "Comet Impact and Formation of Flynn Creek and Other Craters with Central Peaks," Am. Geophys. Union Trans., 49, No. 1, p. 272, 1968b.

BIBLIOGRAPHY (Continued)

- Roddy, D. J.; "Geologic Studies of the MIDDLE GUST and MIXED COMPANY Craters," Proc. MIXED COMPANY/MIDDLE GUST Results Meeting, Vol. II, G. E. Co., TEMPO (DASIAC), pp. 79-128, 1973.
- Schmitt, H. H.; Trask, N. J.; Shoemaker, E. M.; Geologic Map of the Copernicus Quadrangle of the Moon, I-515, U. S. Geol. Surv., Wash., D. C., 1967.
- Shoemaker, E. M.; "Interpretation of Lunar Craters," Physics and Astronomy of the Moon, Kopal, Ed., Academic Press, pp. 283-359, 1961.
- Shoemaker, E. M.; "Impact Mechanics at Meteor Crater, Arizona," The Solar System, Vol. 4, The Moon, Meteorites, and Comets, Middlehurst and Kuiper, Eds., Univ. Chicago Press, Chicago, IL, pp. 301-336, 1963.
- Short, N. M.; "A Comparison of Features Characteristic of Nuclear Explosion Craters and Astroblemes," Ann. New York Acad. Sci., 123, pp. 573-616, 1965.
- Simmons, G.; Todd, T.; Wang, H.; "The 25-km Discontinuity: Implications for Lunar History," Sci. 182, pp. 158-161, 1973.
- Stearns, R. G., et al., "The Wells Creek Structure, Tennessee," Shock Metamorphism of Natural Materials, French and Short, Eds. Mono Book Corp., Baltimore, MD, pp. 323-338, 1968.
- Toksöz, M. N., et al.; "Thermal Evolution of the Moon," Moon, 4, pp. 190-213, 1972.
- Trulio, J. G.; Methods in Computational Physics, Vol. III, Chapter 3, Academic Press, New York, 1964.
- Trulio, J. G.; Theory and Structure of the AFTON Codes, AFWL-TR-66-19, AFWL, Kirtland, AFB, NM, 1966.
- Trulio, J. G., et al.; Study of Numerical Solution Errors in One- and Two-Dimensional Finite Difference Calculations of Ground Motion, AFWL-TR-67-27, Vol. I, AFWL, Kirtland AFB, NM, 1967.
- Trulio, J. G., et al.; "Ground Motion Studies and AFTON Code Development," Numerical Ground Motion Studies, Vol. III, AFWL-TR-67-27, AFWL, Kirtland AFB, NM, 1969.
- Trulio, J. G.; Perl, N. K.; "Limitations of Present Computational Models of Explosive Induced Ground Motion: MIDDLE GUST Event 3," Proc. MIXED COMPANY/MIDDLE GUST Results Meeting, Vol. II, G. E. Co., TEMPO (DASIAC), pp. 568-619, 1973.
- Von Neumann, J.; Richtmeyer, R. D.; "A Method for the Numerical Calculation of Hydrodynamic Shocks," J. Appl. Phys. 21, pp. 232-237, 1950.

BIBLIOGRAPHY (Continued)

- White, J. W.; "An Invariant Description of Failure for an Isotropic Medium," J. Geophys. Rsch., 78, pp. 2438-2441, 1973.
- Windham, J. E.; Knott, R. A.; Zelasko, J. S.; "Geologic and Material Comparisons for the MIDDLE GUST Test Sites," Proc. MIXED COMPANY/MIDDLE GUST Results Meeting, Vol. II, G. E. Co., TEMPO (DASIAC), pp. 458-491, 1973.
- Wright, J. P.; Sandler, I. S.; Baron, M. L: "Ground Motion Calculations for Events II and III of the MIDDLE GUST Series," Proc. MIXED COMPANY/MIDDLE GUST Results Meeting, Vol. II, G. E. Co. TEMPO (DASIAC), pp. 620-645, 1973.
- Zelasko, J. S.; Baladi, G. Y.; Free Field Code Predictions versus Field Measurements: A Comparative Analysis for the PRAIRIE FLAT EVENT, Misc. Paper S-71-6, U.S. Army Corps. of Eng. Waterways Experiment Station, Vicksburg, MS, 1971.

DISTRIBUTION LIST

DEPARTMENT OF DEFENSE

Assistant to the Secretary of Defense
ATTN: Honorable Donald R. Cotter

Defense Documentation Center
2 cy ATTN: TC

Director of Defense Research & Engineering
ATTN: Asst. Dir., Strat. Wpns.

Director
Defense Intelligence Agency
ATTN: Lieutenant Colonel Paul Cavanaugh
ATTN: DIAAP-8B
ATTN: DIAST-3

Director
Defense Nuclear Agency
ATTN: STSI
2 cy ATTN: STTL
2 cy ATTN: SPSS

Commander
Field Command
Defense Nuclear Agency
ATTN: FCTMO

Director
Defense Advanced Research Projects Agency
ATTN: Lieutenant Colonel George Bulin
ATTN: Director

Director
Weapons Systems Evaluation Group
ATTN: Doc. Con.

DEPARTMENT OF THE ARMY

Commander
Harry Diamond Laboratories
ATTN: Library

Director
U. S. Army Engineer Waterways Experiment Station
ATTN: WESRL
ATTN: WESSS
ATTN: Dr. J. Zelasko
ATTN: Dr. J. G. Jackson, Jr.
ATTN: Mr. Don Day
ATTN: Mr. Leo Ingram
ATTN: Mr. Paul Hadala
ATTN: Mr. G. Baladi
ATTN: Tech. Lib.

Commander
U. S. Army Safeguard Svs. Comd. Fld. Ofc.
ATTN: AMCPM-NXE-FB

Dept. Army Ohio River Div. Lab.
Corps of Engineers
ATTN: ORDLBVR

Dept. of the Army
Office, Chief of Engineers
ATTN: Chief of Eng., ENGMC-EM

DEPARTMENT OF THE NAVY

Officer-in-Charge
Civil Engineering Laboratory
ATTN: Mr. Jay Algood

Chief of Naval Operations

Chief of Naval Research
ATTN: Code 418

Commander
Naval Surface Weapons Center
ATTN: Code 730

Director
Naval Research Laboratory
ATTN: Code 2027

Commander
Naval Weapons Center
ATTN: Code 753

DEPARTMENT OF THE AIR FORCE

ADC/DO
ATTN: DOA

AF Cambridge Research Laboratories, AFSC
ATTN: Dr. Tom Rooney
ATTN: Lt Mark Settle

Commandant
AF Institute of Technology, AFSC
ATTN: Tech. Lib., Bldg. 640, Area B
ATTN: DAPD

Commander
Air Force Logistics Command
ATTN: DEE

AF Materials Laboratory, AFSC
ATTN: Tech. Lib.

Headquarters
Air Force Systems Command
ATTN: DLSP

AF Weapons Laboratory, AFSC
ATTN: IIO, Dr. Minge
ATTN: DE
ATTN: Capt W. Ullrich
2 cy ATTN: SUL
10 cy ATTN: DEV

Commander
Air University
ATTN: AUL, LDE
ATTN: ED, Dir., Civ. Eng.

HQ USAF/RD
ATTN: RDQPN, 1D425
ATTN: RDQ 5

Commander
Rome Air Development Center, AFSC
ATTN: Doc. Lib.

DEPARTMENT OF THE AIR FORCE (Continued)

SAMSO/DE
ATTN: DEN, Maj D. Gage

SAMSO/MN
ATTN: MNH, Capt John Kaiser

USAF Academy
ATTN: DFSLB
ATTN: DFCE
ATTN: FJSRL, CC

ENERGY RESEARCH & DEVELOPMENT ADMINISTRATION

Sandia Laboratories
Livermore Laboratory

Sandia Laboratories
ATTN: Info. Dist. Division
ATTN: Dr. M. L. Merritt
ATTN: Mr. Carter Broyles
ATTN: Mr. Walt Herrman
ATTN: Mr. Wendel Weart
ATTN: Mr. Al Chabai

Los Alamos Scientific Laboratory
ATTN: Report Library

Q-51, Los Alamos Scientific Laboratory
University of California
ATTN: Thomas R. McGetchin

University of California
Lawrence Berkeley Laboratory
ATTN: Library

University of California
Lawrence Livermore Laboratory
ATTN: Barbara Germaine
ATTN: Mr. Robert Schock

OTHER GOVERNMENT AGENCIES

NASA
Ames Research Center
ATTN: N245-5, Dr. Verne Oberbeck
ATTN: N245-11, Dr. Donald E. Gault

Center of Astrogeology
U. S. Geological Survey
ATTN: R. E. Eggleton
ATTN: H. Masursky
ATTN: J. F. McCauley
ATTN: D. H. Scott
ATTN: E. M. Shoemaker
ATTN: L. A. Soderblom
ATTN: G. A. Swann
3 cy ATTN: D. J. Roddy

Department of the Interior
U. S. Geological Survey
ATTN: Daniel J. Milton
ATTN: Richard J. Pike, Jr.
ATTN: Don E. Wilhelms
ATTN: Howard G. Wilshire
ATTN: Cecil B. Raleigh, Earthquake Res. Center
ATTN: John H. Healy

OTHER GOVERNMENT AGENCIES (Continued)

Department of the Interior
Bureau of Mines
ATTN: Dr. Leonard A. Obert

Bureau of Mines
Twin Cities Research Center
ATTN: Dr. T. C. Atchison

U. S. Geological Survey
ATTN: Edward C. T. Chao

DEPARTMENT OF DEFENSE CONTRACTORS

Aerospace Corporation
ATTN: Dr. Prem Mather

Aerospace Corporation
ATTN: Mr. Warren Pfefferle
ATTN: Dr. Mason B. Watson

Agbabian Associates
ATTN: Dr. Mike Agbabian

Applied Theory, Inc.
ATTN: Dr. J. Trulio
ATTN: Neil Pearl

The Boeing Company
ATTN: Mr. Ron Carlson

Brown Engineering Company, Inc.
ATTN: Manu Patel

California Institute of Technology
ATTN: Dr. Thomas J. Ahrens
ATTN: Dr. Leon T. Silver

California Research & Technology, Inc.
ATTN: M. Rosenblatt

Civil/Nuclear Systems Corporation
ATTN: Dr. Robert Crawford

IIT Research Institute
ATTN: Tech Library

Institute for Defense Analyses
ATTN: Tech Information Office

Institute of Geophysics & Planetary Physics
ATTN: Orson J. Anderson

General Electric Company
TEMPO-Center for Advanced Studies
ATTN: DASAC

Lockheed Missiles & Space Company
ATTN: Dr. Ronald E. Meyerott, Dept. 50-01,
Bldg. 201

The Lunar Space Institute
ATTN: Dr. Frederick Horz

Massachusetts Institute of Technology
ATTN: Professor Eugene Simmons

DEPARTMENT OF DEFENSE CONTRACTORS (Continued)

McDonnell-Douglas Corporation
ATTN: Mr. Ken McClymonds

Merritt Cases, Inc.
ATTN: J. L. Merritt

Occidental College
Department of Geology
ATTN: David Cummings

Pacific Technology
ATTN: Dr. R. T. Allen
ATTN: Dr. R. L. Bjork

Physics International Company
ATTN: Doc. Con. for Dr. Charles Godfrey
ATTN: Doc. Con. for Mr. Fred M. Sauer
ATTN: Doc. Con. for Dr. Robert Swift
ATTN: Doc. Con. for Mr. Dennis Orphal

R & D Associates
ATTN: Dr. Harold L. Brode
ATTN: Mr. Bob Thompson
ATTN: Mr. John Levesque
ATTN: Dr. C. P. Knowles
4 cy ATTN: Dr. Henry Cooper

Rand Corporation
ATTN: Dr. C. C. Mow

Science Applications, Inc.
ATTN: Mr. Mike McKay

Science Applications, Inc.
ATTN: Bill Layson

Science Applications, Inc.
ATTN: Dr. D. Maxwell
ATTN: Mr. R. Hoffmann

Stanford Research Institute
ATTN: Dr. Carl Peterson
ATTN: Mr. George Abrahamson

DEPARTMENT OF DEFENSE CONTRACTORS (Continued)

Systems, Science & Software
ATTN: Dr. Ted Cherry
ATTN: Dr. Ronald R. Grine
ATTN: Dr. D. Riney
ATTN: Mr. Bob A. Ken
ATTN: Document Control

Terra Tek, Inc.
ATTN: Dr. H. R. Pratt
ATTN: Dr. J. N. Johnson

TRW Systems Group
ATTN: Mr. Bing Fay

TRW Systems Group
ATTN: Mr. Norm Lipner
ATTN: Dr. Peter K. Dai, RI-2178
ATTN: Dr. Benjamin Sussholtz
ATTN: Mr. Edgar Wong

University of Illinois
ATTN: Dr. Nathan M. Newmark
ATTN: Dr. Skip Hendron
ATTN: Dr. Bill Hall

University of New Mexico
Civil Engineering Research Facility
ATTN: Mr. Del Calhoun
ATTN: Mr. D. J. Higgins

University of Texas
Department of Geological Sciences
ATTN: William R. Muehlberger

Weidinger Associates, Consulting Engineers
ATTN: Dr. Melvin L. Baron
ATTN: Ivan Nelson
ATTN: Ivan Sandler

Weidinger Associates, Consulting Engineers
ATTN: Dr. J. Isenberg